Reconfigurable antennas for modern IoT networks : design concepts and implementation strategies

Francesco Positano

To cite this version:

Francesco Positano. Reconfigurable antennas for modern IoT networks : design concepts and implementation strategies. Electromagnetism. Université Côte d'Azur, 2024. English. NNT : 2024COAZ4062 . tel-04926996

HAL Id: tel-04926996
https://theses.hal.science/tel-04926996v1

Submitted on 3 Feb 2025

UNIVERSITÉ CÔTE D'AZUR

ÉCOLE DOCTORALE
SCIENCES ET TECHNOLOGIES
DE L'INFORMATION ET
DE LA COMMUNICATION

THÈSE DE DOCTORAT

Antennes Reconfigurables pour Réseaux IoT modernes : Principes de Conception et Stratégies de Mise en Œuvre

Francesco POSITANO

Laboratoire d'Electronique, Antennes et Télécommunications (LEAT)
UMR7248, Université Côte d'Azur, CNRS

Présentée en vue de l'obtention du grade de docteur en électronique **d'**Université Côte d'Azur

Dirigée par : Robert STARAJ,
Prof. Université Côte d'Azur
Co-encadrée par : Leonardo LIZZI,
Ass. Prof. Università di Trento

Soutenue le : 18, Decembre, 2024

Devant le jury, composé de :
Laure HUITEMA, MCF HDR, XLIM Université de Limoges
Antonio CLEMENTE, HDR, CEA Leti, Grenoble
Guido VALERIO, Prof. Sorbonne Université, Paris
Fabien FERRERO, Prof. Université Côte d'Azur
Luca SANTAMARIA, Dr. ing. Greenerwave, Paris

LEAT

UNIVERSITÉ CÔTE D'AZUR

FRANCE 2030
Initiative d'Excellence

Antennes Reconfigurables pour Réseaux IoT modernes : Principes de Conception et Stratégies de Mise en Œuvre

---

Reconfigurable Antennas for Modern IoT Networks: Design Concepts and Implementation Strategies

Francesco POSITANO

Jury :

Président du jury

Rapporteurs

Laure HUITEMA, MCF HDR, XLIM Université de Limoges

Antonio CLEMENTE, HDR, CEA Leti, Grenoble

Examinateurs

Guido VALERIO, Prof. Sorbonne Université, Paris

Fabien FERRERO, Prof. Université Côte d'Azur

Directeur de thèse

Robert STARAJ, Prof. Université Côte d'Azur

Co-encadrant de thèse

Leonardo LIZZI, Ass. Prof. Università di Trento

Membres invités

Luca SANTAMARIA, Dr. ing. Greenerwave, Paris

to my family,

my blessing

Acknowledgements

This achievement would not have been possible without the daily guidance and support with my supervisor Leo, now friend and always example before me.

All along, I’ve been motivated by the broad knowledge of my thesis director Robert, and the expertise of Fabien, thank you both. I owe a special debt of gratitude to Luca for paving the way for my doctoral research and sparking my passion for academia.

I recognize that none of these invaluable exchanges would have been possible without the strong, united, and multidisciplinary team at LEAT. Here, I had the privilege of working alongside many brilliant minds, and I am grateful to each one of you.

Thanks to Philippe from Orange Lab, and to the CREMANT, for all their help with the measurements.

I would also like to extend my thanks to the PASSEPARTOUT consortium, participating to this project allowed me to put my research into practice, and i realize it is a fortunate privilege.

Special thanks to the Academy of Excellence “Networks, Information and Digital Society" at Université côte d’Azur, whose DocWalker program enabled me to fulfill my dream of spending three months at the prestigious Georgia Institute of Technology in the USA. My appreciation also goes to the Université Côte d’Azur’s DDIE and the Erasmus+ program for facilitating my visiting period at University of Trento in Italy.

Last but not least, I want to thank my family. This achievement is a result of their constant support and all the sacrifices they’ve made along the way.Their support has meant everything to me.

Francesco POSITANO
Nice, October, 2024

Résumé

La croissance rapide des applications de l'Internet des objets (IoT) a entraîné une forte demande en technologies sans fil avancées. Dans le contexte d'un paysage numérique en constante évolution, les antennes reconfigurables sont devenues un point focal crucial en raison de leur nature adaptable. Ce travail offre un aperçu complet du paysage actuel des technologies IoT et sans fil, en mettant l'accent sur les normes compatibles avec l'IoT et la manière dont elles ont influencé la conception des antennes. Cette recherche explore les défis de la conception, de l'optimisation et de la mise en œuvre de ces antennes spécifiquement pour les réseaux IoT modernes.

Les principes fondamentaux des antennes miniatures électriquement petites (ESA) et des conceptions d'antennes reconfigurables pour les applications IoT constituent la base de ce travail. Tout d'abord, l'exploration d'une antenne à polarisation circulaire omnidirectionnelle (OCP) miniature est effectuée, et une analyse approfondie de ses paramètres d'optimisation et de sa polarisation circulaire est réalisée. Une étude sur l'antenne OCP reconfigurable est également fournie, avec un accent sur les stratégies de mise en œuvre pratique.

En outre, la recherche explore la reconfigurabilité du diagramme, une caractéristique qui permet à l'antenne de modifier dynamiquement son diagramme de rayonnement. Une antenne à réseau parasitaire orientable électroniquement (ESPAR) reconfigurable et à profil bas est conçu et optimisé, avec présentation et analyse des résultats mesurés. La recherche propose également des solutions potentielles au problème de réoptimisation associé à la mise en œuvre pratique des circuits de commutation. L'étude inclut également des tests sur le terrain en conditions réelles. La conception et les essais sur le terrain d'une antenne ESPAR pour les applications IoT à longue portée basées sur les véhicules aériens sans pilote (UAV) sont discutés, en couvrant l'intégration du transceiver.

Enfin, ce travail aborde la conception d'une antenne reconfigurable en fréquence pour les communications IoT basées sur les satellites, avec les défis de la miniaturisation et de la reconfigurabilité au premier plan.

Mots-clés : Internet of Things (IoT), Omnidirectional Circular Polarization (OCP), Electronically Steerable Parasitic Array Radiator (ESPAR), Reconfiguration en Polarisation, Reconfiguration en Diagramme de Rayonnement, Reconfiguration en Frequence.

Abstract

The rapid growth of Internet of Things (IoT) applications has led to a surge in demand for advanced wireless technologies. In the context of an ever-evolving digital landscape, reconfigurable antennas have emerged as a pivotal focus due to their adaptive nature. This work provides a comprehensive overview of the current landscape of IoT and wireless technologies, with a focus on the IoT-compliant standards and how they have influenced antenna design. This research explores the challenges of designing, optimizing, and implementing these antennas specifically for modern IoT networks.

The fundamental principles of miniature Electrically Small Antennas (ESA)s and reconfigurable antennas designs for IoT applications builds the foundation of this work. Firstly, the exploration of a miniature Omnidirectional Circular Polarization (OCP) antenna, and an in-depth analysis of its optimization parameters and circular polarization is carried out. A study on reconfigurable OCP antenna is also provided, with a stress on practical implementation strategies.

Further, the research explores pattern reconfigurability, a feature that allows the antenna to dynamically alter its radiation pattern. A low-profile Pattern Reconfigurable Electronically Steerable Parasitic Array Radiator (ESPAR) is designed and optimized, with measured results presented and analyzed. The research also proposes potential solutions to the re-optimization problem associated with the practical implementation of switching circuits. The study also includes real-life field-testing. The design and on-field testing of an ESPAR antenna for Unmanned Aerial Vehicle (UAV) based long-range IoT applications are discussed, covering the integration of the transceiver.

Finally, this work discusses the design of a frequency reconfigurable antenna for satellite-based IoT communications, with the challenges of miniaturization and reconfigurability at the forefront.

Keywords : IoT, OCP, ESPAR, Polarization reconfigurable, Pattern reconfigurable, Frequency reconfigurable.

Author’s Publication List

Peer-Reviewed Journal Paper

[J1] F. Positano, L. Santamaria, R. Staraj and L. Lizzi, "Compact Omnidirectional Circularly Polarized Antenna via Alford Loop and Wire-Patch Structure Combination," in IEEE Open Journal of Antennas and Propagation, vol. 5, no. 2, pp. 277-285, April 2024, doi: 10.1109/OJAP.2023.3340975.

[J2] F. Positano, L. Lizzi, R. Staraj, “Design and On-Field test of ESPAR antenna for UAV based Long Range IoT applications", in Frontiers Antenna and Propagation, vol. 2, doi: 10.3389/fanpr.2024.1429710.

Peer-Reviewed International Conference Paper

[C1] F. Positano, L. Santamaria, F. Ferrero, L. Lizzi and M. Grande, "Pattern Reconfigurable Parasitic Element Array Antenna for Air Quality Portable Sensor," 2021 IEEE Conference on Antenna Measurements & Applications (CAMA), Antibes Juan-les-Pins, France, 2021, pp. 602-604, doi: 10.1109/CAMA49227.2021.9703644.

[C2] F. Positano, L. G. Gallo, L. Santamaria, R. Staraj and L. Lizzi, "High-Gain Wire-Patch Based Pattern Reconfigurable Antenna for IoT Applications," 2022 IEEE International Symposium on Antennas and Propagation and USNC-URSI Radio Science Meeting (AP-S/URSI), Denver, CO, USA, 2022, pp. 1476-1477, doi: 10.1109/AP-S/USNC-URSI47032.2022.9886858.

[C3] V. Garzone, F. Positano, L. Santamaria, R. Staraj and L. Lizzi, "Polarization Reconfigurable Circularly Polarized Antenna for IoT Applications," 2022 IEEE International Symposium on Antennas and Propagation and USNC-URSI Radio Science Meeting (AP-S/URSI), Denver, CO, USA, 2022, pp. 393-394, doi: 10.1109/AP-S/USNC-URSI47032.2022.9886374.

[C4] F. Positano, L. Santamaria, R. Staraj and L. Lizzi, "Low Profile Pattern Reconfigurable ESPAR for UAVs in IoT Applications," 2023 17th European Conference on Antennas and Propagation (EuCAP), Florence, Italy, 2023, pp. 1-4, doi: 10.23919/EuCAP57121.2023.10133027.

[C5] F. Positano, L. Lizzi and R. Staraj, "Pattern Reconfigurable ESPAR System for Long Range IoT Communications," 2023 IEEE Conference on Antenna Measurements and Applications (CAMA), Genoa, Italy, 2023, pp. 707-709, doi: 10.1109/CAMA57522.2023.10352906.

[C6] F. Positano, L. Lizzi and R. Staraj, "Practical Measurements on ESPAR Antenna for UAV based Long Range Communications," 2023 IEEE Conference on Antenna Measurements and Applications (CAMA), Genoa, Italy, 2023, pp. 90-92, doi: 10.1109/CAMA57522.2023.10352737.

[C7] F. Positano, H. Al Jamal, E. Tentzeris, and L. Lizzi, "On The Performance and Calibration of Arbitrarily Conformal Additively Manufactured Phased Arrays for Wearable, Deployable, and Morphing RF Applications", 2024 IEEE International Symposium on Phased Array Systems & Technology, Boston MA, USA, 2024 [PRESENTED]

[C8] F. Positano, L. Lizzi, F. Ferrero, R. Staraj "Frequency Agile Omnidirectional Alford Loop: an Implementation Perspective", 2025 19th European Conference on Antennas and Propagation (EuCAP), Stockholm, Sweden, 2025, [accepted]

[C9] F. Positano, L. Lizzi "Enabling UWB Antenna Polarization Diversity Through a Switchable Feeding Network", 2025 19th European Conference on Antennas and Propagation (EuCAP), Stockholm, Sweden, 2025,[accepted]

Peer-Reviewed National Conference Paper

[N1] F. Positano, L. Lizzi, R. Staraj, F. Manassero and M. D'Onofrio "Conception et Caractérisation d'une antenne reconfigurable en diagramme basée sur mesures RSSI : cas d'etude de communication pour drones," 23eme Journées Nationales Microondes (JNM), Antibes Juan-les-Pins, 2024

[N2] F. Positano, L. Lizzi and R. Staraj"Antenne Compacte Omnidirectionnelle à Polarisation Circulaire pour Applications IoT" 23eme Journées Nationales Microondes (JNM), Antibes Juan-les-Pins, 2024

Contents

1 Context and Motivation

1.1 Current Picture of IoT and Wireless Technologies

Now in its fourth year of use, the 5th generation of telecommunication technology standard still only reaches 81% of the population, and just 51% in rural areas [1]. This indicates that the full realization of the 5th generation is behind schedule [2]. Recent global events, including a pandemic and a chip shortage, have slowed its deployment and utilization [3]. During the same period, mobile data traffic surged by 35% [4], driven by increased accessibility to consumer devices and pandemic-related restrictions, highlighting the urgent need to rapidly close the gap with the expectations.

Since 2014, the number of research works related to 5G has risen dramatically, with nearly 3500 publications in 2020 [5]. Although we may not be fully prepared to leverage 5G's capabilities today, particularly its *killer application* of augmented reality at user level, significant progress has been made in integrating Artificial Intelligence (AI) across all layers of this new technology [6]. 5G and beyond cellular networks are anticipated to support enhanced Mobile Broadband (eMBB), Ultra-Reliable and Low Latency Communications (URLLC), and massive Machine Type Communications (mMTC). Unlike the first two, which focus on high data rate services and ultra-low latency, the mMTC aligns with the IoT vision, aiming to support a vast number of devices with limited radio resources.

Since the term IoT was coined by Ashton [7], three wireless cellular network technologies have succeeded one another. Changes in people's interactions with technological devices, as well as advancements in industry and technology, have played pivotal roles in shaping the definition of IoT as we understand it today. In 2011, it was defined as the evolution of the traditional internet, *"created around interconnections of diverse objects in the physical world, such as vehicles, cellphones, habitats, and habitat occupants"* [8], making the automation of actions its key scheme. Sensors capture information about temperature, orientation, motion, environmental conditions, etc. The system then triggers an actuator or an action, such as processing certain collected data or directly transmitting the raw sensed data using the internet as infrastructure [9].

Still relying on the traditional internet, IoT enables a range of new emerging and trailblazing applications for the welfare of future societies, representing, in fact, the true evolution of the internet. Applications like Smart Wearables for eHealth [10], Domotics and Smart Security for Smart Housing [11], self-driving cars, driving assistance, and smart parking for Smart Mobility [12], as well as Smart Grids, Smart Agriculture, and Smart Metering and Monitoring [13], are already gaining momentum in the current vision of an interconnected society thanks to solutions ranging from Radio Frequency IDentification (RFID)s [14] to ambitious satellite-based IoT [15], as depicted in Figure 1.1.1.

Figure 1.1.1: An example of wireless IoT scenario with applications ranging from smart wearable (Wireless Personal Area Network (WPAN)) to smart grids (Wide Area Network (WAN)) [2]

Connectivity being the leading target, smart IoT environments consist of wireless small “objects" for ease of use, deployment, and maintenance. These objects combine sensors, actuators, and a lightweight communication protocol on an affordable hardware platform [16]. Low-cost devices are primarily created by integrating non-proprietary technology solutions that operate on unlicensed Industrial, Scientific and Medical (ISM) bands, along with low-cost hardware platforms like Arduino® or single-board computers. This facilitates the design of end nodes, which has sparked unprecedented market interest in the consumer sector.

In 2019, there were an estimated 8 billion connected devices in use worldwide. Figure 1.1.2 shows a reliable forecast [17] that expects the number of interconnected devices to increase to around 30 billion by 2030, significantly outnumbering human users. Internet and media devices such as smartphones dominate the consumer segment, while the emerging interconnected objects that will attract interest in the coming years include connected autonomous vehicles, IT infrastructure, and smart grids, indicating a shift towards the Industrial Internet of Things (IIoT).

In such a crowded, ultra-dense environment, where the number of sporadic access attempts from Machine Type Communications (MTC) devices could be significantly large, a serious challenge is posed to the current capabilities of traffic channels [18], representing a substantial scalability issue [19].

In an ubiquitous, heterogeneous ultra-dense network of IoT devices operating in shared bands, self-interference as well as cross-technology interference pose significant challenges to efficient communication. The current landscape features a wide array of wireless technologies that are designed to cover various IoT connectivity requirements, with trade-offs between access and communication channel reliability, as well as Quality of Service (QoS) and scalability being sought starting from the data link layer. These solutions utilize random access or Carrier Sense Multiple Access (CSMA) protocols, which inherently limit the number of devices that can be supported. Other technologies employ channel diversity, opportunistic spectrum access, and adaptive transmission strategies such as channel hopping or multi-modem base stations to achieve greater scalability.

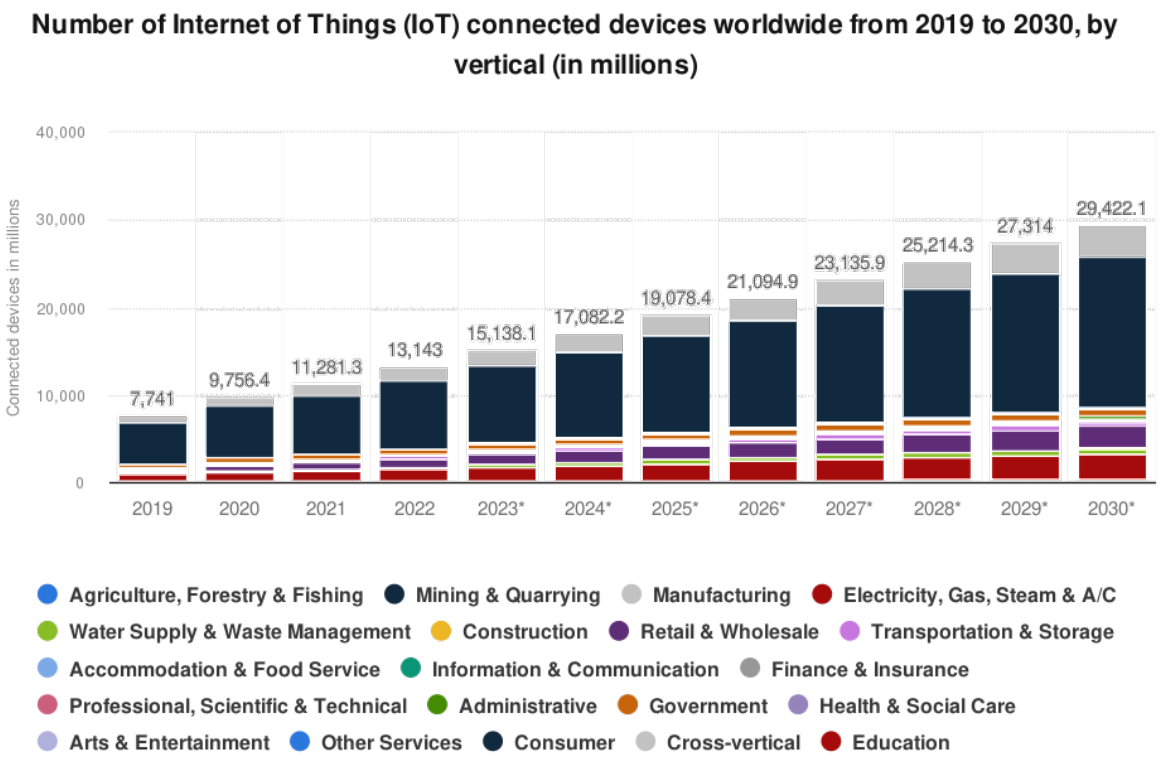

Figure 1.1.2: Data and prospective of the number of IoT connected devices worldwide from 2019 to 2030 [17]

1.2 Range of IoT-compliant Standards

Due to the need for capillary coverage, IoT communication ranges from a few meters to tens of kilometers, depending on the deployment. Networks include WPAN, Wireless Local Area Network (WLAN), Wireless Regional Area Network (WRAN), and WAN, with minimization of power consumption being a crucial factor in each. With sub-1 GHz bands, propagation attenuation and multipath fading are reduced [20], but this also limits data rates. The choice of narrower bands increases the Signal to Noise Ratio (SNR) but also restricts the flexibility of the devices and requires specific modulation techniques to make the transmission more resilient to interference. Focusing on low duty cycle and long-range, Low Power Wide Area Network (LPWAN) completes the set of wireless networks [21]. Figure 1.2.1

Open Standards

Standards Development Organisations (SDO)s such as Third Generation Partnership Project (3GPP), Institute of Electrical and Electronics Engineers (IEEE), Internet Engineering Task Force (IETF), and European Telecommunications Standard Institute (ETSI) work on the development of open standards that increasingly focus on low power and long-distance communications. Some of them are evolving current in-use protocols, while others, with the support of Special Interest Group (SIG) Industrial alliances, have developed new specifications from scratch.

Assuming that legacy cellular wireless technologies can guarantee coverage over large geographical areas, 3GPP is evolving its cellular standards to improve range, signal penetration, and prolong device

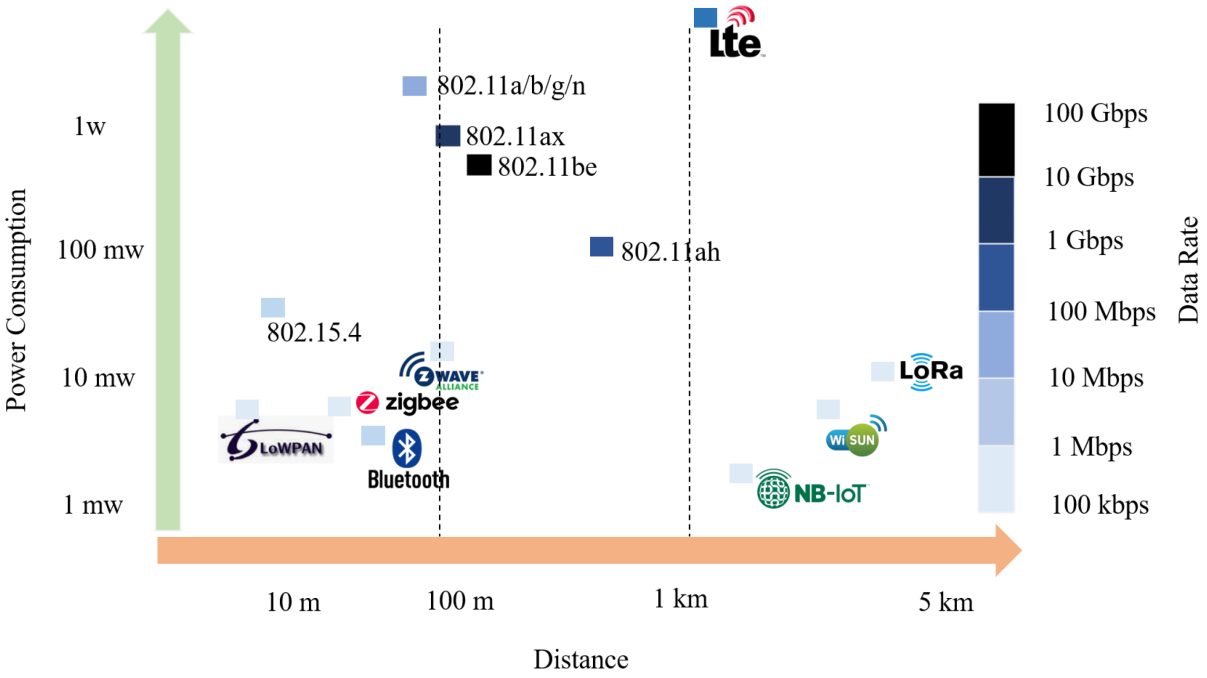

Figure 1.2.1: Overview of IoT technologies compared to power consumption, distance and data rate. [22]

battery lifetime with enhanced Machine Type Communication (eMTC): Extended Coverage - Global System for Mobile communication (EC-GSM), Long Term Evolution for Machine-Type communications (LTE-M), and Narrow-Band Internet of Things (NB-IoT).

The EC-GSM has been proposed as an evolution of the Global System for Mobile communication (GSM) technology from the 2nd generation cellular network to enhance its coverage and penetration in indoor environments using sub-GHz bands. However, Mobile Network Operator (MNO)s are decommissioning second and third generation cellular network technologies [23], and the interest of 3GPP is focusing on the latest LTE-M and NB-IoT.

LTE-M was proposed in 3GPP release 12, with its low power capabilities stemming from a reduction in bandwidth from 20 MHz to 1.4 MHz, low data rates, and a Phisical Random Access Channel (PRACH) that makes it a versatile LPWAN technology [24]. However, random access to the channel limits the number of simultaneous User Equipment (UE)s that can be connected. To complete the scenario, NB-IoT was proposed in release 13 to use even lower rates in a 180 kHz band. NB-IoT's Ultra Narrow Band (UNB) can be deployed inside a 200 kHz GSM carrier, within a single Long Term Evolution (LTE) Physical Resource Block (PRB), or in the LTE guard band, making it an easy-to-deploy LPWAN alternative to LTE-M for more restricted data communications. Additionally, it replaces random access to the channel with Frequency Division Multiple Access (FDMA) in the uplink and Orthogonal Frequency Division Multiple Access (OFDMA) in the downlink, incorporating frequency channel hopping for higher scalability [25].

Another crucial SDO in the development of IoT standards is the IEEE, responsible for defining widely used commercial WPAN standards like 802.15.1 (Bluetooth), WLAN standards like 802.11 (Wi-Fi), and their improved coverage versions up to LPWAN.

In the WPAN scenario, Bluetooth Low Energy (BLE), based on 802.15.1 Bluetooth as its power-saving optimized evolution, operates in the 2.4 GHz ISM band using 40 channels of 2 MHz each, with adaptive frequency hopping for more robust communication that can reach up to 1 Mbps of throughput [26]. As an alternative, ZigBee, a specification based on 802.15.4 Low Rate - Wireless Personal Area Network (LR-WPAN), includes sub-1 GHz bands along with the 2.4 GHz ISM to prioritize low power consumption, using even smaller data rates than BLE specifically intended for wider coverage.

The 802.11ah and 802.11af standards have been proposed, respectively, on unlicensed and licensed sub-1 GHz bands as evolutions of the 802.11ac, also known as Wi-Fi 5, to improve the coverage range of conventional WLANs. Their data rates are 10 times slower compared to 802.11ac, making them suitable for low power WLAN, while also increasing the communication range up to 1 km, bridging WLAN to WRAN [27].

For LPWAN communications, IEEE has proposed the 802.15.4k Low Energy Critical Infrastructure Monitoring Networks (LECIM) and 802.15.4g standards [28]. The former uses UNB on the 433 MHz band with Direct Sequence Spread Spectrum (DSSS) modulation. It can implement either Carrier Sense Multiple Access with Collision Avoidance (CSMA/CA) or Aloha with Priority Channel Access (PCA), depending on specific requirements, to access the channel, limiting data rates to 128 kbps and enabling communications up to 20 km. On the other hand, 802.15.4g adds additional types of modulation to increase channel reliability, supports a wide range of data rates up to 1 Mbps, and limits frame lengths to 1500 bytes to avoid Internet Protocol (IP) packet fragmentation.

Proprietary Standards and Technologies

Most of the SIGs prefer low-rate, low-power, and long-range standards to build their own specifications. Among them, the LPWAN scenario is the most popular due to its combination of low cost and low power consumption, perfectly aligning with the IoT vision. The most frequently used topology is a star, which considers a gateway as a relay between the Wireless Sensors Networks (WSN) and the internet. At the Medium Access Control (MAC) level, access to the channel is commonly random due to the sporadic activity of the WSN, but carrier sensing is also used by some for better resource allocation, resulting in more stable communication.

Among the most widely adopted technologies, SigFox is a solution that uses UNB of 100 Hz over a sub-1 GHz ISM band carrier (868 MHz in Europe and 902 MHz in the United States) to achieve high sensitivity of up to -142 dBm, with a range of up to 40 km in rural settings [29]. It employs Random Frequency Division Multiple Access (R-FDMA) to access resources, which sets a limit of 100 bps for maximum throughput. This technology is widely used for smart metering and sensing, where there is a need for continuous transmission of very small amounts of data.

LoRaWAN, from the LoRa Alliance, operates in the 433, 868, and 915 MHz ISM bands using a proprietary modulation scheme developed by Semtech Corporation, based on Chirp Spread Spectrum (CSS), which is resistant to the Doppler effect and multipath fading [30]. Spreading factors are used to tune the power spreading to trade off between data rate and range. Data rates are significantly higher than those of SigFox, ranging from 300 bps to 37.5 kbps depending on the spreading factor, which reduces the range to just a few kilometers in rural environments. Channel access is random and based on Aloha, and due to its unique topology, messages transmitted may be received by multiple base stations, allowing for approximate localization of the transmitting end device.

Future Directions: Fog and Edge Computing

To summarize, the widespread adoption of WSN made up of simple, low-cost devices has led to the definition of standards and technology specifications that prioritize power consumption reduction. Most IoT Machine to Machine (M2M) networks are battery-powered, and since the most energy-consuming aspect of IoT devices is Radio Frequency (RF) transmission, simple and lightweight techniques for modulation and channel access are preferred to reduce power consumption on a communication basis.

Following this framework, all raw data is typically transmitted and then stored or processed far from the device, generating a huge amount of mostly useless data traffic and limiting channel resources. Fog and Edge computing have recently emerged to propose a new framework that integrates small processing capabilities directly on the end node [31], allowing for the reporting of only small amounts of useful data instead of the entire unrefined dataset.

From a power consumption perspective, this new scheme would not be reasonable if the processing required more power than what is saved during transmission. Thus, Fog/Edge computing is closely tied to the adoption of Machine Learning (ML) and AI for optimized and low-power processing on the end node. Furthermore, with the advent of the 6th generation of mobile cellular networks, the Internet of Intelligent Things (IoIT) has been announced, representing a massive integration of AI with every portable device [32].

1.3 The Role of Antenna Design in IoT

Designing antennas for IoT is all about trade-offs. The increasing demand for miniature, portable, and sometimes implantable devices requires a high level of miniaturization for both hardware platforms and integrated or connected antennas. At the same time, especially for LPWANs, there is a demand for the use of sub-1 GHz frequencies, which are characterized by wavelengths greater than 30 cm. This converges to the need for Electrically Small Antennas (ESA) [33], meaning those for which the equation 1.3.1 holds, where d is the antenna's maximum dimension.

$$d << \frac{1}{k} = \frac{\lambda}{2\pi} \tag{1.3.1}$$

According to the relation first proposed by Chu [34], also reported in 1.3.2 for omnidirectional antennas, the antenna's quality factor Q is inversely proportional to the volume of the sphere that encloses it. This means that the bandwidth is limited by the size of the antenna: the smaller the antenna is, the narrower its bandwidth and the lower its efficiency.

$$Q \geq \frac{1}{(ka)^3} + \frac{1}{ka} \tag{1.3.2}$$

The impedances of ESAs are characterized by low resistive values, primarily due to the limited amount of conducting material used. Additionally, since these antennas are often employed in portable and wearable devices, they are highly sensitive to nearby objects, including the human body. This sensitivity significantly impacts antenna matching due to coupling effects, presenting challenges for effective integration.

From the radiation pattern perspective, since IoT end nodes and gateways must guarantee continuous availability but sporadic transmission/reception, omnidirectional or quasi-isotropic pattern antennas are preferred for their orientation independence in far-field distribution. For these antennas, power is distributed evenly in all directions, exhibiting stable directivity across various orientations, although their overall directivity value is generally low.

The wide variety of protocols discussed in the previous section allows for some freedom in adopting constrained antennas in IoT end-node devices for various application needs, covering the limitations of inefficient antennas (e.g., using CSS modulation for UNB). However, in most cases, the requirements prioritize low power consumption, which, even with optimal modulation techniques and technologies, is difficult to achieve if the physical device functions carry inefficiencies.

One emerging solution to address the trade-offs between performance and antenna dimensions is the design of chip antennas [35]. Their miniaturization can reach dimensions of 0.005λ. A matching circuit allows the chip antenna to excite modes of the hardware platform's Printed Circuit Board (PCB) ground plane, influencing the overall size of the radiating element and enabling reasonable efficiency [36]. Nonetheless, antenna design is complex because it cannot be considered independently of its integration into specific devices; the size of the device's ground plane, the antenna placement, and the matching circuit design are all essential factors.

Taking advantage of the electric field propagation properties, Circular Polarization (CP) antennas are employed, primarily on gateways or base stations, due to their independence from orientation mismatch between transmitting and receiving antennas [37]. Moreover, CP propagation is resistant to multipath interference or fading [20].

1.3.1 Reconfigurable Antennas

Recently, devices must guarantee coverage and coexistence of multiple technologies while keeping their size relatively small for portability and maintaining low power consumption to ensure battery life that is expected to last for years. In some cases, the presence of multiple antennas on a single device could require a volume that reduces its portability and user-friendliness.

In this context, reconfigurable antennas, also referred to as Smart Antennas, represent a viable solution since they allow for dynamic changes in antenna properties, enabling the combination of multiple services and technologies simultaneously. From a practical perspective, the additional performance provided by these antennas justifies the higher costs and complexity associated with reconfiguration.

To minimize power consumption, antennas combined with rectifier circuits, also known as rectennas, can be used to harvest power from environmental RF waves [38], allowing for integration into battery-less devices that do not require any maintenance.

Reconfigurable Properties

Smart antennas can redistribute the current distribution on the radiating structure in a manner that can lengthen or shorten the current path, affecting the electrical length of the antenna. In such cases, the antenna experiences a shift in frequency, making it reconfigurable in frequency [39]. Frequency agility is commonly used to add physical propagation channel diversity to improve security or to substitute complex, bulky wideband or multiband antennas with dynamic narrowband antennas that can adapt to environmental influences or interference.

Channel diversity is also obtained by adopting switchable polarization. Since orthogonal linear polarizations are transparent to each other, inter-channel interference is suppressed. Moreover, sources of different polarizations on the same antenna can be dynamically tuned to enable CP, providing an additional degree of freedom for polarization reconfigurability.

Another dynamically tunable parameter is the radiation pattern beam. Instead of developing an omnidirectional pattern, antennas can direct the beam in a specified direction, significantly reducing energy dissipation in undesired directions and filtering interference. This approach increases the SNR only in the desired direction, resulting in spatial channel diversity, which drastically reduces the need for packet retransmissions [40] and consequently lowers overall power consumption.

Reconfiguration Mechanisms

Reconfiguration techniques require more elaborate radiating structures where the dynamics are controlled by the same hardware platform of the end-node device. Reconfiguration is achieved by interacting with the radiating structure through:

- Electrical and optical systems, by adopting Radio Frequency - Microelectromechanical Systems (RF-MEMS), Positive Intrinsic Negative (PIN)-diodes, or photoconductive laser diodes as switches to activate different paths on the conductive material. Alternatively, a Variable Capacity (Varicap)-diode is employed to gradually tune the antenna impedance matching by controlling the proportional biasing voltage.
- Physical properties, changing the surface or volume of the antenna itself, e.g., deployable antennas commonly used in satellite applications, flexible and origami-shaped antennas that can fold on themselves, or using liquid metal in microfluidic channels.
- Tunable materials, acting on the magnetic properties of specific non-linear materials like liquid crystals or ferrite.

There are not many properties suitable for IoT small, portable device antenna designs. Tunable materials and shape-changing radiating structures drastically increase complexity and, consequently, the cost of manufacturing. Switching techniques are the most commonly used in this context; nonetheless, even if optical switches are independent of RF interferences, they require a complex and energy-consuming activation mechanism. On the other hand, RF-MEMS are the most energy-efficient switching technique, with losses limited to 0.2 dB, although their integration is challenging due to the need for high biasing voltage [41]. Finally, PIN-diodes are the most common solution for IoT antennas; their response is faster than that of RF-MEMS, and they offer low cost and complexity, along with relatively low loss [42].

Adopting switching mechanisms means considering biasing components through Direct Current (DC) current on an RF radiating structure. This may cause problems in terms of interference, loss, and electrical inconsistency in the circuit structure.

The practical approach is to consider the two coexisting systems as independent, isolating each from the other without sacrificing performance [43]. To isolate the DC system from the RF current, capacitors are placed at the extremes of the switching component. Their impedance $Z_C = {}^{1}/_{j\omega C}$ tends to zero as frequency and the value of C increase, being transparent to Alternating Current (AC) current but acting as an open circuit for DC current. Similarly, an inductive load at the ends of the switching component, with impedance $Z_L = j\omega L$, tends to infinity as frequency and the value of L increase, choking the AC component while acting as a short circuit for DC. As a result, while the integration of these systems enhances overall performance, it simultaneously increases the complexity of antenna design, necessitating careful consideration during the development process

1.4 Objectives and Contributions

Summarising, deploying IoT protocols comes with numerous challenges stemming from various constraints and conditions. A primary issue is device congestion due to the increasing number of IoT devices, demanding for more reliable channels. The complexity of the environments where IoT devices operate creates additional difficulties. Various predictable and unpredictable sources of interference, such as atmospheric conditions, other electronic devices or multiple reflections, can compromise the quality of signal transmission. The demand for portability requires IoT devices to be small in size facilitating seamless integration into diverse systems and environments. However, this need for miniaturization often conflicts with the requirement for low-power consumption. Smaller devices typically have less capacity for batteries, and decreased antenna efficiency which may cause weak communication channels, resulting in errors and retransmissions. The goal of this thesis is to propose solutions to these challenges from an antenna design perspective. The objective is to identify the best trade-off of antenna design characteristics that best addresses the constraints of IoT applications.

- Chapter 2 introduces a compact OCP antenna design proposed for portable IoT applications. OCP are particularly beneficial in modern wireless systems due to their ability to mitigate issues related to signal orientation and multi-path fading. The design, which combines two omnidirectional sources with different linear polarizations, is detailed in Section 2.2 and published in [J1].

  A reconfigurable OCP antenna enhancement of the aforementioned antenna structure is proposed to address channel diversity. The contribution to its proof of concept have been presented in [C3]. Progress in this thesis includes addressing the challenge of reconfiguration control design and integration, with a focus on its practical implementation.

- Chapter 3 tackles the trade-off between low-power and long-range communications through the design of ESPARs, valued for their single-feed and high-gain switchable directive beam. In Section 3.2, Particle Swarm Optimization (PSO) is used to optimize reactive loads on a seven-elements ESPAR, with the proof of concept presented in [C2]. A practical design approach considering the reconfiguration control system is presented, supported by measurements on a prototype operating at 5.075 GHz. These results have also been presented in [C4].

  Section 3.3 proposes the design of a five-element ESPAR with a simpler reconfiguration switching system based on PIN-diodes [C5]. The design and integration of the control system are detailed, as well as the characterization in an open-air environment on an hexacopter to quantify the channel quality using pattern reconfigurable antennas [C6]. The results have also been published in [J2].

  Section 3.4 explores a flexible, arbitrarily conformal phased array for wearable, deployable, and morphing RF applications. Strategic tuning and selective activation can be combined with shape-changing capabilities to enhance the performance of the phased array or mitigate coupling effects.

The assessment of concave, convex and accordion-like folding is presented in the section and has been featured in [C7].

- Chapter 4 addresses the challenge of multi-standard coexistence on the same IoT device. An horizontally polarized antenna, suitable for ground station in satellite IoT applications, is proposed to operate on the licensed band 400 MHz and ISM 433 MHz band, using a simple frequency reconfiguration mechanism. The design is validated through two reconfiguration mechanisms: a continuous one with Varicap and a discrete, switchable one with PIN-diodes. The latter also includes measurements on a prototype that have been submitted in [C8].

Measurements of small, differentially-fed antennas, as well as reconfigurable ones, require certain precautions. These include the use of external balancing networks and the isolation of DC components needed for reconfiguration from the RF. These considerations have been factored into this thesis, highlighting the importance of well-executed characterization. All the proposed designs in this thesis addresses specific requirements and combined the necessary solutions with a particular emphasis on practical implementation and integration.

References

[1] M. del Mar Negreiro Achiaga, “Legislative train 02.2024 2 a europe fit for the digital age 5g action plan.” https://www.europarl.europa.eu/legislative-train/carriage/5g-action-plan/report?sid=7801, 2024.

[2] E. C. of Auditors, “Special report 5g roll-out in the eu: delays in deployment of networks with security issues remaining unresolved.” https://www.eca.europa.eu/Lists/ECADocuments/SR22_03/SR_Security-5G-networks_EN.pdf, 2022.

[3] E. Shein, “Global chip shortage: Everything you need to know.” https://www.techrepublic.com/article/global-chip-shortage-cheat-sheet/, October 2023. (Accessed on 04/09/2024).

[4] “Delay in 5g deployment causes and consequences - telecom review.” https://www.telecomreview.com/articles/reports-and-coverage/3962-delay-in-5g-deployment-causes-and-consequences, 6 2020.

[5] S. Mendonça, B. Damásio, L. Charlita de Freitas, L. Oliveira, M. Cichy, and A. Nicita, “The rise of 5g technologies and systems: A quantitative analysis of knowledge production,” *Telecommunications Policy*, vol. 46, no. 4, p. 102327, 2022. Innovation in 5G technology: leadership, competition and policy issues.

[6] S. Douglas, “2024 will be a catalyst for 5g standalone 5g core deployments.” https://www.rcrwireless.com/20240130/opinion/readerforum/2024-will-be-a-catalyst-for-accelerating-5g-standalone-5g-core-deployments-reader-forum, 1 2024.

[7] K. Ashton, “That ’internet of things’ thing - rfid journal.” https://www.rfidjournal.com/that-internet-of-things-thing, June 2009. (Accessed on 04/10/2024).

[8] J. Zheng, D. Simplot-Ryl, C. Bisdikian, and H. T. Mouftah, “The internet of things [guest editorial],” *IEEE Communications Magazine*, vol. 49, no. 11, pp. 30–31, 2011.

[9] R. Khan, S. U. Khan, R. Zaheer, and S. Khan, “Future internet: The internet of things architecture, possible applications and key challenges,” in *2012 10th International Conference on Frontiers of Information Technology*, pp. 257–260, 2012.

[10] F. John Dian, R. Vahidnia, and A. Rahmati, “Wearables and the internet of things (iot), applications, opportunities, and challenges: A survey,” *IEEE Access*, vol. 8, pp. 69200–69211, 2020.

[11] M. Khan, B. N. Silva, and K. Han, “Internet of things based energy aware smart home control system,” *IEEE Access*, vol. 4, pp. 7556–7566, 2016.

[12] Z. Mahrez, E. Sabir, E. Badidi, W. Saad, and M. Sadik, “Smart urban mobility: When mobility systems meet smart data,” *IEEE Transactions on Intelligent Transportation Systems*, vol. 23, no. 7, pp. 6222–6239, 2022.

[13] M. Orlando, A. Estebsari, E. Pons, M. Pau, S. Quer, M. Poncino, L. Bottaccioli, and E. Patti, “A smart meter infrastructure for smart grid iot applications,” *IEEE Internet of Things Journal*, vol. 9, no. 14, pp. 12529–12541, 2022.

[14] S. Amendola, R. Lodato, S. Manzari, C. Occhiuzzi, and G. Marrocco, “Rfid technology for iot-based personal healthcare in smart spaces,” *IEEE Internet of Things Journal*, vol. 1, no. 2, pp. 144–152, 2014.

[15] S. R. Pokhrel and J. Choi, “Data-driven satellite communication and control for future iot: Principles and opportunities,” *IEEE Transactions on Aerospace and Electronic Systems*, vol. 60, no. 3, pp. 3307–3318, 2024.

[16] A. Al-Fuqaha, M. Guizani, M. Mohammadi, M. Aledhari, and M. Ayyash, “Internet of things: A survey on enabling technologies, protocols, and applications,” *IEEE Communications Surveys & Tutorials*, vol. 17, no. 4, pp. 2347–2376, 2015.

[17] L. S. Vailshery, “Iot connected devices worldwide 2019-2030 | statista.” https://www.statista.com/statistics/1183457/iot-connected-devices-worldwide/, July 2023.

[18] S. K. Sharma and X. Wang, “Toward massive machine type communications in ultra-dense cellular iot networks: Current issues and machine learning-assisted solutions,” *IEEE Communications Surveys & Tutorials*, vol. 22, no. 1, pp. 426–471, 2020.

[19] N. Jiang, Y. Deng, A. Nallanathan, X. Kang, and T. Q. S. Quek, “Analyzing random access collisions in massive iot networks,” *IEEE Transactions on Wireless Communications*, vol. 17, no. 10, pp. 6853–6870, 2018.

[20] *Radio Wave Fundamentals*, ch. 1, pp. 1–33. John Wiley & Sons, Ltd, 2013.

[21] U. Raza, P. Kulkarni, and M. Sooriyabandara, “Low power wide area networks: An overview,” *IEEE Communications Surveys & Tutorials*, vol. 19, no. 2, pp. 855–873, 2017.

[22] M. Mansour, A. Gamal, A. I. Ahmed, L. A. Said, A. Elbaz, N. Herencsar, and A. Soltan, “Internet of things: A comprehensive overview on protocols, architectures, technologies, simulation tools, and future directions,” *Energies*, vol. 16, no. 8, 2023.

[23] G. Langham, “Decommissioning legacy networks will be key to reducing operators’ energy usage,” 2022. (Accessed on 28/09/2024).

[24] H. Wang and A. O. Fapojuwo, “A survey of enabling technologies of low power and long range machine-to-machine communications,” *IEEE Communications Surveys & Tutorials*, vol. 19, no. 4, pp. 2621–2639, 2017.

[25] A. Rico-Alvarino, M. Vajapeyam, H. Xu, X. Wang, Y. Blankenship, J. Bergman, T. Tirronen, and E. Yavuz, “An overview of 3gpp enhancements on machine to machine communications,” *IEEE Communications Magazine*, vol. 54, no. 6, pp. 14–21, 2016.

[26] M. Collotta, G. Pau, T. Talty, and O. K. Tonguz, “Bluetooth 5: A concrete step forward toward the iot,” *IEEE Communications Magazine*, vol. 56, no. 7, pp. 125–131, 2018.

[27] M. Park, “Ieee 802.11ah: sub-1-ghz license-exempt operation for the internet of things,” *IEEE Communications Magazine*, vol. 53, no. 9, pp. 145–151, 2015.

[28] “Ieee standard for low-rate wireless networks,” *IEEE Std 802.15.4-2020 (Revision of IEEE Std 802.15.4-2015)*, pp. 1–800, 2020.

[29] “What is sigfox 0g technology.” https://www.sigfox.com/what-is-sigfox/, 2024. UnaBiz Technology.

[30] “Lora® and lorawan®.” https://www.semtech.com/uploads/technology/LoRa/lora-and-lorawan.pdf, March 2024. Semtech Corporation, version 1.0 AN1200.86.

[31] S. S. Hajam and S. A. Sofi, “Iot-fog architectures in smart city applications: A survey,” *China Communications*, vol. 18, no. 11, pp. 117–140, 2021.

[32] F. Tariq, M. R. A. Khandaker, K.-K. Wong, M. A. Imran, M. Bennis, and M. Debbah, “A speculative study on 6g,” *IEEE Wireless Communications*, vol. 27, no. 4, pp. 118–125, 2020.

[33] R. C. Hansen, *Small Antenna Handbook*. Hoboken, NJ: Wiley, 1st ed., 2011.

[34] L. J. Chu, “Physical Limitations of Omni-Directional Antennas,” *Journal of Applied Physics*, vol. 19, pp. 1163–1175, 12 1948.

[35] J. Molins-Benlliure, E. Antonino-Daviu, M. Cabedo-Fabrés, and M. Ferrando-Bataller, “On-ground small ltcc chip antenna and its placement on iot devices,” *IEEE Antennas and Wireless Propagation Letters*, vol. 22, no. 9, pp. 2065–2069, 2023.

[36] A. Andújar, J. Anguera, and C. Puente, “Ground plane boosters as a compact antenna technology for wireless handheld devices,” *IEEE Transactions on Antennas and Propagation*, vol. 59, no. 5, pp. 1668–1677, 2011.

[37] S. Gao, Q. Luo, and F. Zhu, *Circularly Polarized Antennas*. IEEE Press, Wiley, 2014.

[38] X. Lu, P. Wang, D. Niyato, D. I. Kim, and Z. Han, “Wireless networks with rf energy harvesting: A contemporary survey,” *IEEE Communications Surveys & Tutorials*, vol. 17, no. 2, pp. 757–789, 2015.

[39] N. Ojaroudi Parchin, H. Jahanbakhsh Basherlou, Y. I. A. Al-Yasir, R. A. Abd-Alhameed, A. M. Abdulkhaleq, and J. M. Noras, “Recent developments of reconfigurable antennas for current and future wireless communication systems,” *Electronics*, vol. 8, no. 2, 2019.

[40] T. N. Le, A. Pegatoquet, T. Le Huy, L. Lizzi, and F. Ferrero, “Improving energy efficiency of mobile wsn using reconfigurable directional antennas,” *IEEE Communications Letters*, vol. 20, no. 6, pp. 1243–1246, 2016.

[41] L. Swaminathan, “Rf mems switch fabrication and packaging,” in *Nanofibers* (B. Kumar, ed.), ch. 15, Rijeka: IntechOpen, 2020.

[42] A. S. Sedra and K. C. Smith, *Microelectronic Circuits*. Oxford University Press, 7th ed., 2014. Discussion on PIN diodes.

[43] *Nonideal Behavior of Components*, ch. FIVE, pp. 299–376. John Wiley & Sons, Ltd, 2005.

2 Circular Polarization

2.1 Introduction to CP

CP antenna technology is critical in modern wireless systems. It is largely employed in localization, WSN, RFID, wireless power transmission, Television broadcasting systems applications. It is becoming critical in modern wireless systems because it helps to address the issues of:

- Orientation Independence: The signal is transmitted in all planes, increasing the probability of a successful link regardless of the relative orientation of the transmitter and receiver, unlike linearly polarised antennas.
- Multipath Fading Mitigation: When a CP wave is reflected off a surface, its polarisation sense is reversed. A CP antenna designed to receive a specific polarization will inherently reject the opposite sense, effectively reducing the impact of reflections and multipath interference
- Signal Integrity Enhancement: signal attenuation, absorption losses, and signal interference are reduced due to the a more reliable and robust channel.

CP is a property of electromagnetic waves describing the orientation of the electric field vector as the wave propagates when the field vector at a point describes a circle as a function of time [1]. Three conditions are to be fullfilled to obtain a circular polarized wave:

1. The electric field $\bar{E}$ must have two orthogonal linear components,
2. The two components must have same magnitude,
3. The two components must be time-phased shifted of odd multiples of 90°

The sign of the phase difference between the components defines whether the electric field vector rotates clockwise (positive) or anti-clockwise (negative), thus the wave is either Right Handed Circular Polarization (RHCP) or Left Handed Circular Polarization (LHCP), respectively.

A widespread method to generate two orthogonal components is to excite orthogonal modes, e.g. TM10 and TM01 on micro-strip patch antennas. The 90° phase shift is generally induced through external polarization circuits like hybrid couplers, power dividers with offset feeding lines [2]. This method is commonly used due to its straightforward application, but it often leads to more complex and larger structures.

However, CP can be achieved on micro-strip patches with a single feed using geometry tweaking as corner truncation, incorporating slotted patches or grounds or introducing slits. However, these modifications often result in a narrower Axial Ratio (AR) bandwidth and an increased sensitivity to variations in the permittivity of the dielectric substrate and the dimensions of the patch.

2.1.1 OCP Antennas for IoT

In order to obtain a CP while keeping a dipole-like (omnidirectional) radiation pattern, the E-field components E_θ and E_ϕ must have the same magnitude and a phase difference of odd multiples of 90° in each point of the azimuth plane [1].

In literature, different OCP antenna designs have been proposed over the years. In [3], using a coaxial cable for E_θ and a spiral slot over a surrounding shield for E_ϕ, a wideband flat OCP radiation with a 10.2 dBic maximum realized gain is obtained. However, the overall length of the structure (8.6λ) is not negligible. Similarly, surrounding a coaxial cable with radial CP loops [4] [Figure 2.1.1 (a)], the profile of the antenna is reduced to 1.57λ keeping a high gain and wide bandwidth of 3.57%. In both cases, the use of the coaxial cable puts a strong constraint in terms of manufacturing and robustness of the structure, but it develops a flat omnidirectional pattern, able to get high realized gain in the azimuth plane. A high gain can be also obtained by combining multiple OCP elements in arrays, as in [5, 6] [Figure 2.1.1 (d)]. However, the size of these structures remains remarkable, and not suitable for IoT devices.

Lots of efforts have been done during these years to exploit CP on compact omnidirectional antennas [7–21]. The common theme to these designs is the composition of the CP as the combination of the two E-field components E_θ and E_ϕ generated by the compound of two antenna structures.

A combination of a slot and a modified Planar Inverted F Antenna (PIFA) is proposed in [7] at this scope [Figure 2.1.1 (c)]. The need, however, for a fourfold parallel waveguide power divider and 90° phase-shifter in the printed feeding network may be demanding to manufacture. A modified shorted patch and two strips, acting respectively as a magnetic and an electric source of current to develop an OCP radiation pattern are combined into a single structure in [8]. Even though the resulting antenna is easy to manufacture, the dimension of the strips ($\lambda/4$) implies an overall structure length of 1.8λ.

In [9], E_θ is excited by the TM_{01} mode of a Dielectric Resonator Antenna (DRA), while E_ϕ is due to the horizontal currents on logarithmic spiral slots in the ground plane. Similarly, in [10], E_θ is still generated by a DRA, while E_ϕ is provided by an Alford Loop (AL) placed on the top of the DRA [Figure 2.1.1 (e)]. Despite the typical large bandwidth of DRA s, these antennas present a high profile compared to other solutions proposed in the literature.

Low profile ($< 0.028\lambda$) antennas utilize a single-layer substrate circular patch, integrating vias and slits for the vertical E_θ and E_ϕ components respectively [11–13]. Similarly, the horizontal component can be induced from spiral slot shapes carved on a shorted patch radiator (responsible for the vertical E_θ component) [14, 15] [Figure 2.1.1 (b)]. These antennas can provide a wide bandwidth (>14.8%) but their surface is greater than $0.75 \times 0.75\lambda^2$ [12, 15]. Reducing the surface of this type of antenna would imply giving up on the bandwidth [11, 14]. A solution to reduce surface and keep a wide bandwidth is proposed in [13]. Increasing the volume of the antenna using stacked shorted patches with slits, a 32.5% usable bandwidth is obtained. However, the antenna section increases to half a wavelength.

Another way to generate the E_ϕ component is using sets of branches to compose horizontal dipoles, as in [16–18], where in both cases E_θ is due to vertical shorting pins. The $\lambda/2$ length of the branches in addition to the presence of a feeding line in [16] [Figure 2.1.1 (g)] or a transmission line phase-shifter in [17] [Figure 2.1.1 (i)] impose a constraint on the antenna surface, which becomes greater than $0.6\times0.6\lambda$.

A flexible structure is achieved in [18], by avoiding the presence of vertical pins (excluding the feeding one). Meandered lines are printed on the flexible substrate to well match with the branch lines. However the size of the structure is still important ($0.55 \times 0.55 \times 0.2\lambda$).

In [19] the function of the branches is achieved by using 3D folded monopoles greatly reducing the overall antenna size $0.22 \times 0.22 \times 0.076\lambda^3$. However, despite the good performances in terms of bandwidth (3.89%) and gain (1.59dB), the structure may be fragile due to the unsupported metal wires acting as folded monopoles.

Another solution is to use two shorted parallel Printed Circuit Boards (PCBs) arranging the branches on a loop. As an example, the antenna proposed in [20] has an overall size that is remarkably small ($0.16\lambda \times 0.16\lambda \times 0.03\lambda$), but the usable bandwidth is narrow (only 0.9% at 1.435 GHz), and the combination between the orthogonal field components requires the integration of a feeding network. The use of a feeding network is avoided in [21] by properly selecting the distance between the vertical shorting vias and the feeding pin [Figure 2.1.1 (f)]. The antenna combines a Zeroth-Order Resonance (ZOR) and a modified AL obtaining a 1.5 dBic maximum gain and 6% bandwidth at the cost of a larger size ($0.4\lambda \times 0.4\lambda \times 0.08\lambda$).

2.1.2 Reconfigurable OCP Antennas

When it comes to OCP polarization reconfigurable antennas, the planar size of the antenna become significant (greater than $0.58 \times 0.58\ \lambda$) [22–25].

In the work by [22], a shorted patch is combined to slots. Divided into 6 sectors, it uses 24 PIN-diodes to reconfigure the CP. By using four diodes per sector and activating two at a time, it can change the shape of the slot, making the current flow in opposite directions and alterating the E_ϕ component while keeping the E_θ fixed due to the shorted patch. Although the size of this antenna is comparable to the wavelength, it achieves a wide usable bandwidth of 19.8%.

A combination of a top-loaded dipole and 12 radial loops is proposed in [23]. The design consists of two circular, symmetrical PCB, each with a central circular dipole load and six loops. It incorporates 48 PIN-diodes, four per loop, to develop RHCP and LHCP at 1.575 GHz. It has a large bandwidth of 13% for its relatively small size of $0.58 \times 0.58 \times 0.08\ \lambda^3$. The size affects the gain, which is measured to be 0.15 dBic at most. A wheel-shaped antenna, also made on separate PCB substrates, is presented in [24]. It is composed of a central patch and eight surrounding loop stubs that act as magnetic dipoles, enabling the generation of CP conical-beam radiation. Both Linear Polarization (LP) and CP can be generated reconfiguring the antenna's electrical structure through 64 PIN-diodes placed on the coupling loop stubs. The large substrate size of $1.8 \times 1.8\ \lambda^2$ helps to widen the bandwidth up to 15%, but it also affects the radiation pattern shape, resulting in a conical rather than omnidirectional shape.

In [25], a low profile shorted patch with three curved branches uses just six diodes to reconfigure LHCP or RHCP at 2.49 GHz. The antenna is composed of a parallel circular cavity, dual arc arms, and shorted vias. Printed on both sides of a single PCB its size is just $0.4 \times 0.4 \times 0.17\ \lambda^3$, resulting in a limited usable bandwidth of 1.3%. A five H-plane horn structure have been combined with parallel strips controlled by PIN-diodes to achieve LHCP and RHCP reconfiguration in [26]. The antenna is printed on two sides of a single-layer PCB and includes a phase-shifter between the switchable strips and the horn section, tuned to make relative E-field components orthogonal. Designed to operate at 2.45 GHz, the antenna exhibits a 2.9% bandwidth and a realized gain of -0.5 dBic. However, the results from [25, 26] are only simulated.

Taking inspiration from static OCP antenna structure described in [16], polarization reconfiguration through PIN-diodes is proposed by [27]. This approach employs 12 diodes in the feeding network to achieve horizontal and vertical LP, as well as RHCP, and LHCP polarization reconfiguration over a 28.6% overlapped bandwidth. This compact antenna has a dimensions of $0.35 \times 0.35 \times 0.084\ \lambda^3$, although its realized gain is limited to around 0 dBi for CP configurations.

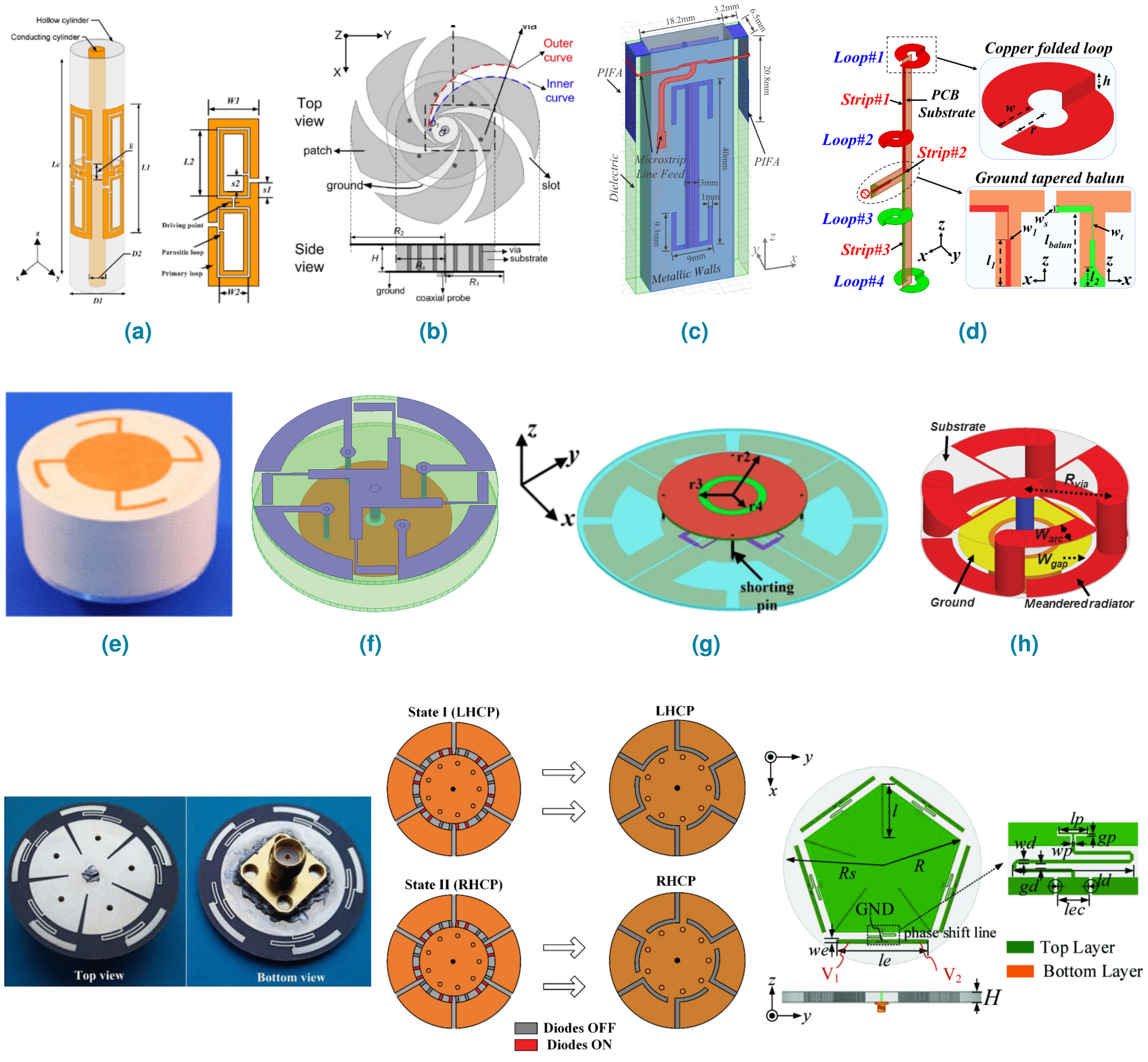

(a) (b) (c) (d)

(e) (f) (g) (h)

(i) (j) (k)

Figure 2.1.1: Examples of OCP antennas: (a) A coaxial cable surrounded by radial CP loops [4], (b) a wide-band combination of vortex slots and shorting vias [14], (c) A combination of a slot and a modified PIFA [7], (d) a high gain array of OCP elements [5] , (e) as combination of DRA top-loaded with AL [10], (f) with a ZOR and modified AL [21], (g) which combines top loaded monopole and arc dipoles fed through impedance matching network [16], (h) a miniature OCP antenna with meandered branches [28], (i) a printed sector-shaped OCP antenna with integrated phase-shifter transmission line to branches [17], and polarization reconfigurable OCP antennas: (j) a shorted patch with slots reconfigurable through 24 PIN-diodes [22], and (k) a five H-plane horn combined with reconfigurable parallel strips through 10 diodes [26]

2.2 Miniature OCP Antenna

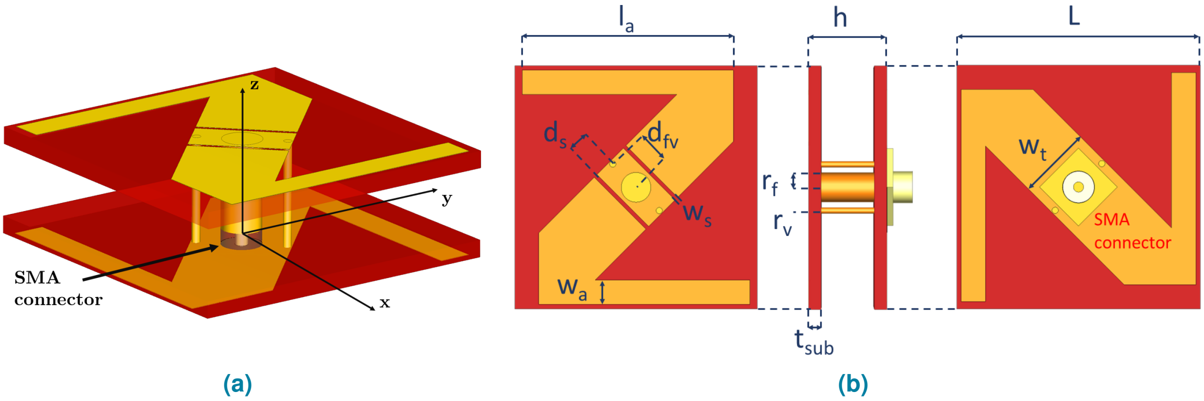

Figure 2.2.1: Structure of the proposed antenna with its fundamental parameters. (a) Perspective and (b) top, side, and bottom view projections.

The proposed antenna (Figure 2.2.1) is a combination of modified AL and Wire-Patch (WP) structures that can excite both E_ϕ and E_θ components, respectively, for the CP polarization at 2.45 GHz.

It is made of two single-layer PCBs with a Z-shape on each outer face at distance $h = 10$ mm. The lower Z-shape is connected to the SubMiniature version A (SMA) connector shield, while the SMA core is connected to a 4 mm wide copper cylinder, which is, in turn, connected to the upper Z-shape. Both layers present two shorting pins parallel to the central copper cylinder. Two slots are carved on the diagonal of the upper Z-shaped layer.

The proposed design is based on the structure introduced by Alford [29], which provides an omnidirectional horizontally polarized far-field. Since currents $J_1 = J_2$ flows in opposite direction, the only constructive currents effects are given by the currents on the arms, namely J_m, that in fact compose the loop, with a current $J_{m1} = J_{m2}$.

The antenna design process relies on 3 main steps. First, a modified Z-shaped AL structure with coaxial feeding is inspected for the generation of E_ϕ. Then, vias are introduced parallel to the central feeding to realize a WP element and thus excite the E_θ component. Finally, slots are introduced in the Z-shaped AL upper layer to tune the E-field components to have the same magnitude at 2.45 GHz, thus enabling an OCP radiation behavior.

The modified two-layer Z-shaped AL structure can be seen as a combination of two folded dipoles in each layer. In order to ease the antenna manufacturing process, the SMA connector is soldered on the bottom layer, causing an asymmetry with respect to balanced resonant structures. As a matter of fact, the feeding point is located on the bottom layer, and the copper cylinder is therefore responsible for an increase of the electrical length of the upper layer. This emerges in Figure 2.2.2 where simulated S-parameters of the three design steps are presented. For the AL case, the $|S_{11}|$ presents two minima, at 3.41 and 4.1 GHz. The far-field behavior in the azimuthal plane at these frequencies, shown in Figure 2.2.3, confirms that the horizontal radiation is mainly driven by the folded dipole resonance, while the separation between the two peaks is given by the electrical length difference introduced by the feed.

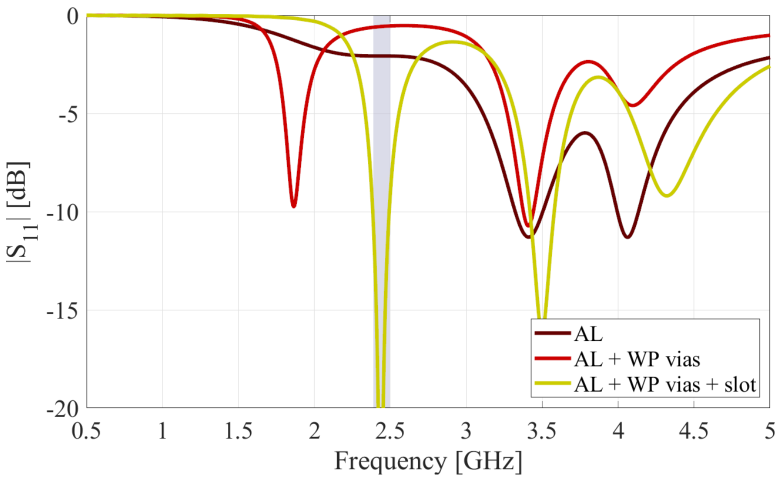

Figure 2.2.2: Antenna impedance matching behavior during the 3 main design steps with highlighted design band.

When vias are introduced to integrate the WP structure, another $|S_{11}|$ minimum appears at 1.86 GHz. As shown in Figure 2.2.4, at this frequency the E_θ is excited by the current on the vias. This behavior was expected since, as in a typical WP structure [30], the two shorting wires between the two PCBs act as two equivalent parallel inductance to the capacitance made by the parallel printed Z-shapes. The resulting equivalent circuit allows the main currents to flow through the short circuit wires, which become responsible for the desired typical omnidirectional vertically polarized radiation pattern.

Finally, two slots are carved on the central trunk of the top Z-shaped strips. These slots represent an additional degree of freedom to find the proper balance between the AL and the WP radiation characteristics, and consequently, a good impedance matching in the desired band.

In Figure 2.2.2, the peaks due to folded dipoles are still present and mainly unchanged. The first $|S_{11}|$ minimum responsible for the E_θ component instead is shifted to 2.45 GHz. Nevertheless, from Figure 2.2.5 it appears that at this frequency the E_ϕ component is now excited too, with an elliptical shape due to the diagonal trunk, resulting in an overall azimuthal CP radiation behavior.

As an additional confirmation of this last statement, Figure 2.2.6 shows the amplitude and phase of the E-field components in the azimuth plane ($\theta = 90°$) at 2.45 GHz. The well-balanced AL and WP sources of the antenna structure compose a stable 90° phase shift between the E_θ and E_ϕ across the whole azimuth plane. The oscillations on the E_ϕ amplitude component can be addressed to the elliptical shape of the E_ϕ component azimuthal cut. In Figure 2.2.6, the RHCP is revealed due to the positive difference between E_θ and E_ϕ.

2.2.1 Parameters Optimization

All the antenna geometrical parameters have been optimized with the aim of obtaining a good impedance matching as well as a good CP level in the 2.4 GHz ISM band, i.e.,

$$\begin{cases} |S_{11}(f)| \leq -10 \text{ dB} \\ AR(f) \leq 3 \text{ dB} \end{cases} \qquad 2.4 \leq f \leq 2.5 \text{ GHz}. \tag{2.2.1}$$

The optimization has been carried out through a parametric study, whose main results are reported in

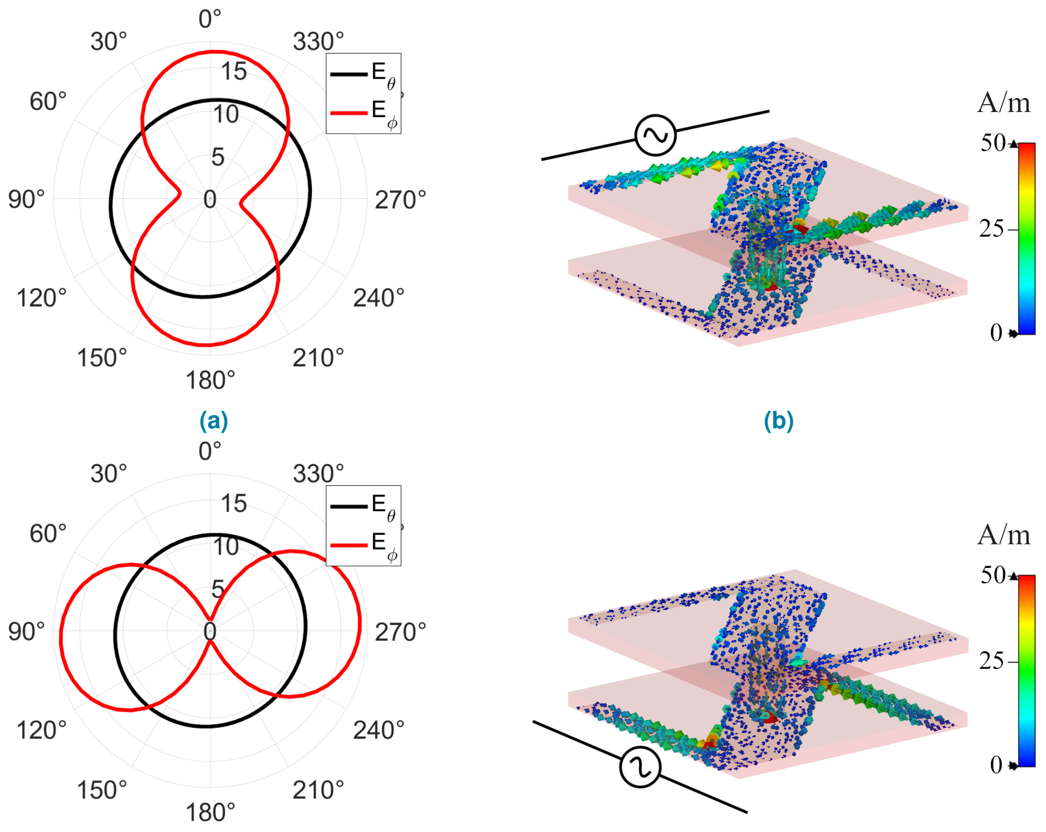

(a) (b)

(c) (d)

Figure 2.2.3: Design step #1: modified AL structure. (a)(c) θ = 90° E-field far-field cut [dB (V/m)] along with correspondent (b)(d) current distribution at (a)(b) 3.41 GHz and (c)(d) 4.1 GHz.

Table 2.2.1: Optimized antenna geometrical parameter values

param. name	L	h	l_a	W_a	W_t	d_s	W_s	r_f	r_v	d_{fv}	t_{sub}
value [mm]	31	10	27	3.1	9.36	2.4	0.4	2	0.4	2.1	0.8

the following. Figure 2.2.7 shows the effects of varying the main antenna geometrical parameters on both the $|S_{11}|$ and the AR. For each variation, the remaining geometrical parameters have been kept fixed to the values reported in Tab. 2.2.1.

The antenna resonance is mainly controlled by the length of the arms of the AL (l_a) and the distance between the top and bottom PCB layers (h). These two parameters are responsible for the antenna's overall horizontal and vertical extensions, respectively. Consequently, as their values increase (decrease), the antenna resonance shifts towards lower (higher) frequencies, as shown in Figure 2.2.7 (a) and Figure 2.2.7 (c). Concerning the AR, the variation of the antenna horizontal extension causes a frequency shift [Figure 2.2.7 (b)] that is in agreement with the one experienced by the $|S_{11}|$ parameter [Figure 2.2.7 (a)]. Differently, the effect of varying h on the AR is opposite [Figure 2.2.7 (d)] with respect to the one shown in Figure 2.2.7 (c). Varying the vertical extension of the antenna makes in fact varying both the inductive effect on the vias and the capacitive effect between the two PCBs, which are at the basis

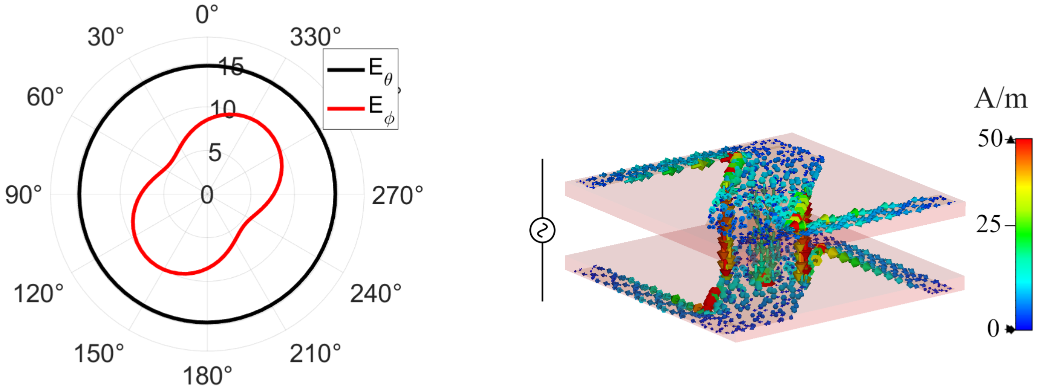

(a)

(b)

Figure 2.2.4: Design step #2: modified AL structure with vertical WP vias. (a) θ = 90° E-field far-field cut [dB (V/m)] along with correspondent (b) current distribution at 1.86 GHz.

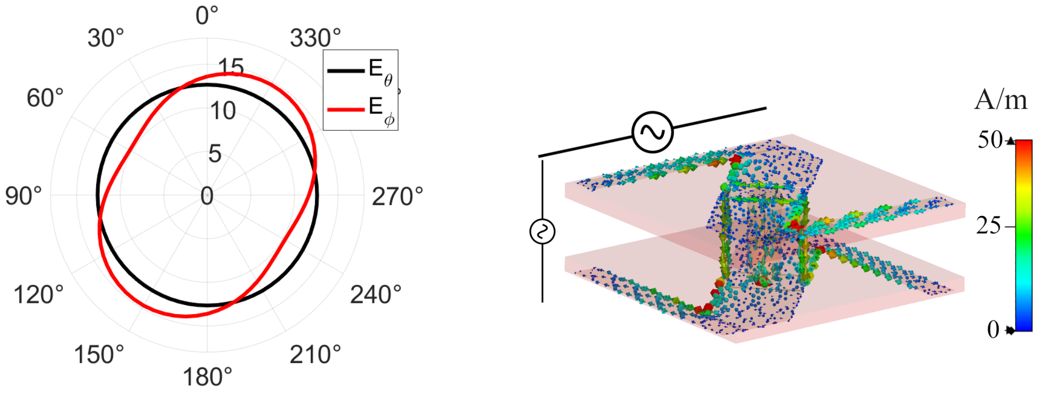

(a)

(b)

Figure 2.2.5: Design step #3: modified AL structure with vertical WP vias and slots. (a) θ = 90° E-field far-field cut [dB (V/m)] along with correspondent (b) current distribution at 2.44 GHz.

of the generation of the E_θ and the E_ϕ field components, respectively. Because of this behavior, the h parameter is fundamental to maximize the effectively usable bandwidth, which is the overlap between the impedance and the 3 dB AR bandwidths.

Concerning the impedance matching, this is mainly controlled by the radii of the short (r_v) and feeding (r_f) wires as well as by the short-feed distance (d_{fv}). As in a classical WP antenna, in fact, the proper design of the system composed by the feed and shorting wires allows the matching of the antenna input impedance to the port impedance, usually 50Ω. This is shown in Figure 2.2.7 (e), where the $|S_{11}|$ behavior for several d_{fv} values is reported. It must be pointed out that the variation of the short-feed distance has no effect on the CP [Figure 2.2.7 (f)].

Finally, as shown in Figure 2.2.7 (g), the width of slot cut (w_s) in the top z-shaped strip can be changed to fine tune the impedance matching, while the AR remains mostly unchanged [Figure 2.2.7 (h)]. On the other hand, the antenna AR can be optimized thanks to the width of the z-shape trunk and the slots' position, i.e., the length of the slot cut (w_t) and its distance from the center (d_s). These variations affect more the AR frequency shift [Figs. 2.2.7 (j), 2.2.7 (l)] rather than the resonance frequency shift [Figs. 2.2.7 (i), 2.2.7 (k)]. As a matter of fact, the balance between the amplitude of the horizontal currents

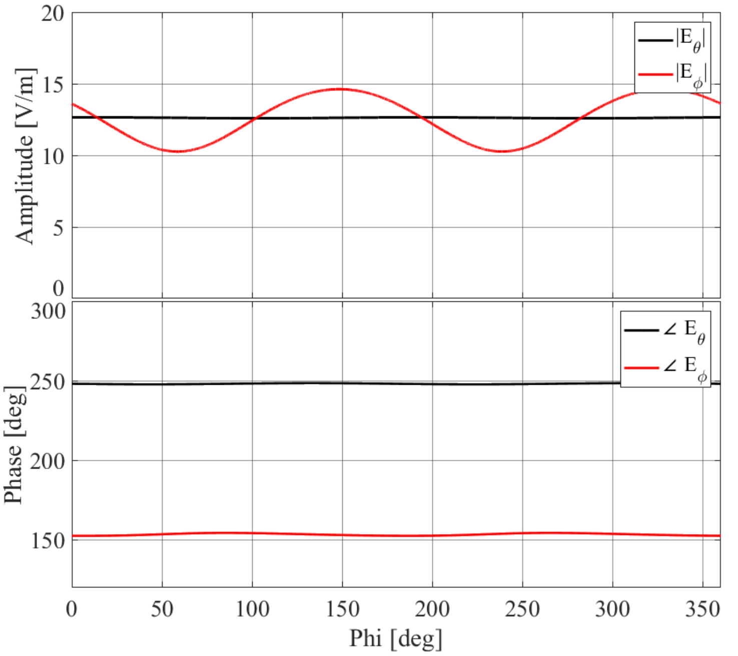

Figure 2.2.6: Amplitude and phase of E-field components across the azimuth $\theta = 90°$ plane.

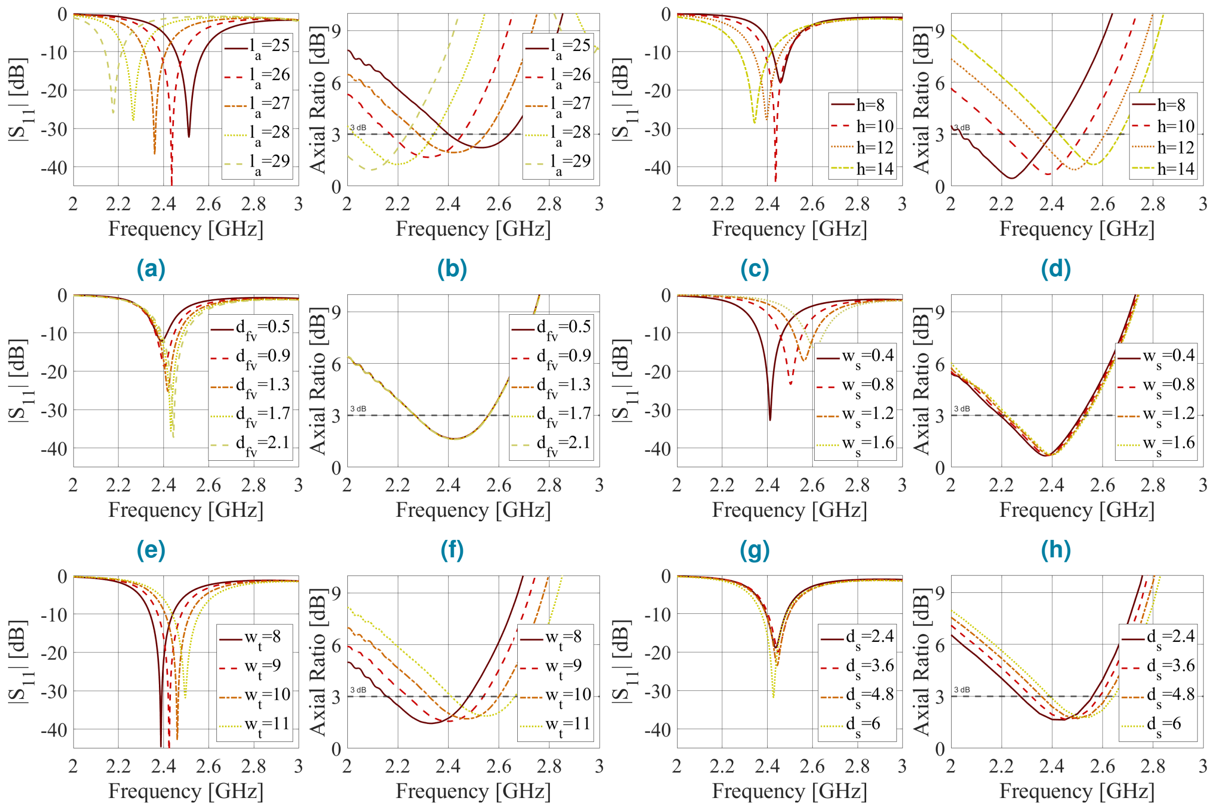

(a) (b) (c) (d)

(e) (f) (g) (h)

(i) (j) (k) (l)

Figure 2.2.7: Effects of varying the main antenna geometrical parameters on both the $|S_{11}|$ (left column) and AR (right column). All the values are in mm.

flowing on the z-shaped strips and the vertical currents flowing on the vias can be controlled by varying the position, length and width of the slot.

Based on this parametric analysis, the antenna optimization process was as follows. It first started with changing the AL arms' length l_a and PCB layers distance h to obtain a proper resonance and a low AR in the required frequency range. Successively, the optimal d_{fv} value was found, and finally, fine-tuning was performed by changing the trunk width w_t, the slot width w_s and position d_s. The final antenna geometrical parameter values are reported in Tab 2.2.1.

2.2.2 Circular Polarization Analysis

In order to verify the CP mechanism as a combination of horizontally and vertically polarized sources, Figure 2.2.9 shows the current distribution from bottom and side view respectively, for 4 equally-spaced time instants $t = nT/4$, $n = 0, 1...3$, T being the period at $f = 2.45$ GHz. Currents on the diagonal trunk are hidden for the sake of clarity, since it has been already showed how currents in the feeding lines of an AL offset each other in Figure 2.2.8 and [31].

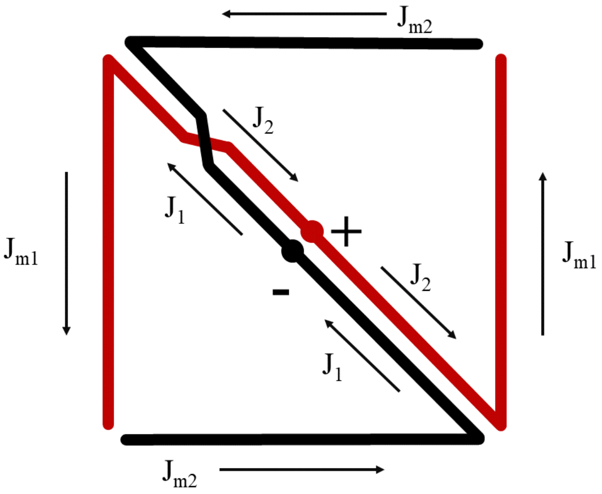

Figure 2.2.8: Alford Loop scheme with currents distribution.

Figure 2.2.9 (a) shows a strong clockwise current flowing at $t = 0$. In opposition, at the same time instant, the profile view in Figure 2.2.9 (b) shows a moderate intensity of current on the vias flowing from the lower PCB to the upper one. At this instant, the AL radiation, thus the horizontal E_ϕ component, is dominant compared to the WP one.

In Figure 2.2.9 (c) the current on the AL arms at $t = T/4$ is weaker than the one at the previous time instant. Figure 2.2.9 (d) instead shows an increase of current intensity on vias, meaning that now the vertical component becomes dominant compared to the horizontal one generated by the loop. Both currents flows in opposite direction compared to the previous case.

At $t = T/2$, the amplitude of the current flowing on the loop increases without changing its counter-clockwise direction, as shown in Figure 2.2.9 (e). Current on vias in Figure 2.2.9 (f) keeps its direction but becomes weaker. Again, the AL-generated E_ϕ component becomes dominant over E_θ.

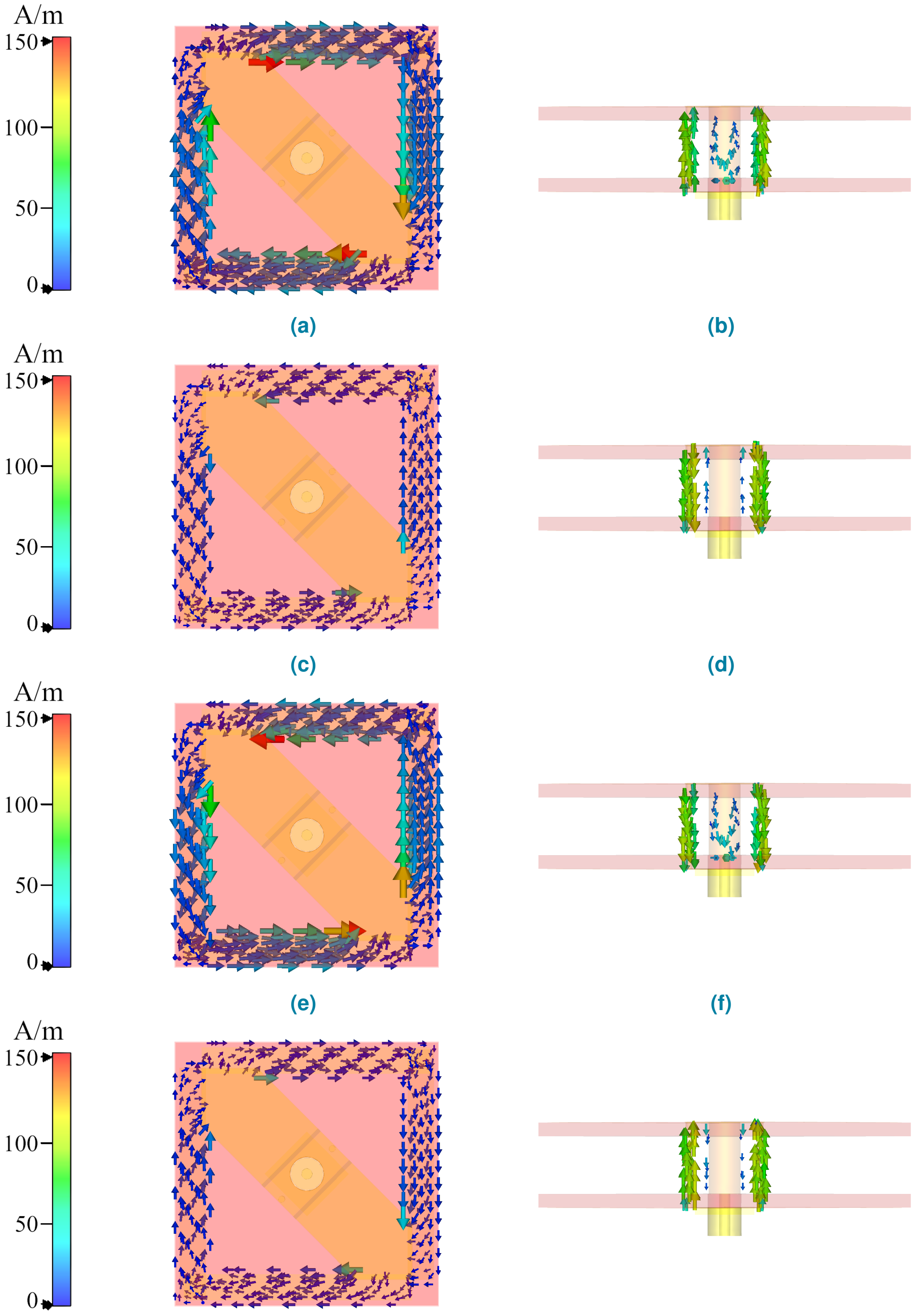

(a) (b)

(c) (d)

(e) (f)

(g) (h)

Figure 2.2.9: Surface current for $t = 0$ (a), (b), $t = T/4$ (c), (d), $t = T/2$ (e), (f) and $t = 3T/4$ (g), (h), on the Loop (left) and WPA vias (right) from bottom and side views, respectively.

Finally, at $t = 3T/4$, the current flow over the AL arms changes its direction to clockwise again and gets weaker in Figure 2.2.9 (g). As a consequence the current on vias in Figure 2.2.9 (h) changes its direction too and increases in intensity.

Based on such an analysis, we can affirm that the E_ϕ and E_θ components are 90° phased shifted by each other. As a matter of fact, each maximum (minimum) current intensity on vias is delayed by $T/4$ with respect to each current maximum (minimum) intensity on the AL arms.

2.2.3 Numerical and Experimental Results

The effectiveness of the proposed antenna has been numerically and experimentally assessed. All the simulations have been carried out using CST microwave studio electromagnetic simulator. As for the measurements, a prototype of the proposed antenna has been realized (Figure 2.2.10). The two PCBs have been printed using a Computer Numerical Control (CNC) milling process, and successively soldered to the vias with the help of a low-cost 3D printed PLA removable structure, which guaranteed the distance between layers and the accurate positioning of the vias. The S_{11} parameter was measured with a Keysight Vector Network Analyzer (Vector Network Analyzer (VNA)), while the radiation patterns were measured with a SATIMO Starlab system.

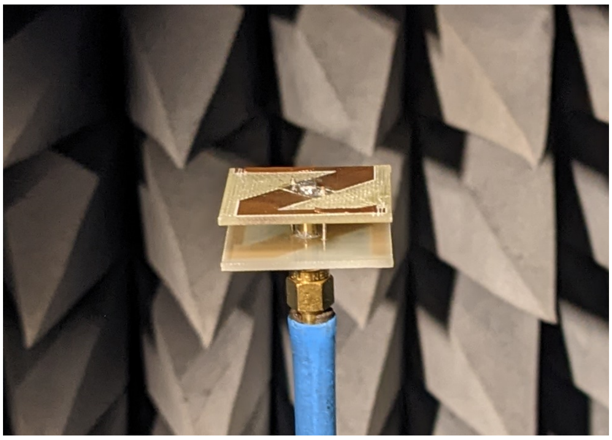

Figure 2.2.10: Antenna prototype during the measurements in the SATIMO Starlab system.

The comparison between simulated and measured values for both the reflection coefficient ($|S_{11}|$) and Total Efficiency is depicted in Figure 2.2.11. The antenna exhibits a good impedance matching in the desired band, with a simulated -10 dB matching band ranging from 2.38 to 2.49 GHz (4.6%). Measurements are in good agreement with the simulations, with the $|S_{11}|$ lower than -10 dB from 2.4 to 2.52 GHz (4.2%), thus covering the entire 2.4-2.5 GHz ISM band.

Despite the small dimensions, the antenna presents a simulated maximum total efficiency of 87% at 2.45 GHz, while the measured one is 86% at 2.48 GHz. The small frequency shift (only 1.6%), as in the case of the S_{11} parameter in Figure 2.2.11, can be ascribed to small imperfections in the realization of the prototype. Nevertheless, the measured antenna total efficiency is always higher than 70% all over the 2.4-2.5 GHz ISM band.

Finally, Figure 2.2.12 shows the simulated and measured antenna realized gain and AR patterns in both the azimuth and elevation planes at 2.45 GHz. The patterns are shown in terms of RHCP and LHCP gain components. In the azimuth plane, the simulated RHCP component is always at least 15 dB higher than the LHCP one. The shapes of the radiation pattern in the planes at $\theta = 90°$ [Figure 2.2.12 (a)], $\phi = 0°$ [Figure 2.2.12 (c)], and $\phi = 90°$ [Figure 2.2.12 (e)] confirm that the antenna exhibits a classical dipole-like RHCP behavior with an omnidirectional radiation behavior in the azimuth plane.

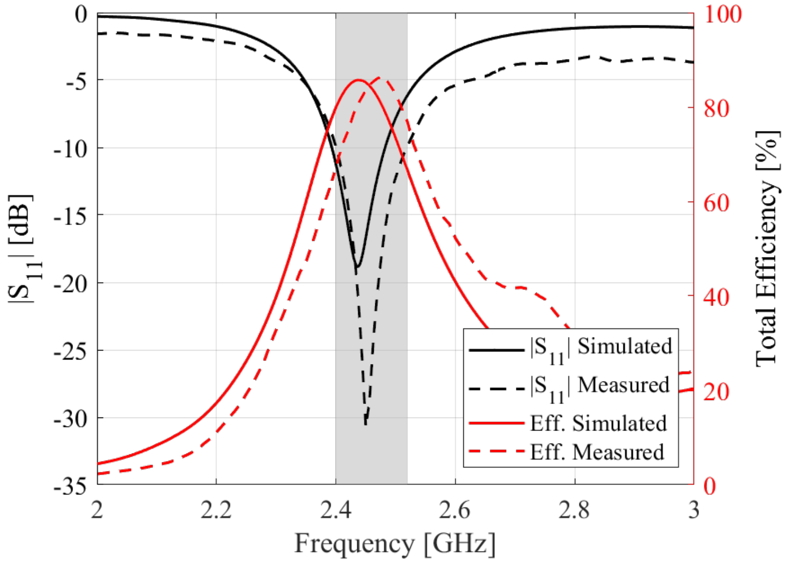

Figure 2.2.11: Simulated and measured antenna $|S_{11}|$ and total efficiency.

The elliptical shape of the RHCP radiation pattern is due to the intrinsic asymmetry of the antenna structure. The AL geometry used to excite the horizontally polarized radiation component consists of two Z-shaped metallic layers that are aligned only along one diagonal direction so that the currents at the center of the structure can cancel each other. Moreover, even the vias are placed along only one diagonal, thus further increasing the asymmetry of the antenna structure. As a result, the RHCP gain values are minimum (-0.24 dBic) at $\phi = 60°$ and $\phi = 240°$, and maximum (1.91 dBic) at $\phi = 150°$ and $\phi = 330°$.

Finally, it must be pointed out that measurements and simulations of the RHCP component are in very good agreement [black curves in Figs 2.2.12 (a), 2.2.12 (c), and 2.2.12 (e)]. Larger differences between simulated and measured curves are visible for the LHCP component [red curves in Figs 2.2.12 (a), 2.2.12 (c), and 2.2.12 (e)]. This is due to the fact that the small values of the LHCP component, i.e., the cross-polar component [always less than -10 dB in Figure 2.2.12 (a), and always less than -15 dB in Figs. 2.2.12 (c), and 2.2.12 (e)] suffer more from the imperfections of the prototype and from the accuracy of the measurement system.

On the right column of Figure 2.2.12, the AR is displayed calculated from the RHCP and LHCP components through the following equation [32]:

$$AR_{dB} = 20 \log_{10} \frac{E_{RHCP} + E_{LHCP}}{E_{RHCP} - E_{LHCP}} \tag{2.2.2}$$

The AR pattern in the azimuth cut reported in Figure 2.2.12 (b) shows an average of 4.1 dB AR. Despite being 2 dB higher than the simulated value, it still grants a fair elliptical polarization. This behavior is kept also in the elevation planes [Figure 2.2.12 (d) and Figure 2.2.12 (f)], in the range between $\theta = 20°$ and $\theta = 135°$, ensuring an elliptical polarization over a vertical beamwidth of 115°.

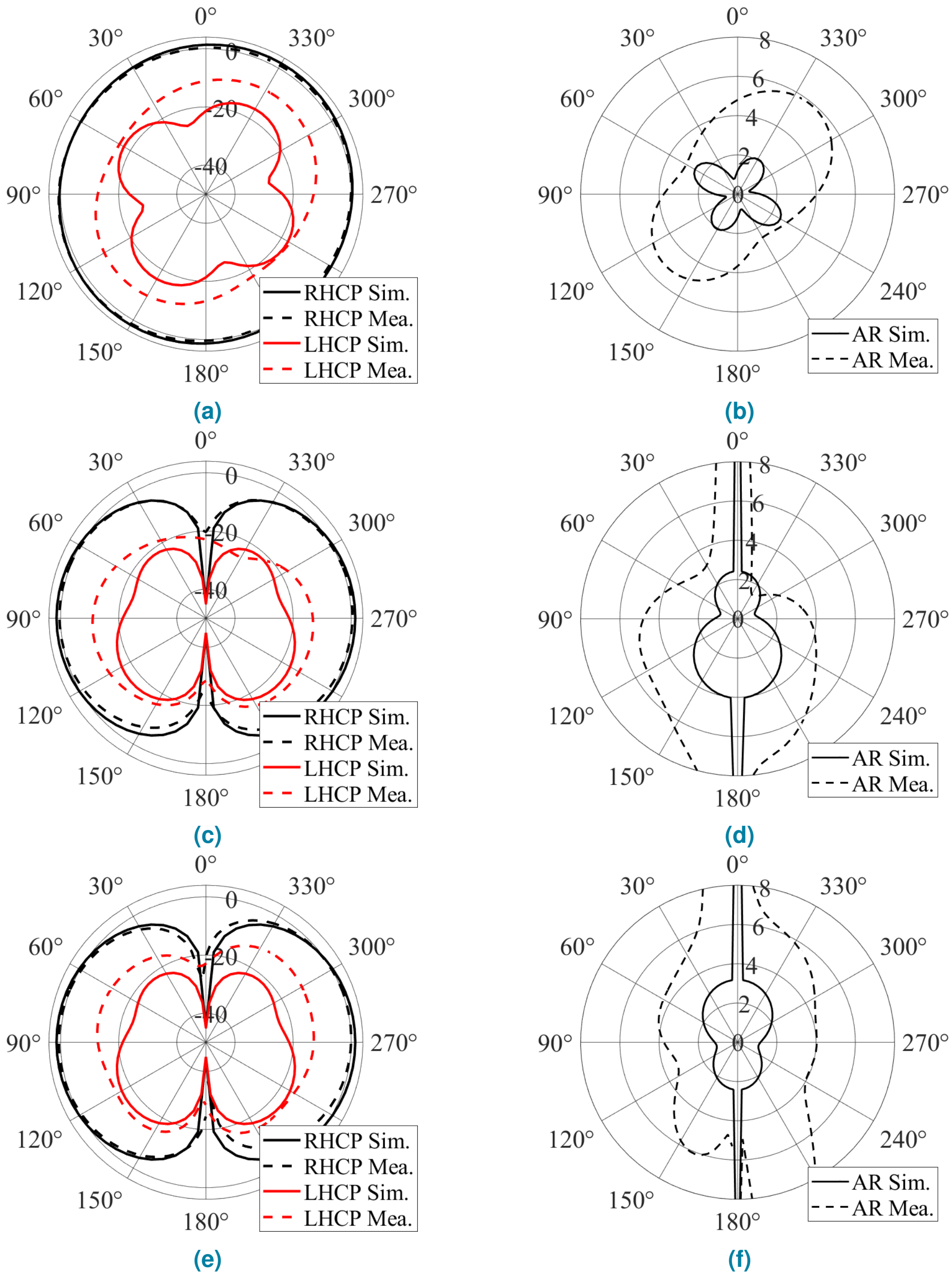

(a) (b) (c) (d) (e) (f)

Figure 2.2.12: Simulated and measured antenna RHCP and LHCP realized gain (left) and AR (right) patterns in planes at $\theta = 90°$ (a), (b), $\phi = 0°$ (c), (d), and $\phi = 90°$ (e), (f).

Table 2.2.2: Comparison of the main OCP antenna solutions available in literature

Ref	Type	Frequency [GHz]	Usable BW* [% / GHz]	Size [λ]	Gain [$dBic$]	Efficiency [%]
[8]	λ/4 shorted patch	5.8	4.3 / (5.63 – 5.88)	1.8 × 0.32 × 0.04	3	70
[9]	DRA + Spiral Slots	2.44	7 / (2.35 – 2.52)	0.5 × 0.5 × 0.17	1.3	87
[10]	DRA + Alford Loop	2.44	7 / (2.34 – 2.51)	0.38 × 0.38 × 0.18	1.8	93
[11]	shorts + V slits	5.8	3.5 / (5.65 – 5.85)	0.52 × 0.52 × 0.026	1.26	90
[12]	shorts + slits	2.4	14.8 / (2.26 – 2.62)	0.75 × 0.75 × 0.028	0.7	72
[13]	shorts + slits	1.385	32.5 / (1.16 – 1.61)	0.34 × 0.34 × 0.5	2.1	85
[14]	shorts + spiral slot	1.65	0.48 / (1.646 – 1.654)	0.33 × 0.33 × 0.017	0.1	68
[15]	shorts + spiral slot	2.73	51.7 / (2.11 – 3.58)	0.85 × 0.85 × 0.14	1	/
[16]	shorts + arc dipoles	1.95	25.6 / (1.7 – 2.2)	0.61 × 0.61 × 0.066	-1.12	/
[17]	shorts + branches	5.8	4 / (5.68 – 5.91)	0.62 × 0.62 × 0.03	1.77	97
[18]	feed pin + branches	5.8	2.9 / (5.72 – 5.89)	0.55 × 0.55 × 0.2	2.1	73
[19]	folded monopoles	2.44	3.9 / (2.395 – 2.49)	0.22 × 0.22 × 0.076	1.59	/
[20]	shorts + loop	1.435	0.9 / (1.429 – 1.442)	0.16 × 0.16 × 0.03	1.01	/
[21]	ZOR + loop	2.44	6.1 / (2.38 – 2.53)	0.4 × 0.4 × 0.08	1.95	/
This work	WP + AL	2.45	4.9 / (2.4 – 2.52)	0.25 × 0.25 × 0.08	1.91	87

*The usable bandwidth (BW) is defined as the overlap between the $|S_{11}| \leq -10$ dB and the $AR \leq 3$ dB antenna frequency bands.

2.3 Miniature Reconfigurable OCP antenna

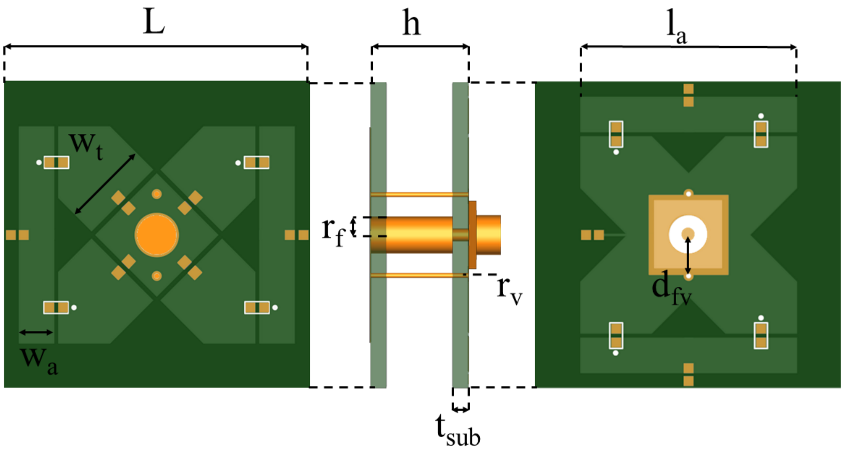

Figure 2.3.1: Geometry and fundamental parameters of the proposed antenna.

Based on the same principle of combining modified AL and WP structures to excite both E_ϕ and E_θ components respectively for the CP polarization presented in the previous section 2.2, a work which includes PIN-diodes based reconfiguration in RHCP and LHCP was first proposed in [C3] for 868 MHz LoRa application and it is presented in the current section for 2.4 GHz ISM band.

The antenna reconfiguration consists of activating symmetric Z-shaped modified AL structure in order to invert the current flow on the loop, thus affecting the horizontal E-field component of the CP while keeping the WP unchanged.

Referring to Figure 2.3.1, the proposed antenna is made of two single-layer, low-cost, 1.6mm thick FR-4 PCBs with a X-shape on each outer face at distance $h = 10mm$. The upper layer is fed by an SMA connector core through a 4 mm wide copper cylinder. The lower X-shape is connected to the ground of the SMA connector, and both layers have two shorting pins parallel to the central feeding cylinder. Finally, slots are carved on the upper layer. The fundamental design parameters are reported in 2.3.1.

Table 2.3.1: Antenna geometrical parameter values

param. name	L	h	l_a	W_a	W_t	r_f	r_v	t_{sub}	d_{fv}
value [mm]	31.2	10	22	3.6	8.86	2	0.25	1.6	4.15

2.3.1 Reconfiguration Mechanism

Four PIN-diodes are placed on each PCB between the X-shape and the arms in alternate order as illustrated by the bias pin indicators in Figure 2.3.2, which also represents the polarization reconfiguration scheme.

In Figure 2.3.2 (a) and 2.3.2 (b), the configuration for RHCP propagation is presented. The X-shape of each PCB depicted in dark green, is naturally connected together by the WP vias, resulting in the same 0 V voltage. The loop arms, depicted in red, are supplied with bias voltage so that diodes D2, D4,

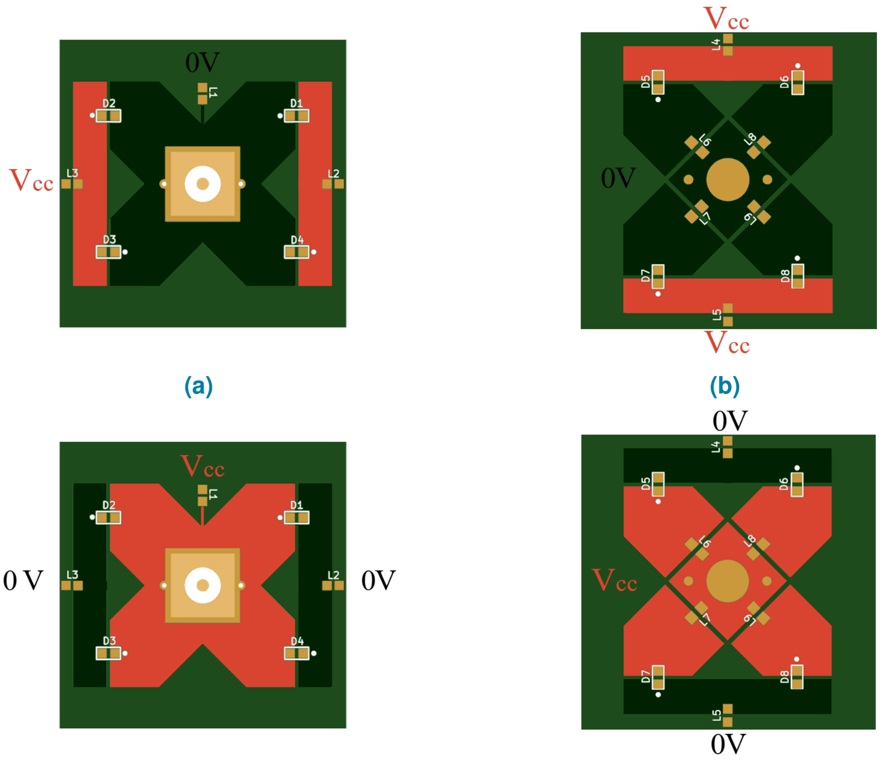

(a) (b) (c) (d)

Figure 2.3.2: Reconfiguration Diodes bias scheme for RHCP (a), (b) where D2, D4, D6 and D7 are forward biased and LHCP (c), (d) where, on the opposite, D1, D3, D5 and D8 are forward biased.

D6 and D7 are forwardly biased, while the other diodes are inversely biased, effectively acting as Open Circuit (OC). RF chokes inductances, depicted as L1-L9 in Figure 2.3.2, are necessary on both the top and on the bottom PCB to extend the 0 V voltage across the slots and to prevent RF leakage from the antenna structure. A value of 100 nH have been chosen as it guarantees a sufficiently high reactive impedance $Z_L = j\omega L \simeq 1.5k\Omega$.

In Figure 2.3.2 (c) and 2.3.2 (d), the same principle is applied at reversed voltages, thanks to the structural symmetry, allowing for the activation of the opposite diodes: D1, D3, D5, and D8 while D2, D4, D6, and D7 are turned off.

Nevertheless the PIN diodes reconfiguration implies changes only on the PCBs in a symmetrical fashion; therefore it does not affect the current flow on the WP vias, which are responsible for the vertical E-field component. Consequently, the considerations for the CP reconfiguration analysis take into account only the AL arms.

In Figure 2.3.3 (a), the current distribution on the arms for the first configuration (D2, D4, D6, and D7 on) is presented. This counter-clockwise loop current, combined with the WP structure, develops a RHCP propagation. The result of inverting the biasing (D1, D3, D5, and D8 on) is shown in Figure 2.3.3 (b), where a perfectly symmetrical clockwise loop is present, thus developing LHCP propagation.

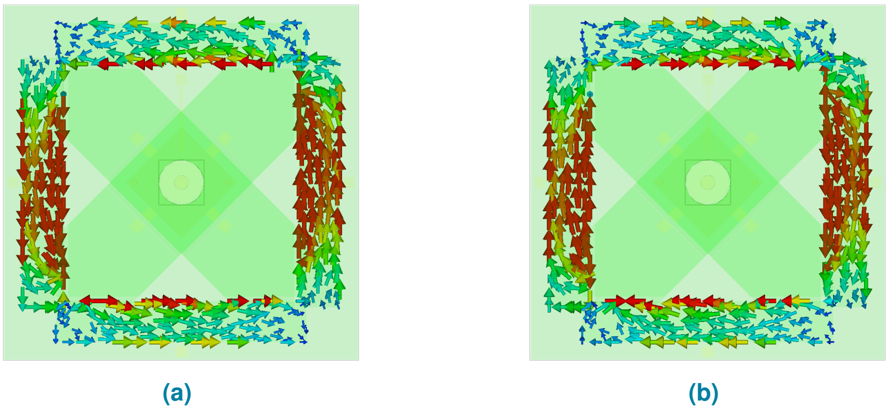

Figure 2.3.3: Bottom view of surface current on the antenna loop arms for same instant $t = 0$ when diodes are in biased for RHCP (a) and LHCP (b) showing a counterclockwise and clockwise current flow respectively.

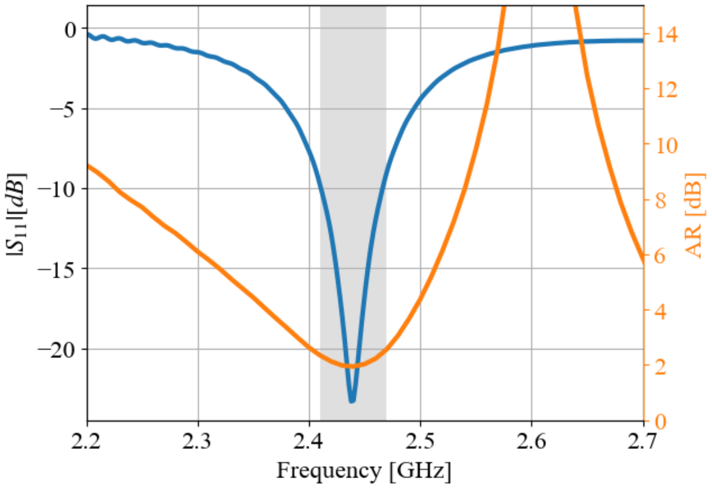

Figure 2.3.4: Simulated reflection coefficient and AR in $\phi = 0°$ and $\theta = 90°$ of the ideal antenna structure.

2.3.2 Numerical Results

Simulations have been carried out with the CST StudioSuite EM simulator, considering virtual Short Circuit (SC) and OC for forward-biased and reversed-biased PIN-diodes, respectively. The reflection coefficient and AR of a RHCP version is displayed in Figure 2.3.4, showing the antenna resonance in the 2.4 GHz ISM band and a usable bandwidth of 60 MHz (2.5%). These results indicate that the antenna performance is comparable to that of the non-reconfigurable version in the previous section 2.2.

Comparing these results with other examples of OCP reconfigurable antennas available in the literature, as reported in Table 2.3.2, the proposed antenna addresses several key points simultaneously, namely the number of diodes needed for reconfiguration and its miniaturization.

Similarly to [27], the proposed antenna draws inspiration from an OCP structure, introducing CP reconfiguration through PIN-diodes. However, in [27], the reconfiguration occurs within a complex feeding network, which may contribute to its low realized gain pattern of 0 dBic. The work of [24] achieves a 15% and can reconfigure CP and LP with 64 diodes. Its significant size of $1.8 \times 1.8\ \lambda^2$ and the presence of a

Table 2.3.2: Comparison of the main reconfigurable OCP antenna solutions available in literature

Ref	N diodes	Frequency [GHz]	Usable BW [% / GHz]	Size [λ]	Gain [$dBic$]	Pattern
[22]	24	2.4	19.8/ (2.09 – 2.55)	$0.93 \times 0.93 \times 0.024$	2.5	Quasi-omni
[23]	48	1.575	13/ (1.43 – 1.63)	$0.58 \times 0.58 \times 0.08$	0.15	Omnidirectional
[24]	64	4	15/ (3.6 – 4.2)	$1.8 \times 1.8 \times 0.2$	/	Conical
[25]	6	2.492	1.3/ (2.47 – 2.5)	$0.4 \times 0.4 \times 0.017$	0.8	Omnidirectional
[26]	10	2.45	2.9/ (2.42 – 2.49)	$0.55 \times 0.55 \times 1.2$	-0.5	Omnidirectional
[27]	12	2	28.6/ (1.65 – 2.2)	$0.35 \times 0.35 \times 0.084$	0	Omnidirectional
This work	8	2.4	2.5/(2.41 - 2.47)	$0.25 \times 0.25 \times 0.08$	1.3	Omnidirectional

*The usable bandwidth (BW) is defined as the overlap between the $|S_{11}| \leq -10$ dB and the $AR \leq 3$ dB antenna frequency bands.

large ground plane results in a conical radiation pattern. In comparison, the proposed antenna utilizes just 8 diodes and occupies 50 times less surface area. Similarly, [22] [Figure 2.1.1 (j)], also designed for 2.4 GHz, is controlled by 24 diodes and occupies a volume of $0.93 \times 0.93 \times 0.024$, which is 4 times larger than the proposed antenna. The 48-diodes reconfigurable OCP proposed in [23] has a small volume of $0.58 \times 0.58 \times 0.08\ \lambda^3$, yet it is still larger than the proposed antenna. One of the drawbacks of miniaturization, as discussed in Chapter 1, is the reduction of impedance bandwidth, which consequently limits the usable bandwidth. The proposed antenna has a very narrow usable bandwidth of just 2.5%, while the previously reported works have a usable bandwidth greater than 13%.

In [26], only 10 PIN-diodes are used to reconfigure the CP [Figure 2.1.1 (k)], and this number is reduced to just 6 in [25]. The small size of these antennas, not exceeding $0.55 \times 0.55\ \lambda^2$, limits the bandwidth to be narrow, at 1.3 % and 2.9 %, respectively. With a smaller size of $0.25 \times 0.25\ \lambda^2$ the proposed antenna has a comparable bandwidth of 2.5% and a higher gain.

2.3.3 Experimental Results

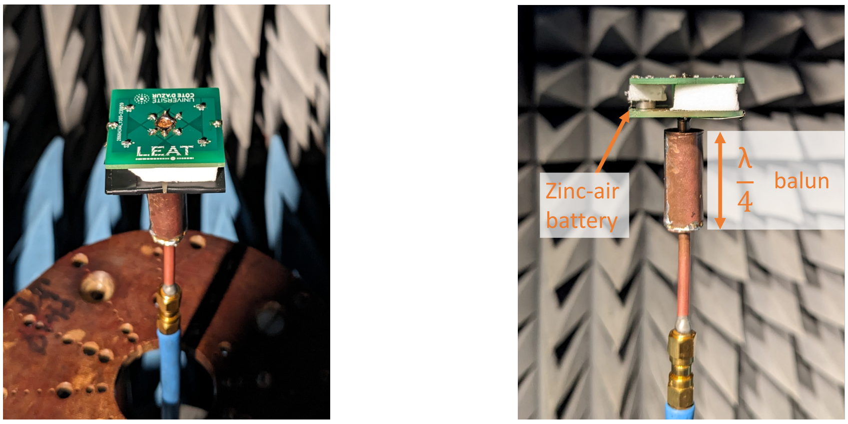

(a)

(b)

Figure 2.3.5: Antenna prototype during measurements in SATIMO Starlab system (a) and a side view to highlight the Balance-to-Unbalance (balun) and battery (b)

A prototype have been developed using Skyworks SMP1345 PIN-diodes and characterized in terms of reflection coefficient and radiation pattern with a Rohde & Schwarz VNA and a SATIMO StarLab system, respectively (Figure 2.3.5).

The measured prototype integrates a zinc-air battery as a control mechanism for the PIN-diodes within the antenna structure. This integration eliminates the need for external wires, thus reducing the potential for interference and unwanted radiation at a cost of a limited current supply.

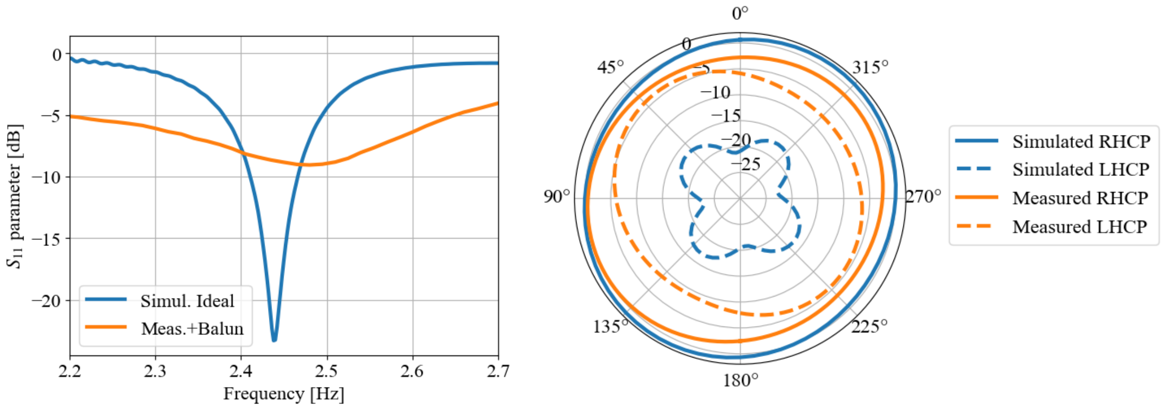

(a)

(b)

Figure 2.3.6: Comparison between simulation and measurements of reflection coefficient (a), and realized gain in azimuthal cut $\Theta = 90^\circ$ at 2.44 GHz (b) of the antenna in RHCP reconfiguration state

During measurements, the need for a balun became apparent to achieve acceptable values due to the compact antenna size. A 60 mm long rigid coaxial cable with a 3 mm cross-section was directly soldered to the antenna structure. The $\lambda/4 = 31.2$ mm long sleeve, with a radius of 13 mm, is placed with the open end against the antenna structure, as presented in Figure 2.2.10 (a).

Measured S_{11} from Figure 2.3.6 (a) shows significant influence from losses, with a minimum at 2.47 GHz. Part of the losses can be attributed to the presence of the balun, but further considerations need to be made concerning the well functioning of the antenna. Moreover, in the far-field, Figure 2.3.6 (b) shows a decrease in the CP omnidirectional radiation, with a difference of 18 dB between RHCP and LHCP in simulation, compared to a minimum of 1 dB difference in measurements, indicating that no CP is developed.

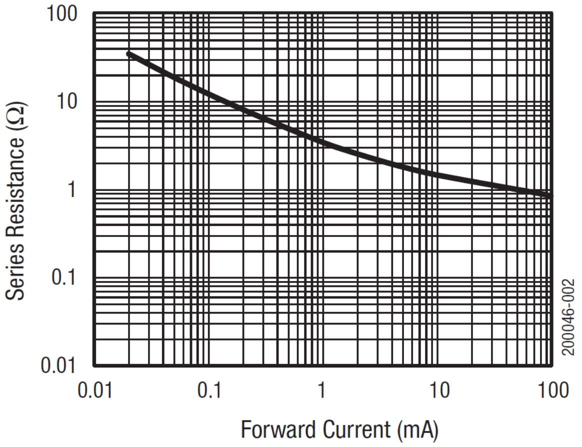

Figure 2.3.7: Series resistance vs. Current for the Skyworks SMP1345 diode [33]

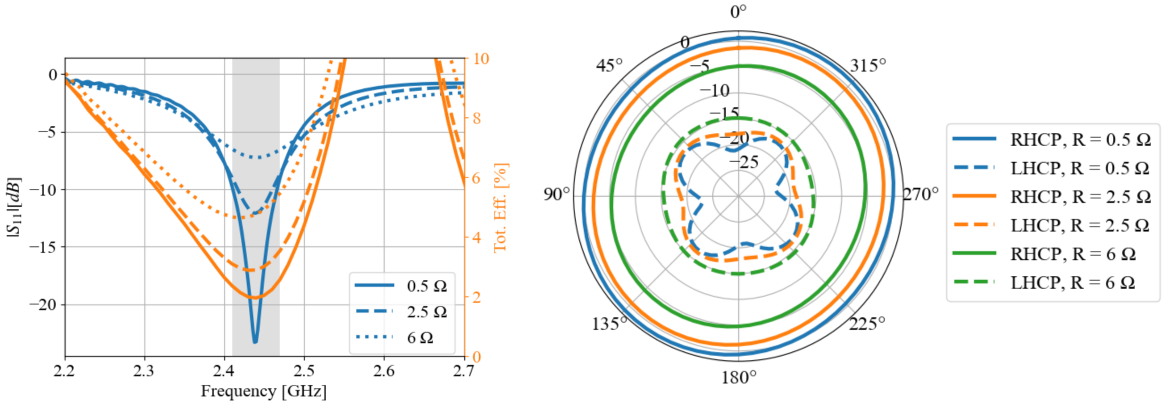

(a) **(b)**

Figure 2.3.8: Simulated results for increasing diode's equivalent circuit series resistance of reflection coefficient (a), and realized gain in azimuthal cut $\Theta = 90^\circ$ at 2.44 GHz (b) of the antenna in RHCP reconfiguration state

The limits of the proper functioning behavior of the proposed antenna are strongly dependent on the RF characteristics of the PIN-diode. For this reason, more accurate considerations can be made based on this observation, as illustrated in Figure 2.3.7 from the SMP1345 datasheet [33], which demonstrates that the forward bias current is inversely proportional to the equivalent series resistance of the diode.

Simulations have been conducted considering different equivalent series resistances for the diodes, and results in terms of S_{11} and AR are reported in Figure 2.3.8 (a). As the resistance increases, matching is lost, reducing the magnitude of the S-parameter. At the same time, AR increases, falling outside the 3 dB threshold.

The limited amount of DC current in the AL arms negatively affects the AC current flowing in the loop. Consequently, impedance matching is lost, along with the balance between vertical E_θ and horizontal E_ϕ far-field components. As the CP loses magnitude, RHCP and LHCP become closer for increasing equivalent series resistance in the diode model, as shown in Figure 2.3.8 (b).

2.4 Conclusions

In this chapter, an overview of OCP antennas available in the literature has been introduced, with a focus on CP composition through combination of two omnidirectional radiating structures.

A compact OCP antenna suitable for IoT devices was presented in Section 2.2. The design, which combines AL and WP structures to develop RHCP in the 2.44 GHz ISM band, and its optimization is addressed. The fabricated and tested prototype of the antenna shows results in good agreement with the simulations, confirming the effectiveness of the proposed solution in terms of both electrical and radiation characteristics. Despite exceeding the 3 dB AR across the azimuth plane, the 4.1 dB of elliptic polarization grants an isolation between RHCP and LHCP of at least 10 dB. Measured -10 dB impedance matching bandwidth is 120 MHz wide (4.9%) from 2.40 to 2.52 GHz. The measured RHCP maximum realized gain and total efficiency are 1.91 dBic and 87%, respectively, making this antenna suitable for CP-based communications despite its elliptical polarization.

Based on this structure, a RHCP to LHCP reconfigurable OCP antenna has been studied in section 2.3. The reconfiguration, based on 8 PIN-diodes, relatively low-power demanding, and its size of just $0.25 \times 0.25 \times 0.08\,\lambda^3$ makes this antenna perfectly suitable for IoT applications. Measurements on a prototype of this antenna highlighted the importance of addressing challenges related to the integration of discrete Surface Mounted Technology (SMT) components during the antenna design and optimization process, and emphasizes the critical role of the forward DC biasing current in the PIN-diodes for their AC applications.

Looking forward, the inclusion of more complex structures already in simulation, which take into account the specific behavior of discrete SMT components, is expected. Alternatively, the use of lower insertion-loss alternatives like RF-MEMS on the same antenna structure could be considered.

The design of antennas for IoT, however, presents distinctive challenges. Miniature antennas with differential feeds, for example, need special handling. Integrating RF modules transceivers, or even a reconfiguration circuit necessitates a careful, coordinated design with the antenna to prevent additional control lines from disrupting the optimized design.

References

[1] C. A. Balanis, *Antenna Theory: analysis and design*. Hoboken, New Jersey: John Wiley, 4 ed., 2016.

[2] D. Pozar, *Microwave Engineering*. Wiley, 2012.

[3] G. Zheng and B. Sun, “High-gain normal-mode omnidirectional circularly polarized antenna,” *IEEE Antennas and Wireless Propagation Letters*, vol. 17, no. 6, pp. 1104–1108, 2018.

[4] X. Quan, R. Li, and M. M. Tentzeris, “A broadband omnidirectional circularly polarized antenna,” *IEEE Transactions on Antennas and Propagation*, vol. 61, pp. 2363–2370, 2013.

[5] W. Lin and R. W. Ziolkowski, “Compact, high directivity, omnidirectional circularly polarized antenna array,” *IEEE Transactions on Antennas and Propagation*, vol. 67, no. 7, pp. 4537–4547, 2019.

[6] J. Shi, X. Wu, X. Qing, and Z. N. Chen, “An omnidirectional circularly polarized antenna array,” *IEEE Transactions on Antennas and Propagation*, vol. 64, no. 2, pp. 574–581, 2016.

[7] J. Wu and K. Sarabandi, “Compact omnidirectional circularly polarized antenna,” *IEEE Transactions on Antennas and Propagation*, vol. 65, no. 4, pp. 1550–1557, 2017.

[8] J. Liu, Y. Li, Z. Liang, and Y. Long, “A planar quasi-magnetic–electric circularly polarized antenna,” *IEEE Transactions on Antennas and Propagation*, vol. 64, no. 6, pp. 2108–2114, 2016.

[9] N. Yang, K. W. Leung, K. Lu, and N. Wu, “Omnidirectional circularly polarized dielectric resonator antenna with logarithmic spiral slots in the ground,” *IEEE Transactions on Antennas and Propagation*, vol. 65, no. 2, pp. 839–844, 2017.

[10] W. W. Li and K. W. Leung, “Omnidirectional circularly polarized dielectric resonator antenna with top-loaded alford loop for pattern diversity design,” *IEEE Transactions on Antennas and Propagation*, vol. 61, no. 8, pp. 4246–4256, 2013.

[11] C. Guo, R. Yang, and W. Zhang, “Compact omnidirectional circularly polarized antenna loaded with complementary v-shaped slits,” *IEEE Antennas and Wireless Propagation Letters*, vol. 17, no. 9, pp. 1593–1597, 2018.

[12] Y. Shi and J. Liu, “Wideband and low-profile omnidirectional circularly polarized antenna with slits and shorting-vias,” *IEEE Antennas and Wireless Propagation Letters*, vol. 15, pp. 686–689, 2016.

[13] M. Akmal, A. Alieldin, and A. R. Eldamak, “A high-power sandwiched omnidirectional circularly polarized antenna for gnss systems,” *IEEE Access*, vol. 11, pp. 31167–31176, 2023.

[14] D. Yu, S.-X. Gong, Y.-T. Wan, and W.-F. Chen, “Omnidirectional dual-band dual circularly polarized microstrip antenna using tm_{01} and tm_{02} modes,” *IEEE Antennas and Wireless Propagation Letters*, vol. 13, pp. 1104–1107, 2014.

[15] D. Yu, S.-X. Gong, Y.-T. Wan, Y.-L. Yao, Y.-X. Xu, and F.-W. Wang, “Wideband omnidirectional circularly polarized patch antenna based on vortex slots and shorting vias,” *IEEE Transactions on Antennas and Propagation*, vol. 62, no. 8, pp. 3970–3977, 2014.

[16] Y. Ma, J. Li, and R. Xu, “Design of an omnidirectional circularly polarized antenna,” *IEEE Antennas and Wireless Propagation Letters*, vol. 16, pp. 226–229, 2017.

[17] Q.-X. Chu, M. Ye, and X.-R. Li, “A low-profile omnidirectional circularly polarized antenna using planar sector-shaped endfire elements,” *IEEE Transactions on Antennas and Propagation*, vol. 65, no. 5, pp. 2240–2247, 2017.

[18] X. Hu, S. Yan, J. Zhang, V. Volski, and G. A. E. Vandenbosch, “Omni-directional circularly polarized button antenna for 5 ghz wban applications,” *IEEE Transactions on Antennas and Propagation*, vol. 69, no. 8, pp. 5054–5059, 2021.

[19] Y. Yu, Z. Shen, and S. He, “Compact omnidirectional antenna of circular polarization,” *IEEE Antennas and Wireless Propagation Letters*, vol. 11, pp. 1466–1469, 2012.

[20] D. Wu, X. Chen, L. Yang, G. Fu, and X. Shi, “Compact and low-profile omnidirectional circularly polarized antenna with four coupling arcs for uav applications,” *IEEE Antennas and Wireless Propagation Letters*, vol. 16, pp. 2919–2922, 2017.

[21] L. Yang, N.-W. Liu, Z.-Y. Zhang, G. Fu, Q.-Q. Liu, and S. Zuo, “A novel single feed omnidirectional circularly polarized antenna with wide AR bandwidth,” *Progress In Electromagnetics Research C*, vol. 51, pp. 35–43, 2014.

[22] Y.-M. Cai, S. Gao, Y. Yin, W. Li, and Q. Luo, “Compact-size low-profile wideband circularly polarized omnidirectional patch antenna with reconfigurable polarizations,” *IEEE Transactions on Antennas and Propagation*, vol. 64, no. 5, pp. 2016–2021, 2016.

[23] B. Li and Q. Xue, “Polarization-reconfigurable omnidirectional antenna combining dipole and loop radiators,” *IEEE Antennas and Wireless Propagation Letters*, vol. 12, pp. 1102–1105, 2013.

[24] W. Lin and H. Wong, “Polarization reconfigurable wheel-shaped antenna with conical-beam radiation pattern,” *IEEE Transactions on Antennas and Propagation*, vol. 63, no. 2, pp. 491–499, 2015.

[25] D. Tang, X. Kong, and S. Liu, “Design of a low profile omnidirectional circular polarized reconfigurable antenna for beidou application,” in *2018 IEEE International Conference on Computational Electromagnetics (ICCEM)*, pp. 1–3, 2018.

[26] P. Liu, Q. Zhang, W. Zhang, D. Gao, and Q. Wang, “Omnidirectional circularly polarized reconfigurable antenna using endfire elements based on siw,” in *2023 17th European Conference on Antennas and Propagation (EuCAP)*, pp. 1–3, 2023.

[27] Y. Cui, C. Qi, and R. Li, “A low-profile broadband quad-polarization reconfigurable omnidirectional antenna,” *IEEE Transactions on Antennas and Propagation*, vol. 67, no. 6, pp. 4178–4183, 2019.

[28] W. Lin, R. W. Ziolkowski, and T. C. Baum, “28 ghz compact omnidirectional circularly polarized antenna for device-to-device communications in the future 5g systems,” *IEEE Transactions on Antennas and Propagation*, vol. 65, no. 12, pp. 6904–6914, 2017.

[29] A. Alford and A. G. Kandoian, “Ultrahigh-frequency loop antennas,” *Electrical Engineering*, vol. 59, no. 12, pp. 843–848, 1940.

[30] C. Delaveaud, P. Leveque, and B. Jecko, “New kind of microstrip antenna: the monopolar wire-patch antenna,” *Electronics Letters*, vol. 30, pp. 1–2(1), January 1994.

[31] V. Mastrosimini, L. Santamaria, M. Grande, F. Ferrero, R. Staraj, and L. Lizzi, “Miniaturized omnidirectional circularly polarized antenna for iot applications,” in *2021 15th European Conference on Antennas and Propagation (EuCAP)*, pp. 1–4, 2021.

[32] *Properties of Antennas*, ch. 1, pp. 1–41. John Wiley & Sons, Ltd, 2005.

[33] Skyworks, “SMP1345 Series very low capacitance plastic packaged silicon pin diodes,” 2023.

3 Pattern Reconfigurable

3.1 Introduction

Radiation pattern reconfiguration is a process by which an antenna dynamically changes the direction or shape of its radiated electromagnetic energy. This adaptation allows the antenna to optimize communications in heterogeneous environments.

In this context, pattern reconfigurable antennas are particularly suitable for IoT applications, where extended range coverage and energy efficiency are paramount. Specifically, for mobile end-nodes, these antennas can adapt to movement or changes in the surrounding environment, ensuring consistent communications. They can also enable dynamic beamforming to compensate for high speeds, such as in automotive applications.

The antenna can switch from a broad, omnidirectional pattern used for network discovery to a narrow, focused beam directed towards a specific receiver for long-range transmission. Unlike lenses and reflector antennas, which focus the beam in a specific direction and make reconfigurability a mechanical process, array antennas offer a solution for achieving beam-steering with smaller static structures. These structures control the direction of the lobes by adjusting the phase difference between elements [1].

With the recent increase in civil infrastructures applications driven by Unmanned Aerial Vehicle (UAV)s [2, 3] in IoT including smart agriculture, infrastructure inspection, remote sensing to goods delivery, pattern reconfigurable antennas are emerging as solution to provide the widest possible coverage, extending up to non-terrestrial communications [4].

Electronic steerable parasitic arrays radiators

It has been demonstrated that the directivity of an array antenna can be enhanced by reducing the spacing between elements [5]. However, this approach can lead to increased losses and consequently, a reduction in radiation efficiency. Furthermore, controlling the phase of an array may necessitate the use of bulky and lossy feeding circuits. As a result, sub-1GHz arrays designed for portability and miniaturization often employ parasitic element radiators to maintain the same reconfiguration principle while reducing size [6].

Firstly introduced by Harrington [7], who described the now more common ESPARs as “Reactively controlled directive arrays", these antennas feature a single fed radiating element surrounded by switchable reactive loaded parasitic elements. By controlling the reactive load, the electrical length of the parasitic element can be altered, thereby controlling its coupling with the active element and consequently, the resulting radiation pattern.

The challenge lies in controlling the reactive loads, which is achieved by implementing switching or tunable circuits that utilizes PIN-diodes, or RF switches or Varicaps.

Pattern reconfiguration can be achieved using PIN-diodes on a combination of three Huygens sources each consisting of a Capacitively Loaded Loop (CLL) and a magnetic Near Field Resonant Parasitic (NFRP). This configuration can achieve a gain of 3.55 dBi at 1.564 GHz, with 84.9% of radiation efficiency within a compact ESA volume of $0.29 \times 0.29 \times 0.05\ \lambda^3$ [8] [Figure 3.1.1 (d)]. A further reduction in size ($0.1 \times 0.1 \times 0.1\ \lambda^3$) and increase in peak realized gain to 6.6 dBi at 2.22 GHz is proposed in [9] [Figure 3.1.1 (e)]. In both cases coverage across 360° azimuthal plane is achieved, but with a relatively large beam of 120° and 158° respectively.

Another example of PIN-diodes-enabled beam-steering uses patch as source radiator and electronically shorted parasitic element to ground plane [10]. By selectively activating combinations of parasitic element, six directive beams can be developed, reaching peak gain of 10 dBi and 80.5% radiation efficiency. A bandwidth of 14.5% is obtained on the IEEE 802.11ac Local Area Network (LAN) bands. However, the overall structure size is considerable $1.75 \times 1.75 \times 0.5\ \lambda^3$, due to the need to include parasitic elements all around a radiating one, over the same ground plane.

In [11], a slot-based antenna capable of 12 directive pattern is proposed [Figure 3.1.1 (b)]. This antenna can reach a maximum realized gain of 4.29 dBi and ensures coverage across the entire azimuth plane with a minimum of 3.38 dBi before the subsequent beam. Despite the compact size ($0.29\lambda \times 0.29\lambda \times 0.38\lambda$) and the simplicity of using PIN-diodes, the number of diodes (12) increases the complexity at the control circuit level.

As an alternative to PIN-diodes, the use of Single Pole Multiple Through (SPnT) switches can be implemented to simplify the control mechanism structure and reduce the use of discrete components [12] [Figure 3.1.1 (f)]. A cloverleaf-like antenna structure realizes a 4-direction ESPAR with self-matched parasites, developing a peak gain beam of 3.9 dBi at 2.44 GHz and front-to-back ratio of 6.5 dB. The impedance bandwidth covers the entire ISM 2.4 GHz bandwidth with a total efficiency of around 60%.

Optimization Procedures for ESPAR Loads Disposition and Values

Designing multiple radiating elements that must couple with each other and dynamically change radiation properties while maintaining steady impedance, poses a substantial challenge. This challenge is particularly evident in the design of the reactive load switching/dimming and the consequent DC and RF isolated feeding circuit.

The complex requirements of such radiating systems make it difficult to rely solely on analytic design methods. However, if the requirements are well-defined, one potential solution is to apply optimization algorithms to find the best possible solution. Once the design variables are defined, an objective function is formulated to quantify a certain antenna performance. Then, constraints are placed, and finally, the optimization procedure is run. The most widely used optimization algorithms are the Genetic Algorithm (GA) and Swarm Intelligence (SI). However, according to the "No Free Lunch Theorem" [13], no optimization algorithm can uniformly outperform all others across all types of optimization problems on average.

In [14], three emerging SI algorithms are compared for the geometrical optimization of a dual-band aperture-coupled patch antenna: the Gray Wolf Optimizer (GWO), the Whale Optimization Algorithm (WOA), and the PSO. The GWO outperformed the others in this specific design problem. There have been many contributions to the description of the coupling and impedance matching problem on ESPARs, with the objective being super-directive and super-realized gain antennas. By limiting the reactive load to a Varicap, it is possible to analytically describe the current on parasitic elements and thus its radiation response, knowing the mutual impedance [15, 16]. Similarly, an iterative optimization algorithm can be used to find the optimal array element reactive loads that contribute to achieving the desired radiation characteristics [17]. A PSO is used in [18] for the optimization of super-directive antennas' geometrical design parameters such as inter-element distance, dipole widths, and lengths. This demonstrates how SI can simplify the design and implementation of complex, compact, high radiation efficiency antenna systems.

Pattern reconfigurable antennas for unmanned aerial vehicles

In Drone to Ground (D2G) communications, antennas equipped on UAVs are preferred to have conical beams pointed towards the ground. In [19], a conical beam is achieved through the combination of four directive beams. The structure is based on a combination of monopole and patch structures, with reconfiguration achieved through control of their feeding network.

A combination of a monopole and orthogonal radial dipoles is proposed in [20], where PIN diodes are used to control the coupling between the dipoles and the monopole, greatly simplifying the structure design. Broadside beams are combined in multiple planes to achieve up to 75° steering by activating coplanar parasitic patches through PIN diodes. In [21], it is also demonstrated that ESPARs can inherit CP with coherent sources, and DRA can be used to enhance the impedance bandwidth [Figure 3.1.1 (a)].

Based on this same principle, a set of 3×3 coplanar ESPAR patches working at 6 GHz can enable conical beam scanning, reaching 8.2 dBi of peak gain and reconfigurability across three axes through PIN-diodes activated parasitic elements [22] have been presented. Despite the relevant volume of the overall structure compared to the wavelength λ_g: $1 \times 1.4 \times 0.04\ \lambda^3$ its efficiency remains relatively low, around 38%.

Transitioning from antenna designs, the implementation of these as electronically controlled communication systems is crucial. An example is proposed in [23], where an 8 parasitic element ESPAR with as many switchable directive beams is used for Direction of Arrival (DoA) estimation in WSN [Figure 3.1.1 (c)]. The $1.3\lambda \times 1.3\lambda$ antenna system has been designed to work at 2.4 GHz with selective activation of sets of parasitic elements through PIN diodes. It uses Received Signal Strength Indicator (RSSI) of Binary Phase Shift Keying (BPSK) test signals to estimate the DoA in a controlled environment.

However, in real-world deployments, communication performance is constrained by various other factors such as the transmission protocol, the surrounding environment, and the integration with the supporting structure. Along with simulations and measurements in controlled environments, tests at higher levels in practical on-field deployment are needed to validate the efficiency of the communication [24].

In the context of D2G communications, a recent example of a WSN node with DoA capabilities is proposed in [25], with a focus on real-life outdoor environment measurements. The ESPAR structure consists of a central active monopolar radiating element and 12 surrounding parasitic elements, controlled by Single Pole Double Through (SPDT) switches for beam switching. After a detailed description of the component integration, such as the RF transceiver, STM32 microcontroller, power supply, and switching circuits, the DoA capabilities are demonstrated, confirming the advantages of integrating simple ESPARs in WSN nodes.

Flexible, conformal arrays

In recent years, conformal structures have been increasingly used in array antennas, particularly in the X-band [26], where applications for space, defense, and military fields are dominant. Alongside the most common wearable applications [27], conformal and more generally flexible antennas are suitable for UAVs and aerospace applications due to their ability to adapt to the vehicle profile without affecting its aerodynamics [28]. However, these antennas are designed to conform to a specific rigid surface.

Shape-changing antennas include the deployable antennas structure, perfect candidate for space applications where the antenna occupies a smaller volume during the launch phase. These shapes can use flexible modular structure [29], accordion-like folding [30] or more complex origami structures [31]. Furthermore shape-changing systems can be used to mechanical beam-form the radiation pattern of a radiating structure. Although, due to the reduction of the cross-sectional area of the array when it is folded or conformed to a curved surface the maximum gain of a folded array is always smaller compared to its planar form of a inverse squared proportionality to the curvature radius [32]. Moreover, whenever an array is designed, its shape is strictly responsible for mutual coupling between elements, thus since any change in the shape would affect the mutual coupling, a re-focus is needed to maximize the power transmission [33, 34] [Figure 3.1.1 (g)]. Following the same principle in [35], these variations are used instead to reconstruct the array shape and estimate its bending angle.

One of the challenges for flexible array resides in the array feeding control. In order to be fully flexible, phased arrays are required to integrate the electronic circuitry used to control the radiators on the same flexible surface of the radiating element [36]. E.g. in [37] [Figure 3.1.1 (h)], the authors demonstrate the first fully-contained origami-inspired phased array operating at 28 GHz with on-structure integrated beamformer ICs and a face-to-face feeding network connecting all four faces of the utilized “eggbox” origami structure.

In this chapter

The chapter continues as follows: in section 3.2 a 7 elements ESPAR design process is presented, starting with the design of the single radiating element, continuing with its combination in a symmetric lattice, its parasitic elements reactive loads optimization based on PSO, finishing with the control circuit integration design.

Following, in section 3.3 the design of a 5 elements ESPAR designed for long range LoRa UAV-enabled applications is presented, with RSSI-based pattern reconfigurable performance assessment on a real case scenario.

Finally, in section 3.4 a study on additively manufactured flexible phased array is presented to assess the capabilities of portable shape-changing pattern reconfigurable arrays.

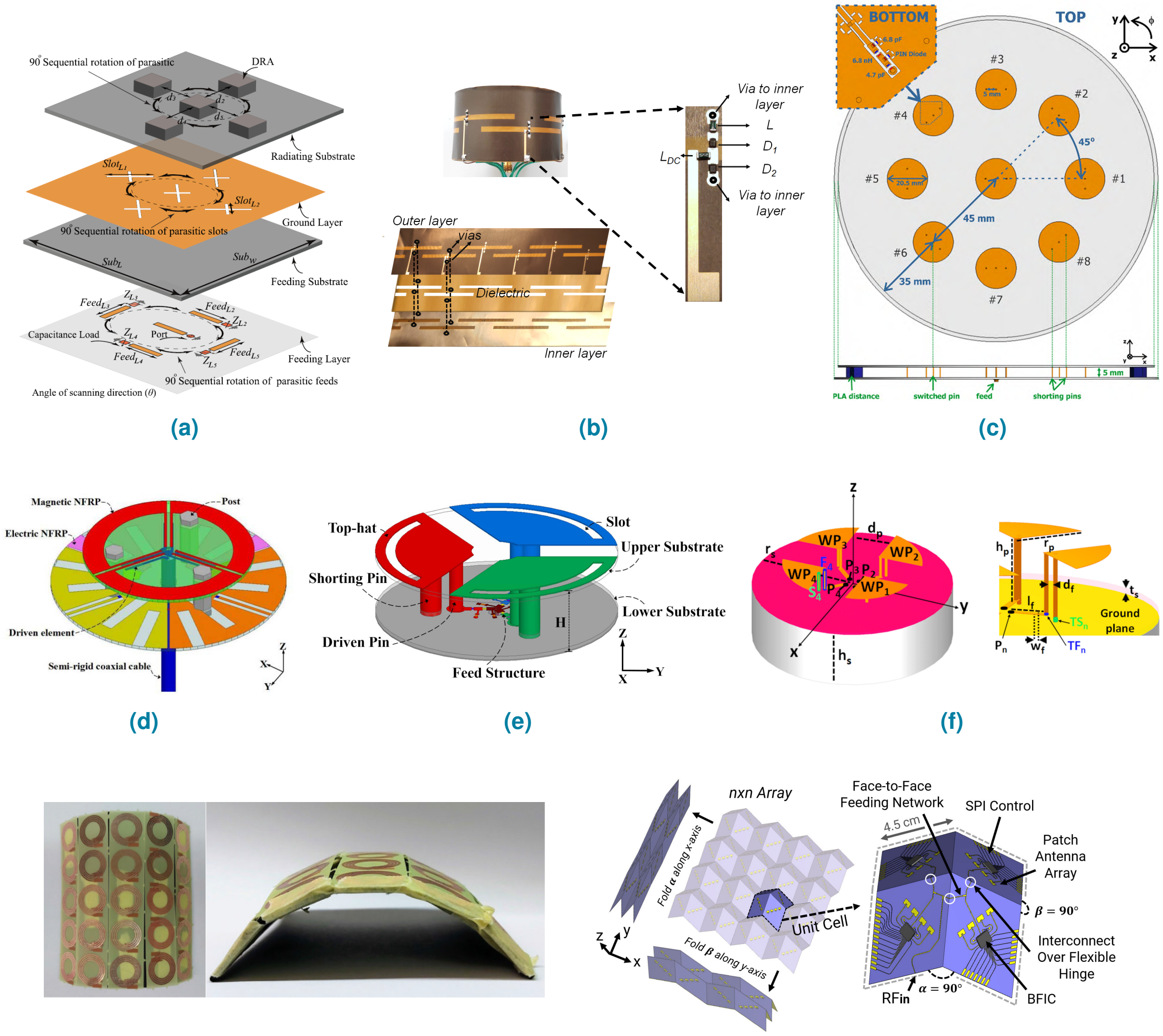

(a) (b) (c)

(d) (e) (f)

(g) (h)

Figure 3.1.1: Examples of pattern reconfigurable antennas: (a) a CP electronically steerable ESPAR of DRAs for conical beams [21] , (b) a slot-based ESPAR cylinder shaped for a 360° coverage across the azimuth [11], (c) a low profile 9-elements ESPAR for RSS-based DoA estimation applications [23], (d) a low-profile ESA with PIN diodes-enabled pattern reconfigurability [8], (e) a compact near-field resonant parasitic antenna with PIN diodes-based beam switching [9] and a 4 element version (f) with Single Pole Four Through (SP4T) switch control [12], (g) arbitrarily conformal metasurfaces for wireless power transfer systems for mechanical pattern reconfiguration [34], and (h) an origami-inspired shape-changing phased array which combines phase and mechanical pattern reconfiguration [37].

3.2 Low Profile Pattern Reconfigurable ESPAR

The design of an ESPAR structure, comprised of one central driven element and 6 surrounding identical parasitic elements, based on WP radiators is presented.

The concept's effectiveness is proven by comparing two ESPARs at different frequencies in simulations, and further validated with measurement on a prototype. The structure's small size ($\lambda \times \lambda \times 0.1\lambda$), high directive gain, and lightweight construction make it well-suited for long range M2M communications on UAVs. In this work a PSO-based methodology (see Appendix A) to find reactive loads for the parasitic elements is employed. This section ends with considerations on a practical manufacturing approach, taking into account the challenges associated with the integration of the reconfiguration circuit.

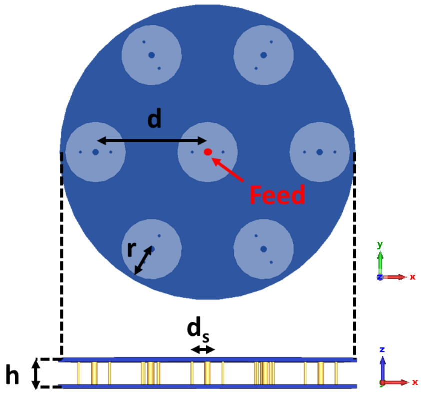

Figure 3.2.1: Geometry and fundamental parameters of the proposed antenna.

3.2.1 Antenna Structure Design and Optimization

The proposed ESPAR consists of seven equal elements in a circular array, single-fed at the center, as presented in Figure 3.2.1. Initially, the single element is designed as a circular WP radiator due to its miniaturization and omnidirectional properties.

The design includes a central feed that connects two equal circular patches of radius $r = 0.1\lambda$ separated by a distance of $h = 0.1\lambda$. These shorted by 2 vias, each at $d_S = 0.05\lambda$ from the central feed, to facilitate the impedance matching.

As demonstrated in Section 2, the h and r parameters inversely affect the resonance frequency, as they influence the electrical length of the radiating element. The feed-to-via distance d_V was set during the design phase to tune the impedance matching, given it affects the capacitive coupling between the two patches. For the design of each individual radiating element, it's crucial to ensure that the condition of impedance matching is met at the required frequency. This condition is considered fulfilled when the reflection coefficient $|S_{11}|$ reaches its minimum value

Once the single element is designed, it is replicated six time on a surrounding circle, composing the parasitic elements array. The center-to-center distance of $d = 0.27\lambda$ have been chosen arbitrarily. Regardless of the inter-element distance, the PSO algorithm can find a set of optimized reactive loads that maximize the realized gain in a desired direction.

Static single beam configuration

The effectiveness of the proposed design methodology has been assessed numerically at two frequencies for a static, single beam configuration. The PSO procedure is used to find the six reactive load to apply to each of the parasitic elements to maximize the beam in the desired direction. These loads are then rounded, to better approximate real-world scenarios. Since the PSO objective is to maximize the realized gain starting from coupling coefficients and far-fields, this study does not consider the impedance matching of the entire structure, focusing instead solely on far-field realized gain.

At 5.075 GHz the PSO-based procedure is applied to find the four loads [Table 3.2.1 (a)] that enable the ESPAR to generate the maximum realized gain of 7.61 dBi, in a specified direction, as illustrated by Figure 3.2.2 (a). As the reconfigurable beam can point in six directions with maximum realized gain every 60°, this overlap guarantees a 360° coverage on the azimuth plane. The overlap between consecutive switched beams ensures a realized gain always greater than 5 dBi, given that the Half-Power Beam Width (HPBW) is greater than 70.8°. Additionally the Front-to-Back Ratio (FBR) is 9 dBi.

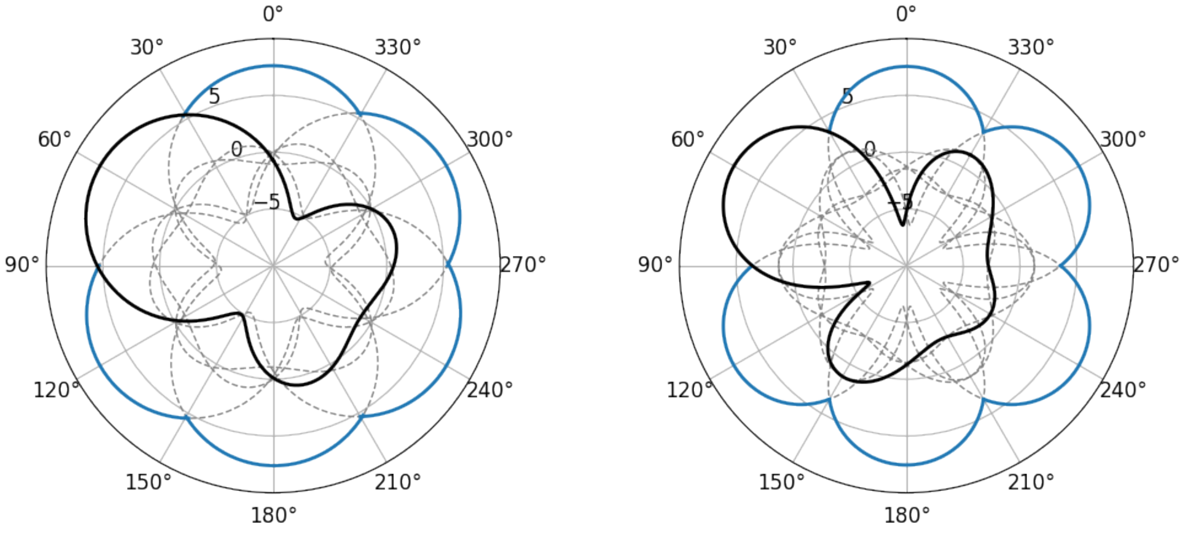

(a)

(b)

Figure 3.2.2: Overlap of the directive beams realized gain in the azimuth plane to prove the 360° beam-steering coverage in case of optimized structure for (a) 5.075 GHz (b) and 2.4 GHz

Table 3.2.1: Set of optimized reactive loads for a maximum gain pointing to Parasite #1 for (a) 5.075 GHz, and (b) 2.4 GHz version.

(a)

Parasite #	1	2	3	4	5	6
C [pF]	/	/	0.3	0.5	0.3	/
L [nH]	1	1.8	/	/	/	1.8

(b)

Parasite #	1	2	3	4	5	6
C [pF]	/	3.7	/	/	/	3.7
L [nH]	1	/	10	4	10	/

On the other hand, Figure 3.2.2 (b) shows that the 2.4 GHz version's optimization achieved a 7.55 dBi realized gain. While the FBR remains the same, the shape of the realized gain radiation pattern in this case presents two side-lobes with a Side Lobe Level (SLL) of -6.3 dB. The HPBW is reduced to 52.7°, leading to a decrease in the overlapping realized gain of consecutive beams, although it remains greater than 3.5 dBi.

3.2.2 Measured Results

Both 5.075 GHz and 2.4 GHz simulated models have been optimized using four reactive loads to maximize the realized gain of the ESPAR structure, following the same design procedure. A prototype of the antenna operating at 5.075 GHz has been realized and tested in an anechoich chamber [Figure 3.2.3 (a)] to validate the efficiency of the methodology. The optimal loads were soldered on the corresponding parasitic element based to Table 3.2.1 (a), between the bottom layer patch and the central via. Due to the the antenna's small size, a sleeve balun rigid coaxial line was used during the prototype's measurements, as shown in Figure 3.2.3 (b).

(a) **(b)**

Figure 3.2.3: Antenna prototype during measurement in anechoic chamber.

The measured S_{11} parameter shows a 4.6% shift to lower frequencies, along with a decrese in efficiency, which can be attributed to the presence of the balun and manifacture imperfections. The -10 dB bandwidth is 132 MHz wide, and the maximum measured realized efficiency is 73.8% at 4.84 GHz.

Given the narrow total efficiency bandwidth centered at 4.84 GHz, the measured radiation results refer to this frequency rather then the 5.075 GHz design frequency.

The comparison with the measured realized gain curve in Figure 3.2.5 shows that the pattern shape is consistent with the simulated results, albeit with a higher SLL of -3.37 dB instead of -4.7 dB. The maximum measured realized gain is 6.64 dBi in the desired direction.

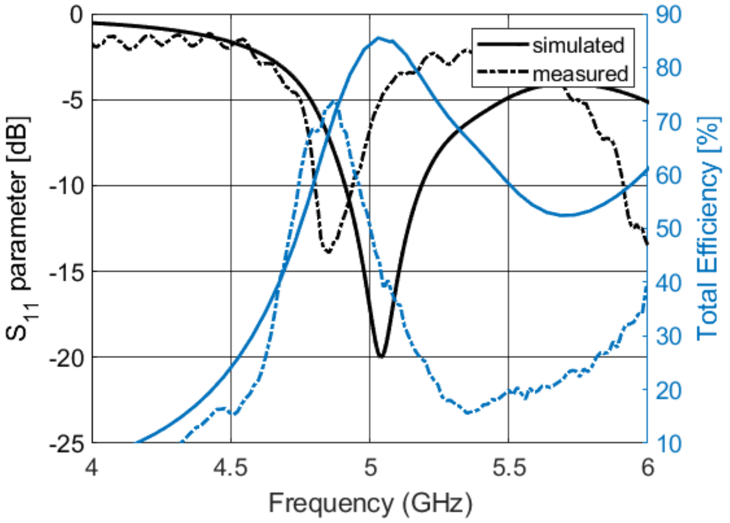

Figure 3.2.4: Antenna S_{11} parameter and total efficiency measurement comparison with simulation.

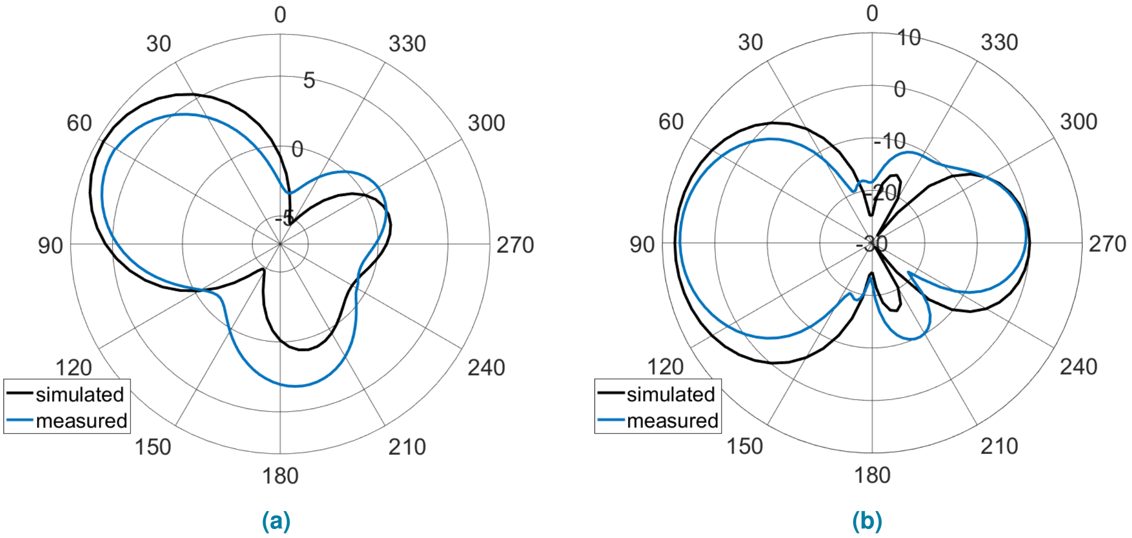

(a)

(b)

Figure 3.2.5: Antenna realized gain (a) azimuth and (b) elevation plane cut: simulated and measured results comparison.

3.2.3 The Re-Optimization Problem

In previous sections, the geometry design of the ESPAR structure, its optimization based on PSO maximizing the realized gain, and the characterization in a static configuration have been presented.

As previously shown, due to the structure symmetry, four loads are needed to achieve a high-gain beam, while beam-steering is obtained by rotating the load combinations on the array parasitic elements as a whole. Therefore, a switching circuit on each parasitic element is necessary to provide the expected reconfigurable beam-switching. In this context, a model that takes into account the presence of an SP4T switch placed on the bottom patch of each parasitic element has been considered in simulations to ensure reliability in practical applications.

This issue is addressed in this section, considering the structure designed to work at 2.4 GHz. This choice was made to minimize the effects of the reconfiguration circuit, due to the ratio between the SP4T size and the radiating surface of the lower patch disk of the parasitic elements being smaller than the one at 5.075 GHz.

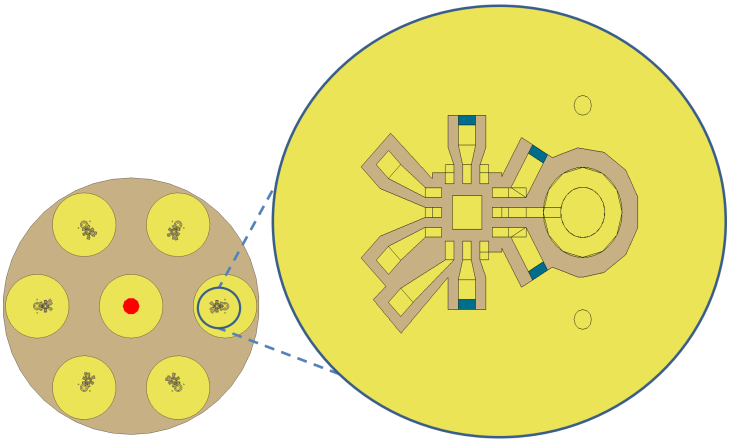

Figure 3.2.6: Overview of the antenna structure with a zoom on the SP4T switch footprint.

The footprint of the SP4T, the four loads, and voltage biasing pins have been included in the design of the bottom parasitic elements' circular patch. Simulations that takes into account the components' presence have been carried out considering the SP4T equivalent circuit provided by the manufacturer Psemi for the PE613050 UltraCMOS® switch shown in Figure 3.2.7, as 1.6 Ω for the activated RF output and 0.14 pF for the others which are off.

The inclusion in simulations of the RF responses of the discrete components and the difference in the electrical path induced by the switch introduces changes in the shaping of the overall structure beam, as presented in Figure 3.2.8 (a). Up to 5 dB of maximum realized gain beam are lost and the beam is spread, meaning that the results of the optimization on the previous ideal ESPAR deteriorate significantly when considering a structure which takes into account practical manufacturing challenges. Thus, another PSO-based optimization procedure is performed on the structure complete with reconfiguration circuit footprint including the SP4T equivalent circuit in the simulation. The result, presented in Figure 3.2.8 (b), is again a directive beam which reaches 7.34 dBi of maximum gain, with just 0.21 dB of losses compared to the ideal version, and reduced side-lobes and FBR.

Due to its discrete selection of loads, the SP4T introduces asymmetries, which the optimization

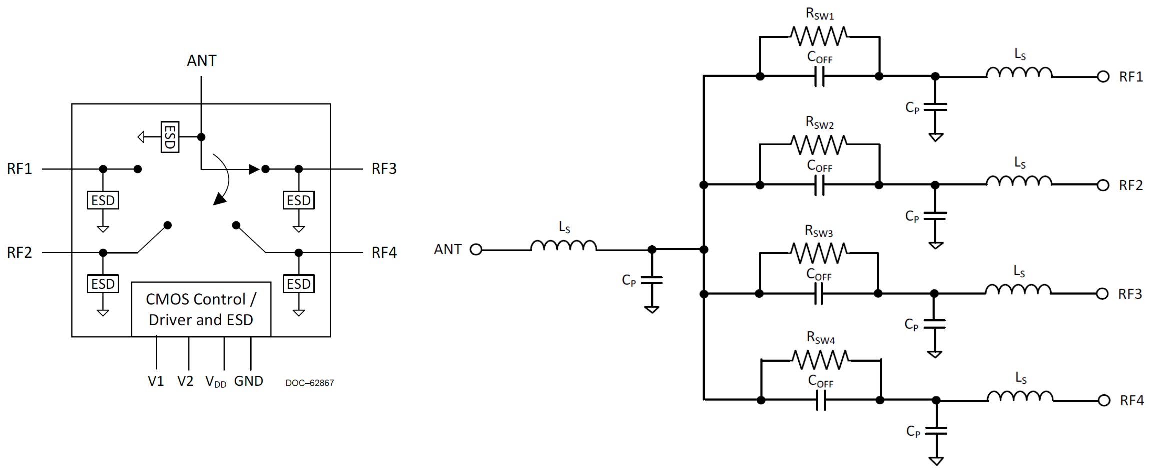

(a) **(b)**

Figure 3.2.7: Psemi PE613050 (a) Functional diagram and (b) Equivalent Circuit model schematic

Table 3.2.2: Set of re-optimized reactive loads rounded to discrete available SMT values

Parasite #	1	2	3	4	5	6
C [pF]	/	0.3	/	1.3	/	0.3
L [nH]	1	/	10	/	10	/

procedure compensated finding five loads instead of four to maximize the beam realized gain. A further approximation to make the switching symmetric again, using discrete values provided by components manufacturers, results in a set of loads as in Table 3.2.2.

The final result is a slightly deformed pattern of 6 dBi maximum realized gain, tilted by 27°. The loss of 1.55 dBi maximum gain compared to the ideal case demonstrates the importance of validating simple structures through closer-to-real simulations when considering a reconfigurable antenna ready to manifacture.

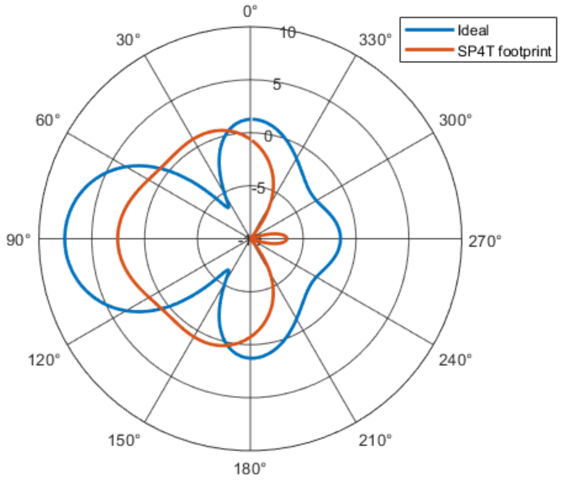

(a) **(b)**

Figure 3.2.8: Antenna realized gain comparison to ideal case when (a) reactive loads optimized for an ideal case are included in the footprint of the reconfigurable one, and (b) reactive loads optimized on the reconfigurable structure with SP4T switch footprint.

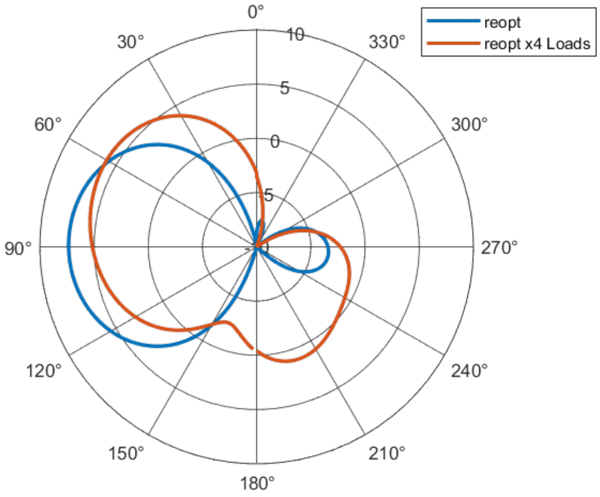

Figure 3.2.9: Antenna realized gain including rounded reactive loads to available SMT discrete components.

3.3 Design and On-Field Test of ESPAR Antenna for UAV-based Long-Range IoT Applications

In the following section a 4 directive and an omnidirectional pattern switchable beams ESPAR structure based on simple PIN-diodes design is presented. The integration of a reconfigurable control circuit on the antenna structure and an on-field test of LoRaPHI [38] 868 MHz packet transmission are performed to assess the performance in real-life long range UAV-based IoT applications.

3.3.1 Design of the Parasitic Element Antenna System

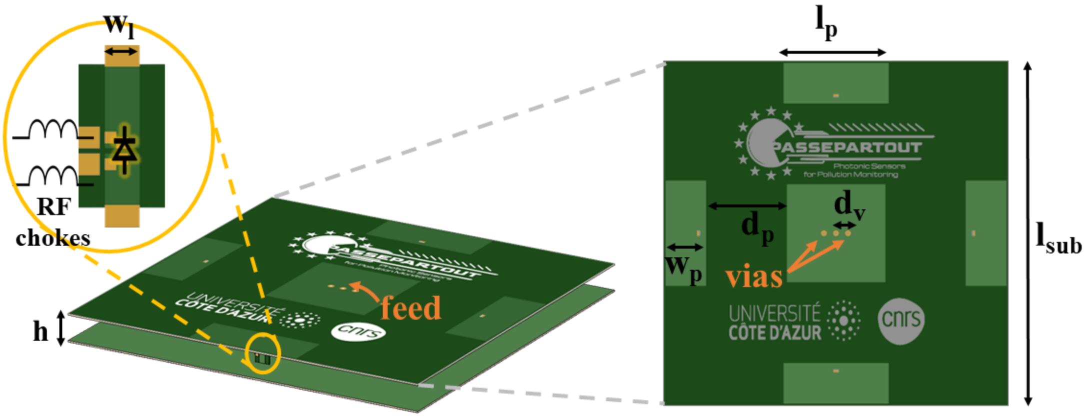

Figure 3.3.1: Antenna structure with a zoom on parasite's snap-fit PCB with PIN diode and RF chokes.

The antenna structure, presented in Figure 3.3.1, consists of a single-fed squared shorted patch surrounded by 4 rectangular patches. The central active radiating element represents the well-known WP radiator, which can develop an omnidirectional radiation pattern despite the small vertical extension. This is achieved by placing two shorting wires parallel to the SMA core connector at a distance d_v. These wires, positioned between the two PCBs, act as an equivalent parallel inductance to the capacitance created by the patch and the ground plane. The five patches are printed on a 0.8 mm thick 20×20 cm^2 wide FR-4 substrate, while another PCB of the same size is placed at a distance h and acts as ground plane. Four snap-fit PCBs that host an SMP1345 PIN-diode connect the passive patches to the ground plane.

RF-chokes are needed at the ends of the PIN-diodes on the vertical snap-fit PCBs in order to insulate the microcontroller used to activate the diodes from the RF signals. For this purpose, a 100 nH inductor providing a reactance of $jX_L = j\omega L \simeq j545\ \Omega$ at 868 MHz was used. One advantage of having the snap-fit PCB between the layers is the easy and accurate manufacturing of the entire structure, fixing the air gap to the snap-fit notch length of 13.37 mm.

The resulting system enables 5 pattern configurations: one omnidirectional configuration when all the diodes are OFF, and 4 directive patterns when the diodes are activated one by one. These latter patterns point in the directions opposite to the correspondent activated parasitic element. The 4 directive beams can combine in a conical shape meeting the requirement for UAVs antennas.

Table 3.3.1: Optimized antenna geometrical parameter values

param. name	l_{sub}	h	l_p	w_p	d_v
value [mm]	200	15	61	23.5	7

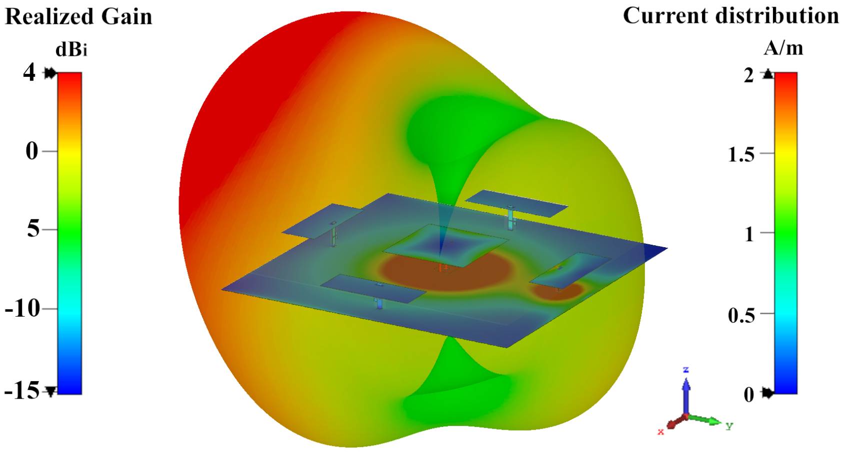

Figure 3.3.2: Contour current distribution and Realized Gain far-field distribution for a diode activated parasitic element.

Design procedure

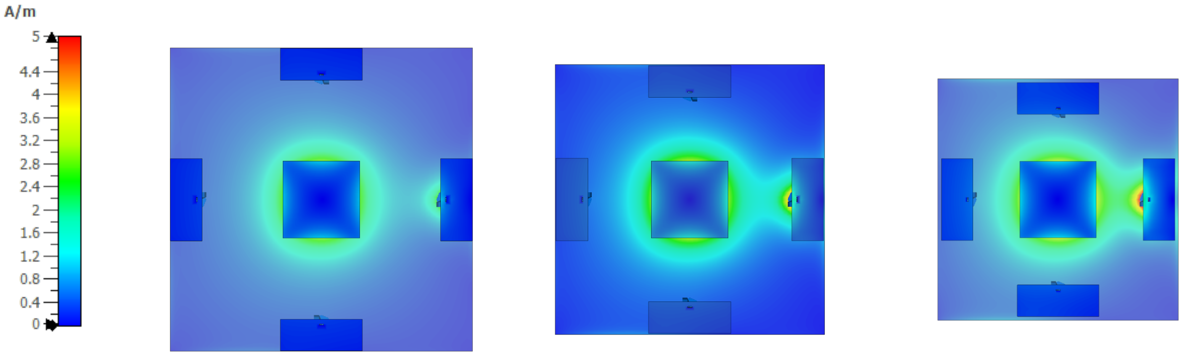

(a) (b) (c)

Figure 3.3.3: Comparison with coupling surface current in case of (a) 60 mm, (b) 47 mm and (c) 35 mm distance between radiating and parasitic elements.

The design process is described in the three following simple steps:

1. A simple squared WP antenna has been designed to work at 868 MHz. The size l_p of the patch acting as a top-hat for the SMA core of length h has been optimized together with the distance between the vertical pins and the central feed over a fixed ground plane of 200 × 200 mm. The optimization has been aimed at maximizing the antenna impedance matching at 868 MHz.
2. the parasitic elements have been designed starting from top-hat monopoles. Rectangular patch shapes have been chosen to better couple with the squared active patch at a fixed distance of 0.2λ.

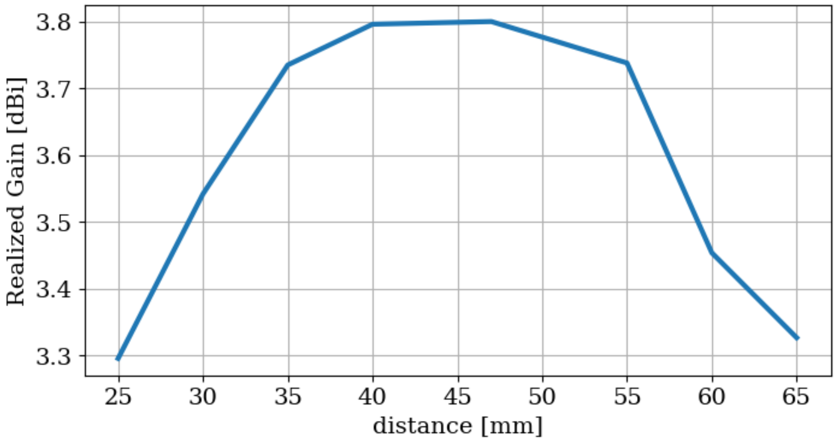

Figure 3.3.4: Realized Gain variation compared to parasite distance between radiating and parasitic elements.

A simple wire has been considered as short circuit between the parasitic patch and the ground plane, its position has been chosen to be on the patch's closest edge to the central element to maximize the coupling. In an advanced model, the snap-fit PCBs have been considered instead of the wire model for the shorting vias in order to house the diode footprint. Activating one diode at a time, the corespondent parasitic patch element is thus shorted to the ground plane and acts as a reflector in the radiation pattern composition. This phenomenon is shown in Figure 3.3.2. It is evident that the current distribution indicates that when the right parasitic element is engaged through the diode's activation, it interacts with the central patch, assuming a radiating role. The concurrent radiation from both elements, along with the influence of the ground plane, directs the beam in the opposite direction.

3. Finally, an optimization of the distance between central and parasitic elements have been carried out to maximize the antenna realized gain in the directive configuration. The coupling in terms of surface current for three different distances is shown in Figure 3.3.3. The reflective effect of the activated parasitic element is due to the current on the snap-fit PCB which comes to be opposite to the one on feed and vias. Moreover, even if in Figure 3.3.3 (c) the coupling between the central patch and the activated right parasitic element is stronger, it can be noticed that a higher amount of current spreads on the ground plane, either unwantedly participating to the coupling of other parasitic elements, either increasing losses [Figure 3.3.3 (a)]. For the case in Figure 3.3.3 (b), instead, the current is focused between the fed element and the shorted parasitic element. No interaction with the other parasitic elements nor leaks on the ground plane occur, resulting in a greater realized gain. As a further confirmation, the variation of gain with respect to the parasitic element distance is presented in Figure 3.3.4 and it shows that the optimal relative placement can be found around 0.13λ (44 mm).

The optimized final design refers to the parameters reported in Table 3.3.1.

3.3.2 Numerical and Experimental Results

Simulations of the optimized antenna structure have been carried out using CST Microwave Studio Electromagnetic simulator. The PIN-diodes have been modeled according to the component datasheet as lumped elements, considering 100 mA and 2.1 V for forward-biased diodes, and 0V for reverse-biased diodes. The 100 nH RF-chokes have been also modeled as lumped elements.

A prototype of the proposed antenna system has been manufactured, measured, and the results are compared with simulations. The prototype has been equipped with an SMA connector to be measured with a Rohde & Schwarz Vector Network Analizer and in a SATIMO StarLab system. As show in Figure 3.3.5, the measured Voltage Standing Wave Ratio (VSWR) and total efficiency values are in good agreement with simulations. The measured total efficiency at 870 MHz amount to 87.9%, and the measured VSWR is 32 MHz wide (for VSWR $\leq$ 2) ranges from 843 to 875 MHz. The difference with the simulated results stand in a small 1% frequency shift. Simulations show a resonance which is perfectly centered in 868 MHz ranging from 855 to 881 MHz and a relatively smaller total efficiency. In both cases, the coverage of the LoRa European frequency bands (863-870 MHz) is guaranteed.

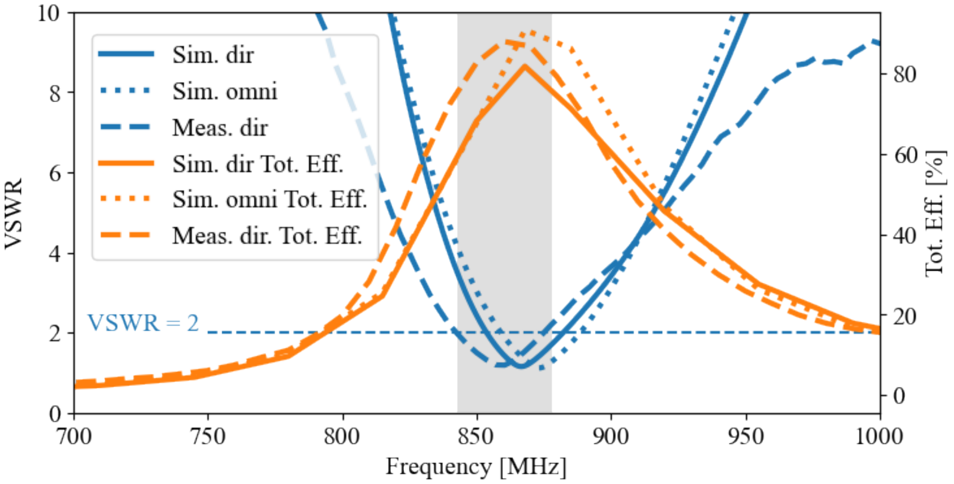

Figure 3.3.5: Simulated and measured VSWR and total efficiency when a directive beam is activated and in omnidirectional case.

The measured realized gain cut along the direction of the maximum in the directive case is presented in Figure 3.3.6 (a) in comparison with the simulated one. A good agreement is visible with a measured and simulated maximum gain of 3.95 dBi. Differences stand only for low values of the gain and they can be addressed in part to the SMA cable and support of the measurement system. A demonstration of the conical coverage is presented in Figure 3.3.6 (b) where an overlay of the 4 switchable directive gain beams is proposed. The intersection between consecutive configuration states is always greater than 3 dBi. Moreover, the difference between configurations in opposite directions is always greater than 4 dBi. The resulting 360° coverage indicates that activating more than 1 diode at the time is unnecessary as a larger beam with a smaller maximum gain would be produced.

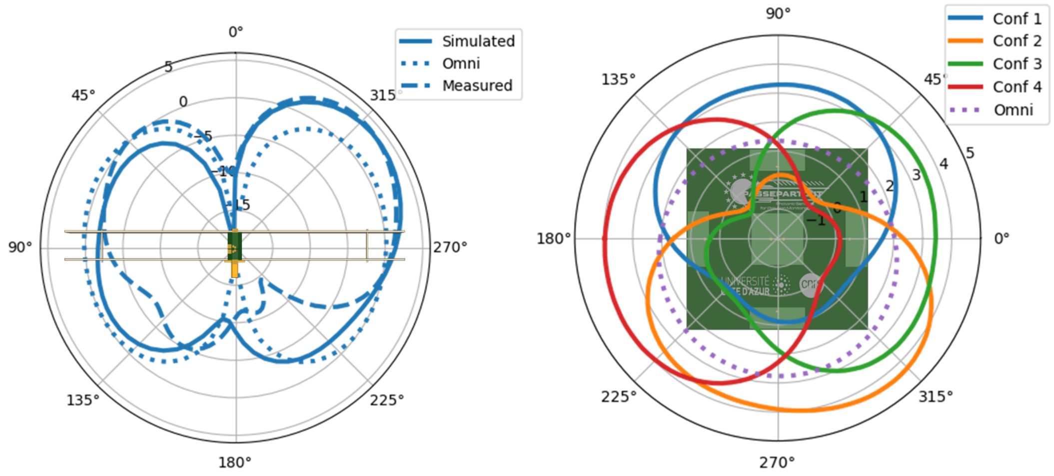

(a) **(b)**

Figure 3.3.6: Simulated and measured Realized Gain ϕ = 0 cut for a single directive beam in dBi (a) and Measured Realized Gain θ = 45 cut for the 4 directive configurations in dBi (b). Both cases compared to the omnidirectional configuration.

3.3.3 Transceiver Integration

As part of an airborne based portable terminal for real-time air quality monitoring, the antenna system has been conceived to house all the circuitry needed to send to ground the measured data using the LoRaWAN® protocol. This choice has been made to electrically and mechanically isolate the communication system from the drone and its payload. For this reason a board with integrated ATmega328 microcontroller and RFM95 radio module [39] has been fixed under the PCB used as ground-plane with the LoRa module RF output pin soldered to the central via of the antenna system replacing the SMA connector. There are 4 couples of wires connecting the board to each snap-fit parasitic element shorting PCB, in order to bias the lying diodes and electrically switch the beams (Figure3.3.7). The board is powered by an external battery, fixed on the back of the ground plane too.

A further enhancement in the transceiver integration has been made with another version presented in Figure 3.3.7 where an Arduino Nano, and RFM95 footprints have been directly included in the design of the ground plane PCB together with the biasing lines for the snap-fit PCBs, which have been properly modified to bring the DC bias at both extremes of the diodes. This prototype reduces the interference due to free wires running through the structure and it is more solid since all components are now soldered on the PCB itself. The integration of the widely used Arduino Nano make the design of this prototype a perfect candidate for low cost, easy-to-assemble antenna for any IoT application using the 868 MHz frequency band.

3.3.4 On-Field Test

For a practical evaluation of the advantages of using the proposed antenna on UAVs for long range transmission, an open area test site has been set as in Figure 3.3.8 employing an hexacopter in Line-of-Sight (LoS) piloting.

The testing system is based on the collection of RSSI samples during a LoRaPHI packet exchange. Sampling is done at the ground station by the proposed reconfigurable antenna. Another copy of the

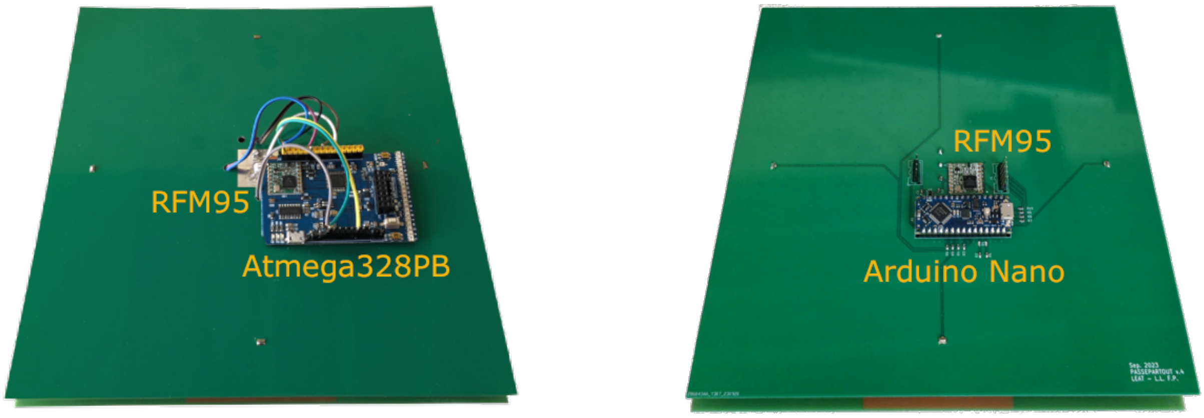

(a)

(b)

Figure 3.3.7: First version of Atmega328 based microcontroller (a) and PCB Arduino Uno version (b).

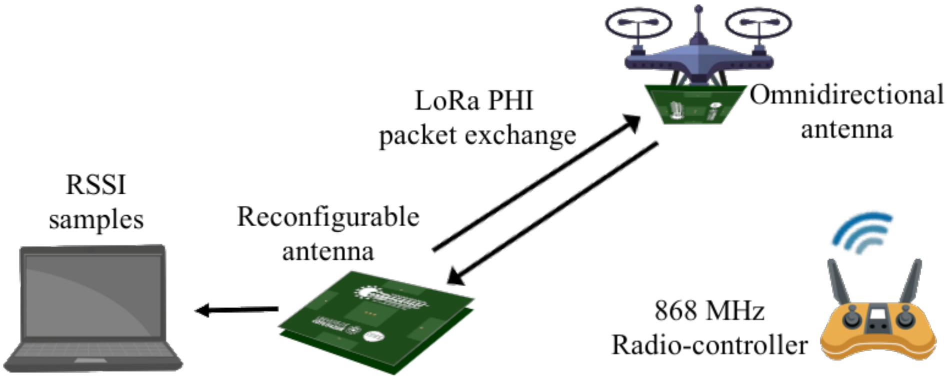

Figure 3.3.8: Diagram of the on-field test setup.

antenna is mounted on the drone thanks to a 3D printed supporting structure which guarantees a fair isolation with the metal parts that pertain to the drone as shown in Figure 3.3.9. The antenna on the ground can reconfigure its radiation diagram as explained in the previous sections, while the one mounted on the drone is set to radiate omnidirectionally (all PIN-diodes OFF).

All collected samples have been then combined with the drone flight positions at synchronous timestamps in post-processing. At each drone position, measurements have been averaged over 15 samples collected every second.

During the on-field test, 2 different scenarios have been considered: A. the distance scenario, aiming at evaluating the communication performance when the drone is moving away from the ground station, and B. the rotation scenario, where the drone is rotating around the ground station at fixed distance.

A. Distance scenario

In the first scenario, RSSI values were sampled for all ground antenna configurations along a straight-line drone path. The objective was to test communication performance over distance while maintaining a consistent relative antenna orientation, as shown in Figure 3.3.10. Due to LoS requirements and country flying regulations, the maximum distance was limited to approximately 350 m from the ground station

Figure 3.3.9: Photo of the proposed antenna mounted on the hexacopter drone during the flight.

location and 50 m in height. Keeping the height constant at 45 m, this limitation resulted in the angle to the ground converging to 8° at the furthest point of the drone's flight. Although the main lobe of the directive radiation pattern was not pointing its maximum to the drone, the radiation in that direction still lies in the -3 dB HPBW range, thus having a relatively low effect in terms of RSSI variation.

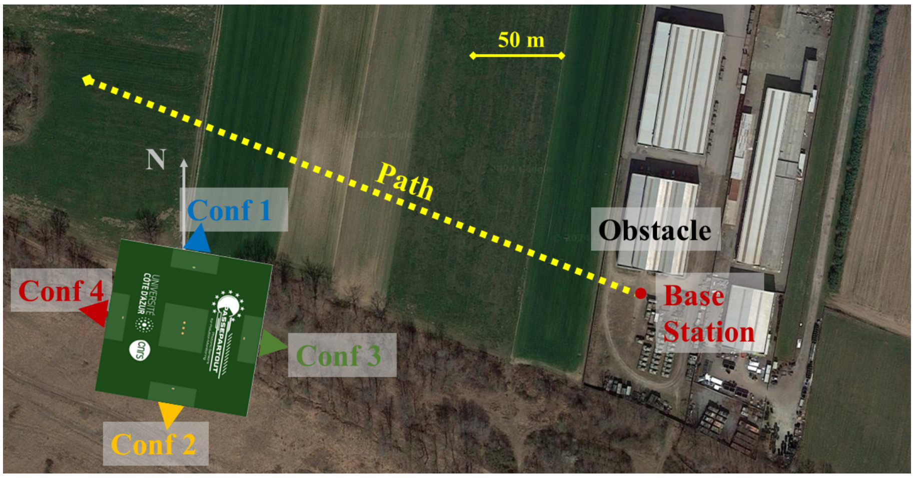

Figure 3.3.10: Path top view for measurement on distance referring to Conf 4. A reference of the Base Station antenna orientation and its location is pointed in red.

Figure 3.3.11 shows a comparison of the collected RSSI measurements with the theoretical values calculated through the Friss formula for free-space propagation. These latter have been computed as:

$$RSSI_{est} = 10\log_{10}\frac{P_R}{1mW} \tag{3.3.1}$$

where P_R is expressed in mW [40], and have been estimated in dBm from as follows:

$$P_R = P_T + G_T + G_R - L_f - L_{device} \tag{3.3.2}$$

Where P_T is the transmitter power, G_T and G_R the transmitter and receiver gains, respectively, L_f the free-space path loss (calculated as in 3.3.3), and L_{device} losses introduced by the RF-modules or devices [41].

$$L_f = 20\log_{10} f_{MHz} + 20\log_{10} d_{km} + 32.4dB \tag{3.3.3}$$

Which is an equivalent and more convenient expression of 3.3.4:

$$L_f = 20\log_{10} f + 20\log_{10} d - 147.6dB \tag{3.3.4}$$

considering an isotropic receiver antenna with:

$$\frac{P_T}{P_R} = \left(\frac{4\pi d}{\lambda}\right)^2 \tag{3.3.5}$$

Measured RSSI data well agree with the theoretical values, except for some outliers obtained for *Conf 1* and *Conf 2* and for distances smaller than 100 m. This behavior can be addressed to the multiple reflections and scattering phenomena caused by the proximity of a building, across the direction of the respective reconfigurable beams.

As the distance from the ground station distance increases, the advantage given by the possibility of selecting the antenna configuration pointing at the drone is more evident. *Conf 4* enables RSSI values that are on average 5 dB greater than the other configurations, and almost 10 dB greater than those of *Conf 3*, which points in the direction opposite to the flight path.

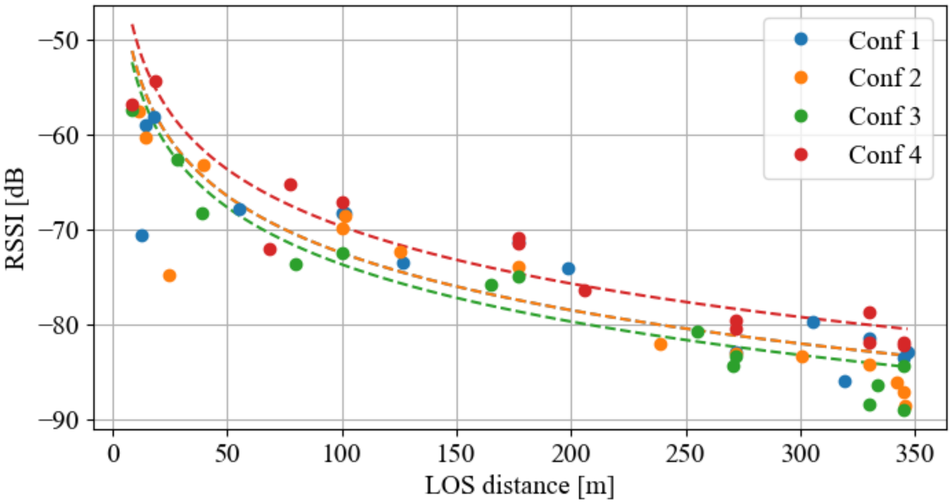

Figure 3.3.11: Averaged measured RSSI samples for each configuration compared to a qualitative free space loss trend (dashed lines), respectively.

B. Rotation scenario

The objective of the second on-field test scenario is to evaluate the use of steerable directive beams to provide the best physical channel. This has been carried out by sampling RSSI values with the drone circling around the base station at a fixed altitude of 17.5 m and distance of 28 m.

The obtained results are depicted in Figure 3.3.12, which show the RSSI values measured by each antenna configuration for all the different angular directions (the direction at 0° being the one corresponding to *Conf 1*). The RSSI values (points) for each configuration are plotted together with the corresponding simulated realized gain curve (dashed line). As it can be noticed, RSSI levels consistently reach their maximum at the corresponding angle of the ESPAR configuration, at only exception of *Conf 1*, which corresponds to the direction of the closest building, where a lower value can be spot at 0°. Losses in this case can be addressed to multiple reflections that, in this scenario, play an important role as the drone never exceed 28 m LoS distance from the ground station and, at his most, about 50 m from the building.

Moreover, even if at such a small communication distance RSSI samples can be scattered, as shown in Figure 3.3.11, differences between opposite configurations are remarkable (about 5 dB between *Conf 1* and *Conf 2* at 0°, and between *Conf 4* and *Conf 3* at -90°).

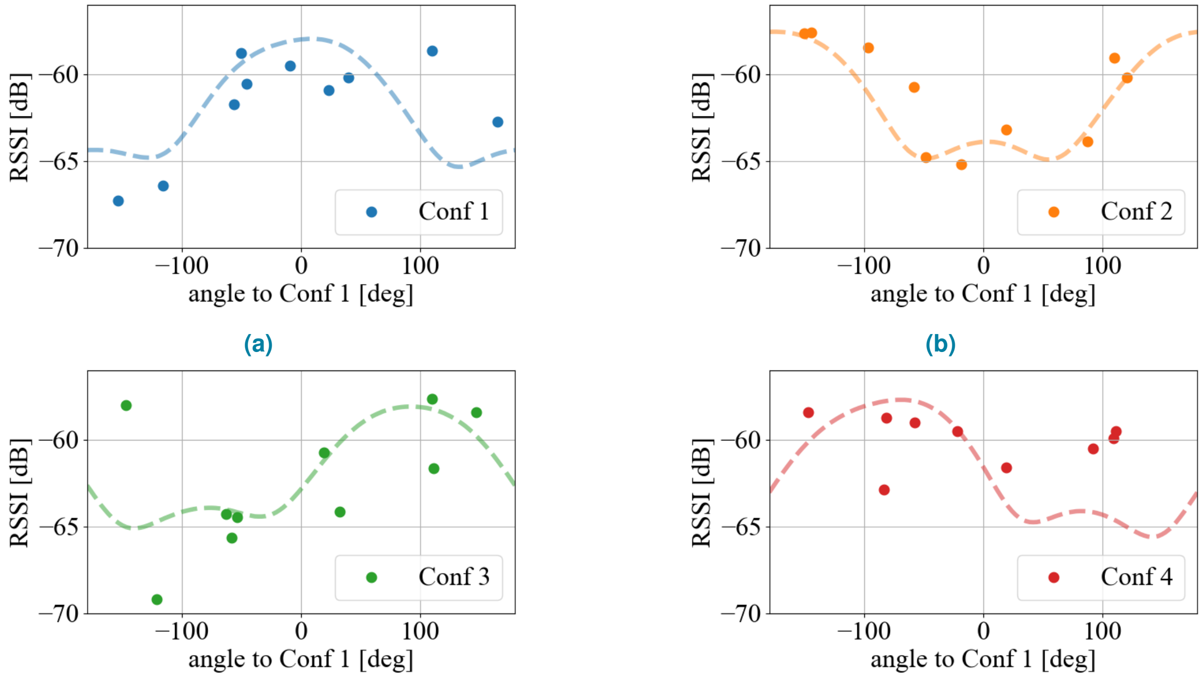

(a)

(b)

(c)

(d)

Figure 3.3.12: Averaged measured RSSI for each configuration compared to a qualitative radiation patternshape over the same angles (dashed line), respectively.

3.4 Performance Assessment and Calibration of Arbitrarily Conformal Additively Manufactured Phased Arrays for Wearable, Deployable, and Morphing RF Applications

In this section, a 4 × 5 series-fed patch phased-array design is presented and its combination of mechanical and electrical beam forming assessment is proposed through three folding configurations: convex, concave, and accordion-like. The design process and a discussion on the effects of shape changing configurations is presented, along with the its additively manufacturing fabrication process.

3.4.1 Phased Array Design

The design process follows three steps: first, a five element series-fed patch radiator is designed and optimized in CST Microwave Studio at 9.75 GHz. Next, a phased array is formed using four series-fed elements, yielding a total of 4 × 5 patches. Finally, the Beam Former Integrated Circuit (BFIC) footprint and necessary bias lines are routed.

The single radiator structure design is based on the design procedure outlined in [1]. The whole phased array structure including four series-fed patch, the BFIC and the relative routing have been conceived to be printed on a 0.13 mm thick Rogers® RO3003™ ($\varepsilon_r = 3$, $\tan\delta = 0.001$). The patch width and length are $Wp = 10.3$ mm and $Lp = 8.7$ mm, respectively. The distance between the series patches is increased sequentially, starting from $L_{line1} = 6.11$ mm, and scaled by a factor of $k = 1.14$ to reach to $L_{line4} = 8.35$ mm between the 4^{th} and the 5^{th} patch. The additional line length results in a phase delay between the series patches which in turn minimizes the main lobe tilt across the elevation plane. The reflection coefficient of a single series-fed patch is measured and plotted in Figure 3.4.1, demonstrating resonance at 9.75 GHz.

The phased array series-patch distance have been considered as $d < \lambda/(1+\sin\theta)$ in order to avoid grating lobes [42]. Figure 3.4.2a presents the geometry of the proposed structure and its design parameter are defined in Table 3.4.1.

The proposed phased array is based on the use of the AWS-0101 X-Band Silicon RADAR Quad Core Integrated Circuit (IC) from Qorvo®. The AWS-0101 BFIC provides dual beam Reception (RX) and single beam Transmission (TX), with a 6-bit phase and gain control resulting in a step resolution of 5.625° and 0.5 dB, respectively, over its operational frequency range of 8.5 – 10.55 GHz.

Table 3.4.1: series-fed patch antenna dimensions

Param.	W	L	L_{line1}	W_{line}	W_p	L_p	d
val.	63.33	81.2	6.11	0.6	10.3	8.7	15.83

The simulated results of the proposed phased array are shown in Figure 3.4.3. A steering range of ±45° is achieved, with a maximum realized gain of 13.5 dBi and SLL of –13.7 dB at boresight. The gain and SLL degrade with beam-steering, reaching 10.0 dBi and –6.4 dB, respectively, when the beam is steered to ±45°.

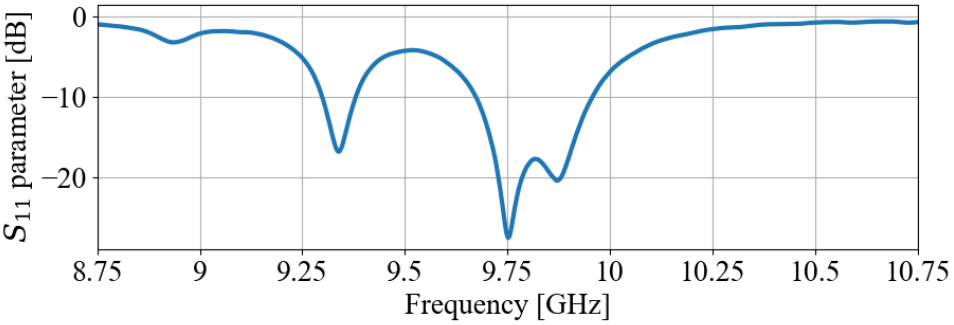

Figure 3.4.1: Planar Array active reflection coefficient on port 1.

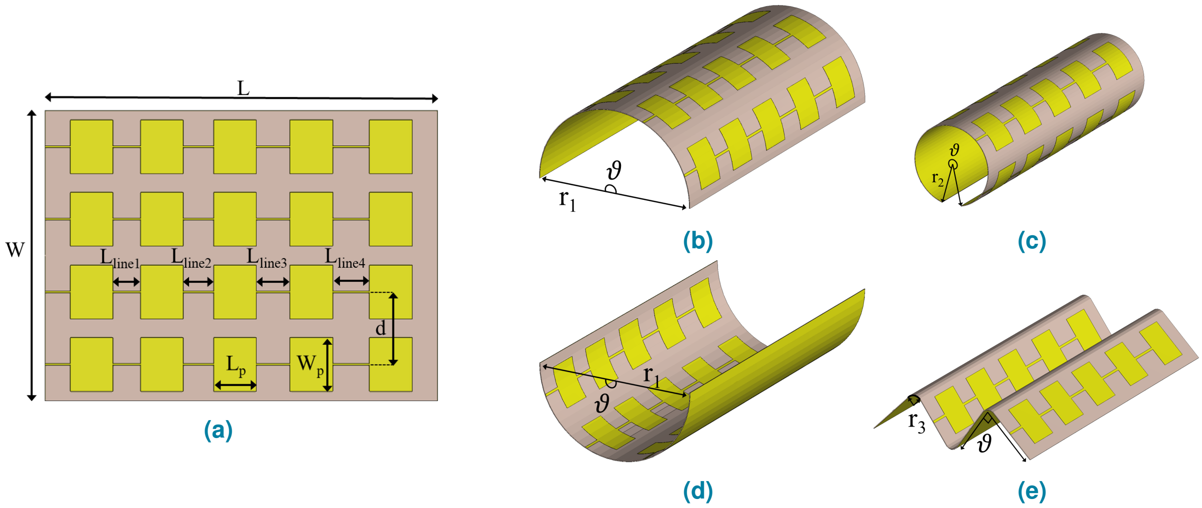

(a) (b) (c) (d) (e)

Figure 3.4.2: Series-fed patch phased array structure geometry (a) design parameters of the planar configuration, and shape changing configurations: (b) convex, (c) 360° convex, (d) concave, and (e) accordion-like shape.

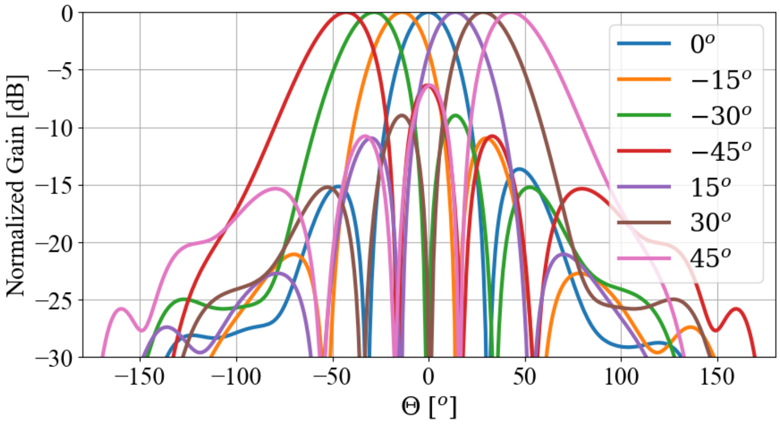

Figure 3.4.3: Beam-steering capability of the proposed planar phased array.

3.4.2 Shape-Changing Phased Array

In order to provide a wide assessment of the possible shape-changing configurations of the phased array, three configurations have been considered folding along the array's transversal axis: convex, concave and accordion-like configurations. As an array's shape undergoes alterations, its elements' relative positions and orientations shift, effectively transforming it into a new array. These changes modify the phased array's radiation characteristics, leading to a sub-optimal radiation pattern and a shift in beam angles. Consequently, calibrating element excitation phases becomes imperative to compensate for these changes and re-focus and/or uphold desired beam properties. Additionally, strategic selective activation of specific elements is utilized to achieve desired beam-shaping through the optimal combination of element patterns. Due to geometrical symmetry, radiation pattern analysis and simulations are performed on positive scanning angles only.

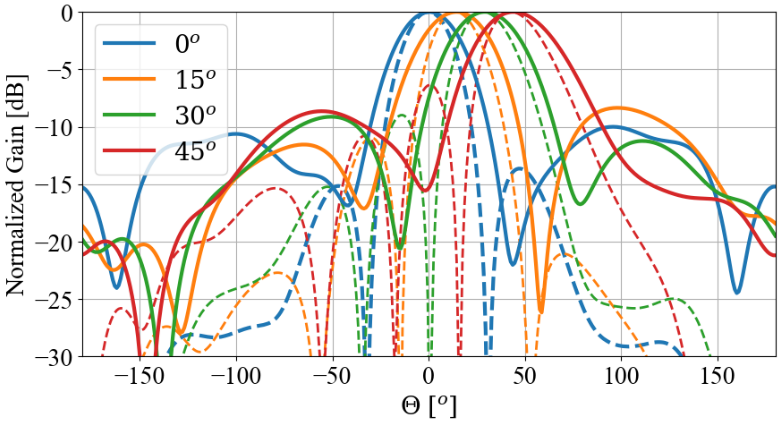

Figure 3.4.4: Radiation patterns comparison between the planar (dashed) and semicircle convex configuration (solid) for positive steering angles; $\vartheta = 180°$.

Convex

Convex folding of the phased array is the most versatile configuration, yielding highly reconfigurable and diverse radiation patterns. With small folding angles (< 180°) the achieved performance is comparable to the planar array. On the other hand, despite the modified and sub-optimal relative position of the elements for larger angles up to a 360°, selective activation of elements is used to achieve larger coverage angles.

A convex folding of the array on a cylindrical radius of 20 mm and 11 mm is considered. This results in folding angles of nearly $\vartheta = 180°$ and $\vartheta = 360°$, respectively, where the folding angle and the cylindrical radius are related through the substrate length, given by $\vartheta = \frac{L}{r}$. The 180° folding angle, or semicircle fold, results in the reduction of the projected surface area by 37%, occupying $40 \times 82.53 = 3301.2$ mm^2 instead of $63.33 \times 82.53 = 5226.6$ mm^2.

The beam-steering capability of the calibrated semicircle folded phased array and its planar counterpart is presented in Figure 3.4.4. As for the planar array, the more the beam is steered the worst the SLL. With the proper choice of amplitude and phase shift between array elements the SLL can be improved. For example, when the beam is pointing to 45°, it is –8.6 dB for the convex case while being –6.4 dB for the planar configuration. Moreover, with the semicircular convex shape, the spatial location of the elements

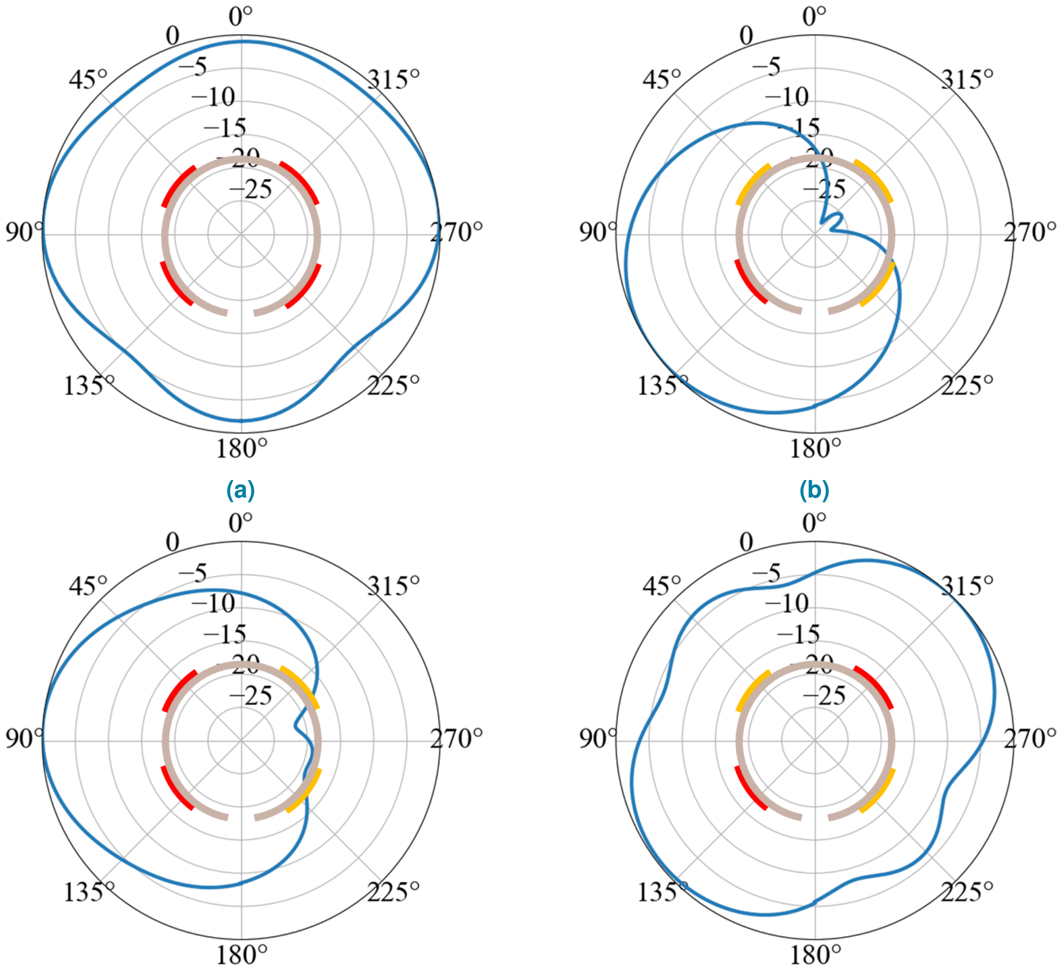

(a)

(b)

(c)

(d)

Figure 3.4.5: Radiation plots of the 360° convex shape with all elements configured to beam at boresight. Selective activation of different elements is used, with red elements being “on", and yellow elements being “off": (a) full activation, (b) activation of one series-fed patch, (c) activation of two consecutive series-fed patched, and (d) activation of two non-consecutive series-fed patched. Note that each 5-element series-fed patch is represented as a single “element".

can improve the elevation coverage as the boundary elements are pointing to different directions.

The 360° convex folding shape is the most representative of the large coverage for selective activation. In Figure 3.4.5 (a) when all element radiate boresight an omnidirectional beam is produced, while rotation of 45° can be obtained activating one or two consecutive array elements (Figure 3.4.5 (b), 3.4.5 (c)).

Concave

The concave configuration is a dual to the convex configuration. Despite the fact that it shares the same geometrical structure, the array’s performance is strongly affected by the coupling of opposing elements, and being more sensitive at smaller folding angles. In Figure 3.4.6, the calibrated radiation pattern of a semicircular 180° folded phased array is compared to its planar counterpart, for various beam angles and selective activation configurations. However, even when selective activation is utilized, this array’s geometry renders it challenging to beamsteer beyond 30° without major losses. As evident from

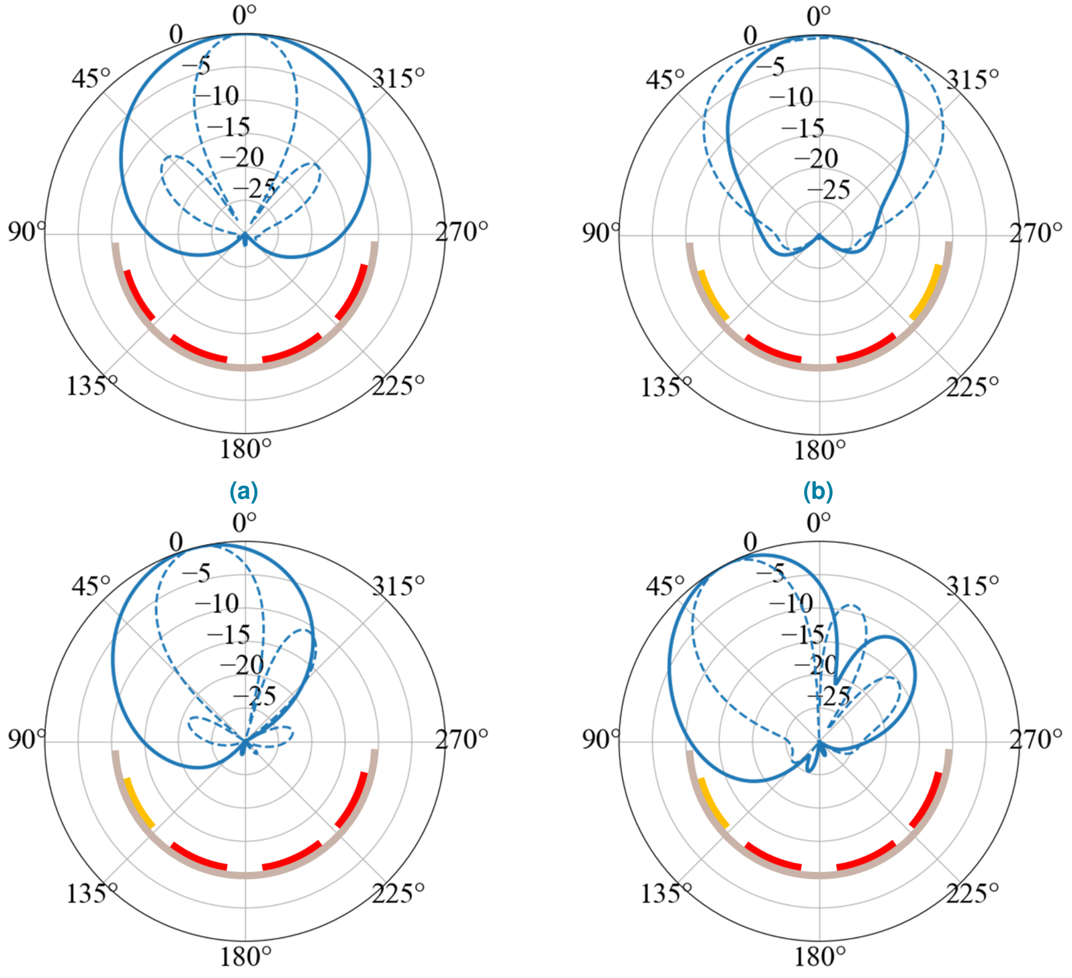

(a)

(b)

(c)

(d)

Figure 3.4.6: Comparison between the radiation patterns of the semicircle concave configuration (solid), and planar (dashed) configurations for (a) boresight, (b) selective boresight, (c) 15° and (d) 30°. Red elements being “on", and yellow elements being “off". Note that each 5-element series-fed patch is represented as a single “element".

Figure 3.4.6 (a) and Figure 3.4.6 (b), in addition to phase compensation, selectively activating the center elements of the concave configuration refocuses the beam, and therefore increases the directivity and reduces the half-power beamwidth. Additionally, Figure 3.4.6 (c) and Figure 3.4.6 (d) plot the re-calibrated beams of the concave structure as to match the planar configuration, while selectively activating three of the four elements.

Accordion-like

An accordion-like folded shape is obtained by bending the substrate between the series-fed patch in opposite directions. The bend is considered to be rounded around a cylindrical radius of 2 mm. In Figure 3.4.7 calibrated radiation patterns from a 90° bent accordion and the planar phased array are presented and they show high similarities. With a 90° folding between accordion faces the overall structure projected surface area is reduced by 30%. On the other hand, the directivity is found to be reduced by 3.2 dB, or

16% compared to the planar configuration. Additionally, the HPBW is increased by 47%. Even in this case a selective activation can improve the beam-steering elevation range for angles greater than ±45°.

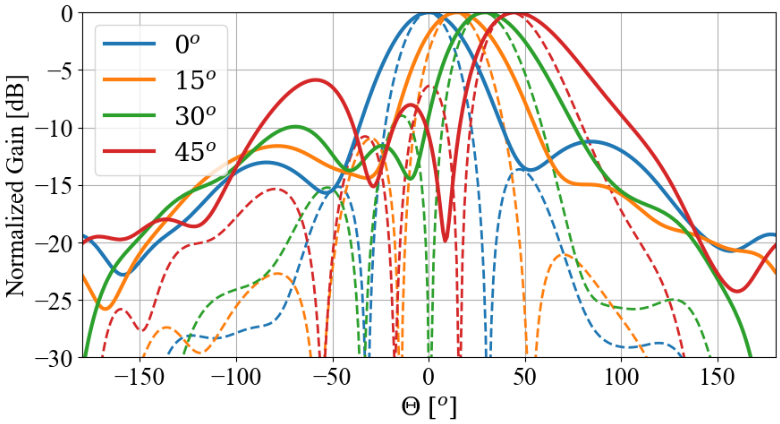

Figure 3.4.7: Radiation pattern comparison between planar (dashed) and accordion-like configuration (solid) for positive steering angles; ϑ = 90°.

3.4.3 Fabrication

The conformal phased array is additively manufactured using an inkjet printed masking technique followed by chemical etching. The antenna elements and RF circuitry are inkjet printed onto a flexible Rogers® RO3003™ (h = 130 um, ε_r = 3, tan δ = 0.001). Utilizing the Dimatix DMP-2831 inkjet printer, four layers of SU-8 photoresist are precisely deposited using a Samba cartridge with drop volume of 2.4 pL. Following this, a Ultra Violet (UV) crosslinker cures the resulting pattern, which is then submerged in a Ferric Chloride bath, etching any exposed copper. Finally, the substrate is washed with acetone (dimethyl ketone) to remove the SU-8 dielectric layers.

To ensure efficient thermal management, a 3 × 3 via array, featuring 0.2 mm via hole diameters, is dilled into the BFIC's ground pad and subsequently filled with conductive silver paste (LPKF ProConduct, ρ = 9.42 × 10^{-6} Ωm). Finally, the substrate undergoes thermal sintering at 160 $^\circ C$ for 30 minutes. Solder paste is then applied to all pads, followed by solder reflow utilizing a heat gun to affix the 7 × 7 mm QFN packaged BFIC. Wires are soldered to facilitate access to the biasing and Serial Peripheral Interface (SPI) control lines. Figure 3.4.8 shows the fabricated prototype in planar, folded, and convex configurations.

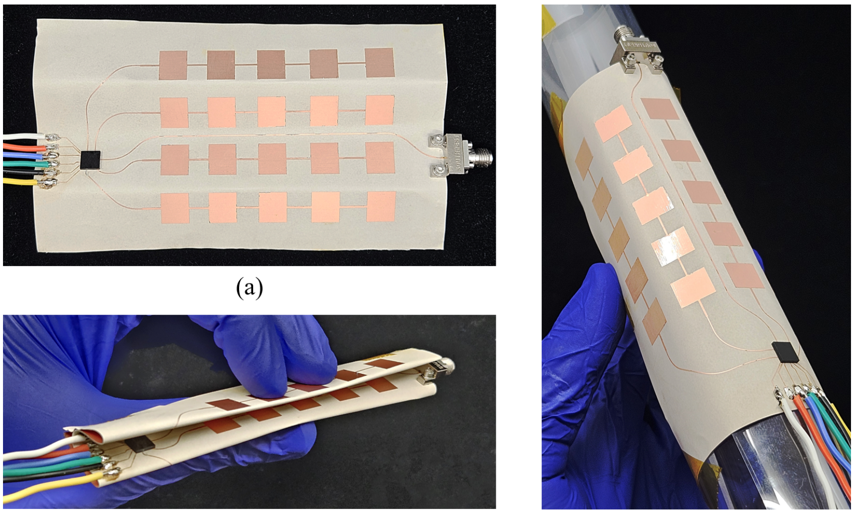

(a)

(b)

(c)

Figure 3.4.8: Fabricated conformal phased array in (a) planar, (b) folded (accordion-like), and (c) convex configurations.

3.5 Conclusions

In this chapter, an overview of pattern reconfigurable antenna arrays available in the literature has been introduced, with a focus on ESPARs and flexible, shape changing phased-arrays.

The designing an ESPAR of co-planar omnidirectional sources is discussed in Section 3.2. The design process included the validation of the proof of concept through the application of a PSO algorithm to maximize the realized gain in the desired direction for two similar structures, scaled to work at different frequencies, namely 5.075 GHz and 2.4 GHz, yielding similar results. All considerations were then validated by measurements on a prototype of the 5.075 GHz version, which align with expected simulated results. Finally, some considerations are made on the re-optimization problem, when it comes to integrating complex switching systems on the ESPAR to provide beam-switching capabilities in real-world scenarios. Looking forward, a prototype of a fully functioning beam switching ESPAR antenna is expected to complete the develpment cycle around the low-profile 7-element ESPAR structure. Nonetheless, further real-world scenario discussions are needed to deepen the understanding of pattern reconfigurable antennas and their reconfigurable controls, which will be a crucial turning point not only for IoT but for next generations of cellular networks and more.

Another example of ESPAR is proposed in Section 3.3 to meet the requirements for low-profile, long-range, easy-to-assemble antennas for UAVs. The proposed five element ESPAR is designed to work at 868 MHz LoRa frequencies controlled by simple PIN-diodes. Despite this, the structure represent a versatile solution as it can also be used as an omnidirectional source. The proposed design is validated by a prototype which has been characterized both in a controlled environment and in a real-world scenario, on board of an hexacopter drone. On-field communication tests were performed to evaluate the advantages of the directive beam for coverage improvement and the reliability of the best physical channel choice when switching beams. The results of this study show that the longer the distance, the greater the dominance of using a directive beam to receive power. Moreover, choosing the proper directive beam can improve channel reliability even at short distances, permitting overall increases of the measured RSSI level. This approach provides a realistic assessment of antenna performance, reflecting the actual conditions under which these antennas operate. It has significant potential for wide-ranging applications and different types of antennas. However, it is expected to extend measurements over larger distances. This would enable a more comprehensive characterization of long-range communication protocols, providing an even more robust and versatile tool for antenna analysis.

Finally, in Section 3.4, a 4×5 phased array of four, 5-element series-fed patch elements is presented for arbitrarily conformal phased arrays for wearable, deployable, and morphing RF Applications. Its design on a thin flexible substrate and the assessment of multiple shape-changing configurations compared to the planar phased array as a reference is discussed, with an emphasis on the radiation pattern performance. The concave configuration shows a significant degrade in both radiation performance and steering range capability, even when select elements are used for the optimal performance. The convex configuration has been simulated up to a 360° fold angle, and shows that by strategically tuning the element amplitude and phase, a similar performance to the planar case can be obtained. Moreover, selective activation may be utilized to increase of the scanning coverage at the expense of a reduced gain. Finally, the accordion-like configuration proved to be the closest to the planar configuration in terms of radiation performance, and presents the possibility to increase the elevation coverage through different folding angles and selective element activation. Whether a phased array is to operate on a static conformal structure, or if intentional shape-change is utilized in conjunction with beam-steering to achieve additional pattern reconfigurability, understanding the performance of arbitrarily conformal phased arrays and applying the required beam calibration, will present diverse opportunities for advancements in communications and sensing applications.

References

[1] C. A. Balanis, *Antenna Theory: analysis and design*. Hoboken, New Jersey: John Wiley, 4 ed., 2016.

[2] H. Shakhatreh, A. H. Sawalmeh, A. Al-Fuqaha, Z. Dou, E. Almaita, I. Khalil, N. S. Othman, A. Khreishah, and M. Guizani, “Unmanned aerial vehicles (uavs): A survey on civil applications and key research challenges,” *IEEE Access*, vol. 7, pp. 48572–48634, 2019.

[3] P. Cohn, A. Green, M. Langstaff, and M. Roller, “Commercial drones are here: The future of unmanned aerial systems.” https://www.mckinsey.com/industries/travel-logistics-and-infrastructure/our-insights/commercial-drones-are-here-the-future-of-unmanned-aerial-systems, 2017.

[4] K. Maliatsos, P. S. Bithas, and A. G. Kanatas, “A low-complexity reconfigurable multi-antenna technique for non-terrestrial networks,” *Frontiers in Communications and Networks*, vol. 2, 2021.

[5] A. Debard, A. Clemente, A. Tornese, and C. Delaveaud, “On the maximum end-fire directivity of compact antenna arrays based on electrical dipoles and huygens sources,” *IEEE Transactions on Antennas and Propagation*, vol. 71, no. 1, pp. 299–308, 2023.

[6] A. Mohammadi and F. M. Ghannouchi, *MIMO Wireless Communications*, pp. 9–26. Berlin, Heidelberg: Springer Berlin Heidelberg, 2012.

[7] R. Harrington, “Reactively controlled directive arrays,” *IEEE Transactions on Antennas and Propagation*, vol. 26, no. 3, pp. 390–395, 1978.

[8] M.-C. Tang, B. Zhou, and R. W. Ziolkowski, “Low-profile, electrically small, huygens source antenna with pattern-reconfigurability that covers the entire azimuthal plane,” *IEEE Transactions on Antennas and Propagation*, vol. 65, no. 3, pp. 1063–1072, 2017.

[9] M.-C. Tang, Y. Duan, Z. Wu, X. Chen, M. Li, and R. W. Ziolkowski, “Pattern reconfigurable, vertically polarized, low-profile, compact, near-field resonant parasitic antenna,” *IEEE Transactions on Antennas and Propagation*, vol. 67, no. 3, pp. 1467–1475, 2019.

[10] Y. Yang and X. Zhu, “A wideband reconfigurable antenna with 360° beam steering for 802.11ac wlan applications,” *IEEE Transactions on Antennas and Propagation*, vol. 66, no. 2, pp. 600–608, 2018.

[11] L. Santamaria, F. Ferrero, R. Staraj, and L. Lizzi, “Slot-based pattern reconfigurable espar antenna for iot applications,” *IEEE Transactions on Antennas and Propagation*, vol. 69, no. 7, pp. 3635–3644, 2021.

[12] L. Santamaria, F. Ferrero, R. Staraj, and L. Lizzi, “Electronically pattern reconfigurable antenna for iot applications,” *IEEE Open Journal of Antennas and Propagation*, vol. 2, pp. 546–554, 2021.

[13] D. Wolpert and W. Macready, “No free lunch theorems for optimization,” *IEEE Transactions on Evolutionary Computation*, vol. 1, no. 1, pp. 67–82, 1997.

[14] A. D. Boursianis, M. S. Papadopoulou, M. Salucci, A. Polo, P. Sarigiannidis, K. Psannis, S. Mirjalili, S. Koulouridis, and S. K. Goudos, “Emerging swarm intelligence algorithms and their applications in antenna design: The gwo, woa, and ssa optimizers,” *Applied Sciences*, vol. 11, no. 18, 2021.

[15] B. Schaer, K. Rambabu, J. Bornemann, and R. Vahldieck, “Design of reactive parasitic elements in electronic beam steering arrays,” *IEEE Transactions on Antennas and Propagation*, vol. 53, no. 6, pp. 1998–2003, 2005.

[16] Q. Han, B. Hanna, K. Inagaki, and T. Ohira, “Mutual impedance extraction and varactor calibration technique for espar antenna characterization,” *IEEE Transactions on Antennas and Propagation*, vol. 54, no. 12, pp. 3713–3720, 2006.

[17] M. Thevenot, C. Menudier, A. El Sayed Ahmad, G. Zakka El Nashef, F. Fezai, Y. Abdallah, E. Arnaud, F. Torres, and T. Monediere, “Synthesis of antenna arrays and parasitic antenna arrays with mutual couplings,” *International Journal of Antennas and Propagation*, vol. 2012, no. 1, p. 309728, 2012.

[18] D. P. Lynch, M. M. Tentzeris, V. Fusco, and S. D. Asimonis, “Super realized gain antenna array,” *IEEE Transactions on Antennas and Propagation*, vol. 72, no. 9, pp. 7030–7040, 2024.

[19] Y.-S. Choi, J.-S. Park, and W.-S. Lee, “Beam-reconfigurable multi-antenna system with beam-combining technology for uav-to-everything communications,” *Electronics*, vol. 9, no. 6, 2020.

[20] Y.-S. Choi and W.-S. Lee, “Reconfigurable beam switching antenna with horizontal parasitic element reflector (hper) for uav applications,” in *2020 IEEE International Symposium on Antennas and Propagation and North American Radio Science Meeting*, pp. 433–434, 2020.

[21] R. Movahedinia, A.-R. Sebak, M. R. Chaharmir, M. Ranjbar Nikkhah, and A. A. Kishk, "x -band circularly polarized electronically steerable parasitic array radiator of dra," *IEEE Transactions on Antennas and Propagation*, vol. 66, no. 2, pp. 721–728, 2018.

[22] R. De Marco, E. Arnieri, G. Amendola, and L. Boccia, "Microstrip espar antenna with conical beam scanning," *IEEE Antennas and Wireless Propagation Letters*, vol. 23, no. 1, pp. 174–178, 2024.

[23] M. Burtowy, M. Rzymowski, and L. Kulas, "Low-profile espar antenna for rss-based doa estimation in iot applications," *IEEE Access*, vol. 7, pp. 17403–17411, 2019.

[24] J. Pokorny, A. Ometov, P. Pascual, C. Baquero, P. Masek, A. Pyattaev, A. Garcia, C. Castillo, S. Andreev, J. Hosek, and Y. Koucheryavy, "Concept design and performance evaluation of uav-based backhaul link with antenna steering," *Journal of Communications and Networks*, vol. 20, no. 5, pp. 473–483, 2018.

[25] M. Groth, M. Rzymowski, K. Nyka, and L. Kulas, "Espar antenna-based wsn node with doa estimation capability," *IEEE Access*, vol. 8, pp. 91435–91447, 2020.

[26] Y. Wang, M. Han, W. Dou, and T. Li, "3-d printed all-metal conformal circularly polarized reflectarray antenna at x-band," *IEEE Transactions on Antennas and Propagation*, pp. 1–1, 2024.

[27] R. K. Baudh, S. Sahu, M. S. Parihar, and V. Dinesh Kumar, "A semi-flexible conformal beam scanning broadband wearable antenna array for radar application," in *2023 IEEE 7th Conference on Information and Communication Technology (CICT)*, pp. 1–4, 2023.

[28] L. I. Balderas, A. Reyna, M. A. Panduro, C. Del Rio, and A. R. Gutiérrez, "Low-profile conformal uwb antenna for uav applications," *IEEE Access*, vol. 7, pp. 127486–127494, 2019.

[29] M. R. M. Hashemi, A. C. Fikes, M. Gal-Katziri, B. Abiri, F. Bohn, A. Safaripour, M. D. Kelzenberg, E. L. Warmann, P. Espinet, N. Vaidya, E. E. Gdoutos, C. Leclerc, F. Royer, S. Pellegrino, H. A. Atwater, and A. Hajimiri, "A flexible phased array system with low areal mass density," *Nature Electronics*, vol. 2, 2019.

[30] M. W. Nichols, A. Gonzalez, E. A. Alwan, and J. L. Volakis, "An accordion-folding series-fed patch array with finite thickness: A folding technique for cubesat arrays," *IEEE Antennas and Propagation Magazine*, vol. 65, no. 3, pp. 77–82, 2023.

[31] S. V. Georgakopoulos, C. L. Zekios, A. Sattar-Kaddour, M. Hamza, A. Biswas, B. Clark, C. Ynchausti, L. L. Howell, S. P. Magleby, and R. J. Lang, "Origami antennas," *IEEE Open Journal of Antennas and Propagation*, vol. 2, pp. 1020–1043, 2021.

[32] D. E. Williams, C. Dorn, S. Pellegrino, and A. Hajimiri, "Origami-inspired shape-changing phased array," in *2020 50th European Microwave Conference (EuMC)*, pp. 344–347, 2021.

[33] M. Gal-Katziri, A. Fikes, and H. A., "Flexible active antenna arrays," *npj Flex Electron*, vol. 6, no. 85, 2022.

[34] A. Dellabate, V. Lazzoni, A. Monorchio, and D. Brizi, "Arbitrarily conformal metasurfaces for enhanced wireless power transfer systems," *IEEE Access*, vol. 12, pp. 64376–64384, 2024.

[35] A. Fikes, O. S. Mizrahi, and A. Hajimiri, "A framework for array shape reconstruction through mutual coupling," *IEEE Transactions on Microwave Theory and Techniques*, vol. 69, no. 10, pp. 4422–4436, 2021.

[36] A. C. Fikes, M. Gal-Katziri, O. S. Mizrahi, D. E. Williams, and A. Hajimiri, "Frontiers in flexible and shape-changing arrays," *IEEE Journal of Microwaves*, vol. 3, no. 1, pp. 349–367, 2023.

[37] H. Al Jamal, C. Hu, N. Wille, and M. M. Tentzeris, "Beyond planar: An additively manufactured, origami-inspired, and shape-changing RFIC-based phased array for near-limitless radiation pattern reconfigurability in 5G/mmWave applications," *IEEE Microwave and Wireless Technology Letters*, 2024.

[38] L. Alliance, "Lora and lorawan: Technical overview." https://lora-developers.semtech.com/documentation/tech-papers-and-guides/lora-and-lorawan/, 2023.

[39] F. Ferrero, "UCA21." https://github.com/FabienFerrero/UCA21, 9 2021.

[40] Mobilefish, "Lora documentation." https://lora.readthedocs.io/en/latest/, 2023.

[41] *Radio Wave Fundamentals*, ch. 1, pp. 1–33. John Wiley & Sons, Ltd, 2013.

[42] R. Mailloux, *Phased Array Antenna Handbook, Third Edition.* Artech House, 2017.

4 Frequency reconfigurable

4.1 Introduction

A straightforward method for adjusting the resonant frequency of an antenna, thereby enabling frequency reconfigurability, involves integrating the antenna with tunable RF circuits. For example, [1] introduced a “filtenna” [Figure 4.1.1 (g)], a fusion of a reconfigurable composite filter and a wideband funnel-shaped monopole antenna. This design facilitates two operational states: a wideband state for sensing available radio frequencies and a tunable narrowband state for communications. These states are controlled by a single PIN-diode, while the continuous frequency reconfiguration is achieved using two Varicaps. The entire structure occupies a surface of $0.24 \times 0.39\ \lambda^2$. In [2] a dual-port antenna with an integrated rectifying circuit is proposed [Figure 4.1.1 (f)]. This design allows for autonomous switching between different operating frequencies, thereby eliminating the need for external DC bias voltage. The antenna operates at 2.1 GHz when excited at port-1, which serves as the input for the rectifying circuit. The rectifier converts received RF power into DC voltage, which then controls a PIN-diode. The diode acts as a switch between two higher frequencies (2.85 GHz and 5.52 GHz) at port-2, used for transmitting and receiving RF power. Despite the innovative nature of autonomous reconfiguration, it still requires bulky rectifiers and matching networks, limiting its potential in IoT applications.

Another strategy for reconfiguring the resonant frequency of an antenna involves leveraging the unique properties of certain materials. In [3] authors proposed a micro-strip antenna made from a P3HT organic semiconductor polymer. The antenna’s resonant frequency can be dynamically adjusted by varying the intensity of white light illumination. Although the reconfiguration is fast and the sweep continuous over a 1.5 GHz sweeping band (1.1 GHz to 2.6 GHz), its applications are limited due to sensitivity to environmental conditions. Moreover, compared to traditional copper micro-strip antennas, it has modest radiation efficiency and lower gain.

A basic patch antenna can be made frequency reconfigurable by incorporating a liquid metal droplet within a 3-D printed microfluidic channels [4] [Figure 4.1.1 (h)]. This liquid metal, specifically EGaIn (eutectic gallium indium), serves as a tunable element, effectively altering the antenna’s electrical properties and, consequently, its resonant frequency. By incorporating multiple pairs of slots into the patch antenna, a wide frequency tuning bandwidth is achieved, ranging from 1.9 GHz to 3.5 GHz. However, the complexity of integration and handling of liquid metal remains a significant challeng with this technology. Authors of [5] manipulated the flow of liquid metal by gravity [Figure 4.1.1 (i)], allowing the antenna to switch between different frequency bands and polarization modes. A square ring channel facilitates the movement of the liquid metal, eliminating the need for additional mechanical components or circuits. This provides a simple and efficient method to reconfigure the antenna's frequency. Four reconfiguration states allow the switchable band to range between 1.2 GHz and 5.4 GHz. However, the antenna's sensitivity to orientation makes the frequency reconfiguration difficult to control. Instead of liquid metal, water can be used to frequency reconfigure a DRA [6] [Figure 4.1.1 (j)]. This method combines two techniques: mode reconfiguration and dielectric loading. The antenna operates with mode TE^{y}_{11} at 2.4 GHz and by pumping water in a microfluidic cavity, it can switch to a quasi-TE^{y}_{13} at 3.6 GHz and is continuously tunable with the water level in this range.

Frequency reconfiguration can also be achieved through origami-like folds [7]. The proposed antenna is designed to operate at two frequencies depending on whether it is folded or unfolded [Figure 4.1.1 (e)]. In the unfolded state, the antenna is a flat dipole that operates at 1.23 GHz, while in the folded state, it assumes a cubic shape, switching the frequency to 0.77 GHz. Despite the novelty and ease of deployment of this technology, there are still challenges in the integration of actuators and motors, suggesting that the origami-inspired technology is not yet mature enough for widespread consumer use.

The most common method for adjusting the resonant frequency of an antenna involves the use of diodes. Varicap diodes are used for continuously tuning of the resonant frequency, while PIN-diodes are used to discrete switching between available frequencies. In [8] authors proposed a NFRP element made of a capacitively-loaded loop that uses a Varicap to tune the frequency of a monopole antenna. The measured frequency agility range is 0.9399-1.0052GHz. The study also demonstrated through simulations that the choice of the Varicap significantly influences the resonance frequency reconfiguration range. By incorporating a Defected Ground Structure (DGS) and a reconfigurable micro-strip feedline, an antenna can adjust it's operating frequency using Varicaps [9]. This four-port dual-band Multi Input Multi Output (MIMO) antenna can continuously adjust its operating frequency tuning the Varicap feeding voltage. The continuous operating frequency ranges from 1.3 to 1.8 GHz for the lower band and from 1.8 to 2.6 GHz for the higher band. Despite the detailed design process, the antenna's relatively high complexity and its array structure make it unsuitable for IoT applications. A frequency reconfigurable antenna designed for IoT applications is proposed by [10]. The antenna's design is based on an octahedral shape with an omega-shaped slot, allowing for switching between various configurations to achieve different resonant frequencies [Figure 4.1.1 (c)]. The use of all combinations of two PIN-diodes allows multiple bands to be reached simulataneously, namely S-band, C-band and X-band. A reconfigurable patch antenna design that can be dynamically adjusted to operate at different frequencies and polarizations is proposed in [11] [Figure 4.1.1 (b)]. Twelve switchable shorting pins are used to switch between eight distinct frequency bands ranging from 1.85 GHz to 2.63 GHz. Additionally, 17 PIN-diodes are used to tune this antenna's polarization.

All these systems that work with diodes require a DC bias network, which must be separated and isolated from the RF on the antenna structure. This complexity is avoided in [12] where a trapezoidal patch shorted to ground through two Varicaps is presented. The Varicaps act in a dual configuration, granting a reconfiguration on two bands. Their bias is made through the RF feed, simplifying the antenna's design and avoiding the negative effects of bias line coupling and radiation. The antenna reconfiguration frequencies range between 410 MHz and 990 MHz and between 2.1 GHz and 3.5 GHz. The work addresses the complexity of combining frequency reconfigurable and miniature structures, highlighting the inverse relation between tuning range and efficiency.

Despite the inherent miniaturization of loop structures due to their small size relative to the wavelength, there is a scarcity of literature that addresses frequency reconfiguration applied to these structures. This is likely because loop structures, known for their very narrow bandwidth, experience a significant reduction in efficiency when tuning the resonant frequency In [13], a tunable slot-loop antenna miniaturized by periodically loading it with Varicaps is presented. This method effectively slows down the guided wave, enabling the antenna to operate at lower frequencies while occupying a small footprint. Eight Varicap are used to develop a continuous frequency reconfiguration between 2.34 GHz and 4 GHz. However, the mismatch caused by Varicap as a capacitive load becomes so great that S_{11} for frequencies lower than 3.5 GHz never reaches -10 dB. A frequency reconfigurable rectangular loop antenna capable of operating on three frequency bands (2.7-3.1 GHz, 3-3.5 GHz, and 3.5-4.5 GHz) is also proposed in [14] [Figure 4.1.1 (a)]. This is achieved simply by switching the states of four PIN-diodes. This work also underlines the miniaturization capabilities of the loop antenna, in this case $0.2 \times 0.27 \times 0.015\ \lambda^3$, although only simulated results are available. In [15], a chip inductor is inserted at the midpoint of the loop as a load, while a series Varicap continuously tunes the resonance frequency [Figure 4.1.1 (d)]. The resulting equivalent tunable series of inductor and Varicap allows a reconfigurable frequency range between 2 GHz and 2.5 GHz. The size is remarkably small, just $0.07 \times 0.07\ \lambda^2$, but consequently, the measured efficiency is very low, never exceeding 14%.

In this chapter, a horizontally polarized magnetic dipole source made of a circular AL is proposed to work at Ultra High Frequency (UHF) bands for satellite communications. Despite its narrow band, typical of small loop antennas, it can provide a large coverage from licensed band 400 MHz and ISM 433 MHz thanks to a simple loading mechanism. Two examples are proposed for this purpose. The first one, discussed in Section 4.2, presents a study on the relation between miniaturization, bandwidth and efficiency using a Varicap as a load for a continuous frequency reconfiguration, covering the two required bands. Secondly, in Section 4.3, a model that uses a PIN-diode as a load is discussed with a focus on practical implementation. The designs principles are further demonstrated through measurements on a prototype of the PIN-diode reconfigurable version of the circular AL, showcasing the practical functionality and robustness of the design.

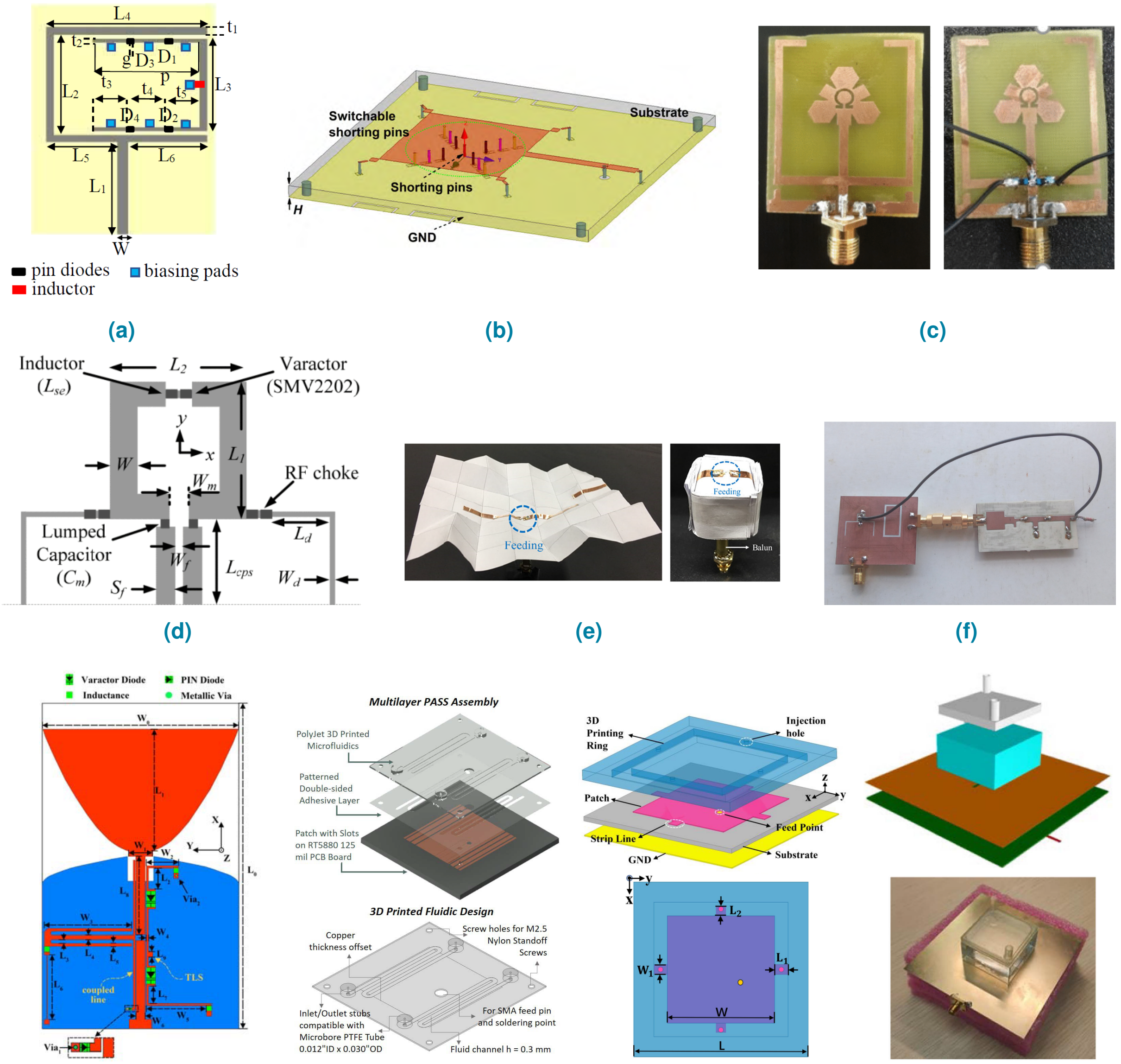

(a) (b) (c)

(d) (e) (f)

(g) (h) (i) (j)

Figure 4.1.1: Examples of frequency reconfigurable antennas: (a) a miniature frequency reconfigurable loop through PIN-diodes [14], (b) a reconfigurable patch antenna through PIN-diodes [11], (c) an octahedral multi-band frequency reconfigurable antenna through PIN-diodes [10], (d) A miniature Varicap-controlled loop [15], (e) origami-shaped antenna, both frequency reconfiguration states [7], (f) PIN-diode based self reconfigurable antenna through the use of rectifying circuit [2], (g) A filtenna with continuously tunable frequency reconfiguration through Varicaps and PIN-diodes [1], (h, i) Frequency reconfigurable antennas based on liquid metal and 3D printed microfluidic channels [4, 5], (j) frequency tunable DRA antenna through top loaded variable water level [6].

4.2 Frequency Agile Omnidirectional Antenna

The proposed antenna is based on the well known AL structure, a magnetic dipole source previously discussed in Section 2.2.2. The structure is differentially fed from the center, currents on the parallel lines compensate each other as they flow in opposite directions, resulting in the main currents responsible for the radiation being the one on the loop arms.

The proposed circular AL structure is shown in Figure 4.2.1. The two parts of the AL are designed to be printed on the opposite layers of a 1.6 mm thick single PTFE Teflon® PCB.

The implementation of variable capacitance loads between the AL arms provides continuous frequency agility, which compensates for the narrow-band behavior typical of miniature antennas.

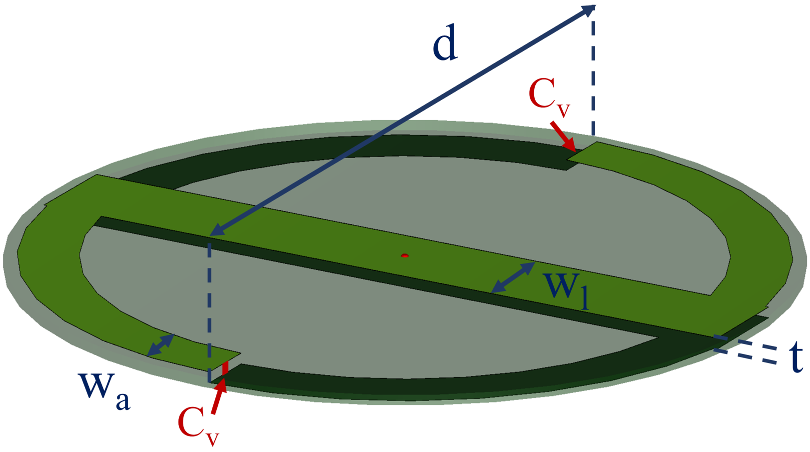

Figure 4.2.1: Proposed circular AL structure antenna.

4.2.1 Design and Miniaturization Process

As demonstrated in Section 4.1, capacitive loading of an antenna can greatly influence miniaturization, albeit at the expense of reduced efficiency. In an initial evaluation for miniaturization capabilities, an analysis of different substrate materials, each 1.6 mm thick, have been conducted. A substrate made of FR-4 epoxy fiberglass characterized by a relative permittivity $\varepsilon_r = 4.3$, an hydrocarbon ceramic Rogers RO4350B with $\varepsilon_r = 3.55$ and PTFE Teflon with $\varepsilon_r = 2.55$ have been considered. The antenna structure has been then optimized to have a minimum $|S_{11}|$ in 400 MHz over the three substrate, with results reported in Table 4.2.1.

Table 4.2.1: Comparison for different substrate permittivity when antenna is matched at 400 MHz. Performance are expressed in terms of Fractional Bandwidth (FB) and total efficiency.

Material	ε_r	d [mm]	d [λ]	FB [%]	Tot. efficiency [%]
FR-4	4.3	148	0.20	1.5	64
RO4350B	3.55	156	0.21	1.9	89
PTFE	2.55	168	0.22	2.5	92

As expected, the higher the permittivity, the more significant the miniaturization. For instance, with FR-4, the smallest diameter of 0.2 λ is obtained, but this comes with the lowest total efficiency of 64% and impedance bandwidth at -10 dB is only 6 MHz wide, ranging from 395 MHz and 401 MHz.

On the other hand, the RO4350B and the PTFE require a larger structure after optimization for the same working frequency, specifically 0.21 λ and 0.22 λ, respectively. For a 0.01 λ increase in size, RO4350B gains 25% in total efficiency compared to FR-4 while PTFE only 3% compared to RO4350B. However, PTFE has the widest FB of 2.5 % ranging from 396.3 to 405.9 MHz. For this reason, it is the preferred choice for this study.

The dimensions of the fundamental parameters of the final antenna design are reported in Table 4.2.2.

Table 4.2.2: Dimensions of the design parameters of the optimized model of the proposed bi-band AL antenna.

d [mm]	W_a [mm]	W_l [mm]	t [mm]
174	10	10	1.6

4.2.2 Reconfiguration Mechanism Implementation

The designed circular AL currently operates statically at the lower required frequency of 400 MHz. The presence of a tunable load, based on the inclusion of an Hyperabrupt Varicap Diode at the ends of the upper layer's AL arms connected to the correspondent arms in the bottom layer as a load, enables frequency agility. A re-optimization based on reactive loads have been implemented to recenter the resonance to the desired frequencies and refit total efficiencies.

The proposed structure employs two KV1983A Hyperabrupt Varicap Diodes by Microsemi, which ranges from 0.45 pF to 1.2 pF tuned by varying the voltage intensity, as per Table 4.2.3. The choice of the Varicap was made considering the high sensitivity and high Q of the Super Hyperabrupt cathegory of Varicaps, its small values of capacitance ranging from 0.45 pF to 1.2 pF, and relatively low biasing voltage up to 8 V maximum.

Table 4.2.3: Microsemi KV1983A Super Hyperabrupt Varactors High Sensitivity 1-8 V [16].

V_B [V]	1 V	1.5 V	2.5 V	4 V	8 V
C_V [pF]	1.2	1	0.83	0.6	0.45

Loading with a capacitor implies a resonance frequency shift to lower frequencies and a reduction in total efficiency, as shown in Figure 4.2.2, $|S_{11}|$ curves are never lower than -10 dB across all reconfiguration range which is out of the design band. Recenter the resonance frequency to the desired band can be achieved in two ways: by scaling the size of the AL structure, but this would maintain a low efficiency, or by introducing a parallel inductor to compensate the capacitive effects induced by the Varicap.

An equivalent parallel LC circuit is generated as load between the layers connecting the arms of the AL as shown in Figure 4.2.3. According to this scheme, and considering a null overall reactive component at the required frequency, the L and C in parallel must meet the relation $L = {}^1\!/_{\omega^2 C}$. For instance, for a 1 pF capacitance, a 158 nH inductance should correspond at 400 MHz. It goes without saying that not all combinations of reactive loads are physically feasible due to the demand for high values of Capacitors

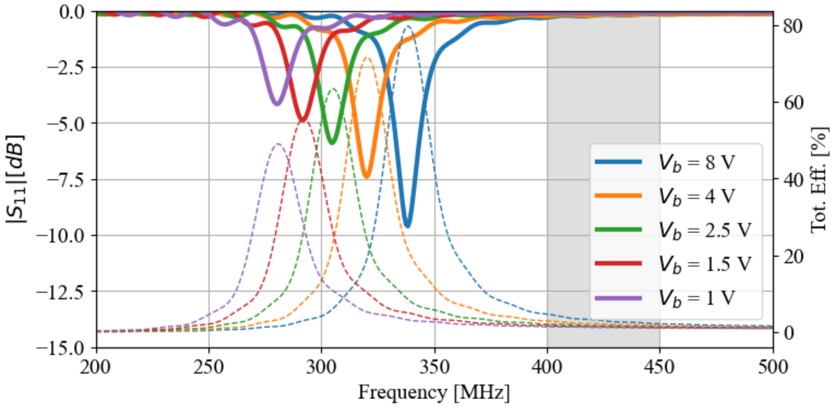

Figure 4.2.2: S_{11} parameter of the optimized structure for 400 MHz when loading the ends with a capacitor within the chosen Varicap range. The frequency shift from 400 MHz and the reduction from 93% of total efficiency are clear.

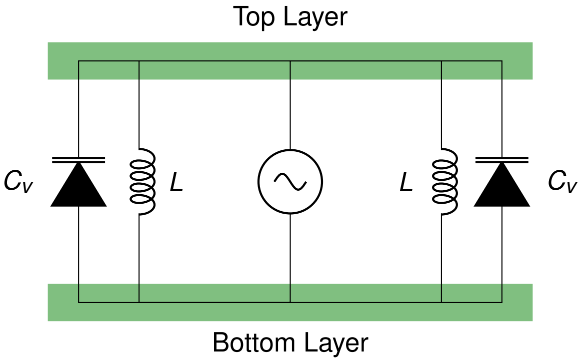

Figure 4.2.3: Equivalent circuit of the antenna structure with the two arms of the loop connected each other through inductor and Varicap.

and Inductors. Again, miniaturization implies that a trade off must be found, necessitating a sacrifice in efficiency.

By centering the load balance to 420 MHz, thus maximizing the antenna total efficiency when using the middle bias voltage 2.5 V of the Varicap (corresponding to about 0.83 pF), we find an equivalent parallel inductance of 175 nH. Results of the optimized reactive loaded circular AL are shown in Figure 4.2.4.

The span, 400 MHz to 440 MHz, is entirely covered by the Varicap sweep. Moreover there are values of the Varicap that make the antenna resonate outside the required bands. Although the S-parameter is always lower than -17 dB and total efficiency always greater than 90% in the design frequency band. Finally, DC bias voltage values range between 2.5 V and 8 V to continuously adjust the resonance frequency in the required frequency band. Centering the reconfiguration frequency range also provides a margin of error for eventual compensations of manifacture inaccuracies.

In terms of radiation, the antenna structure develops the omnidirectional pattern of a magnetic source, as expected from a loop. Figure 4.2.5 shows the θ and ϕ realized gain components for the two required bands: 400 MHz when loaded with a 0.9 pF equivalent capacitor, and 440 MHz when loaded with a 0.55 pF. The horizontal polarization is confirmed by the over 40 dB difference between θ and ϕ components, showing the dominance of the horizontal E_ϕ in both cases.

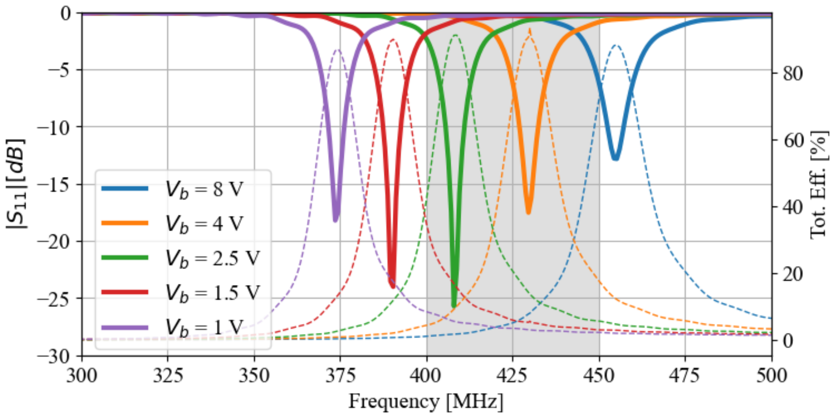

Figure 4.2.4: S_{11} parameter of the optimized structure at 420 MHz for a fixed inductance $L = 175nH$ within the Varicap values range. Frequency is now re-centered on the design band but the spread for frequency reconfiguration is wider.

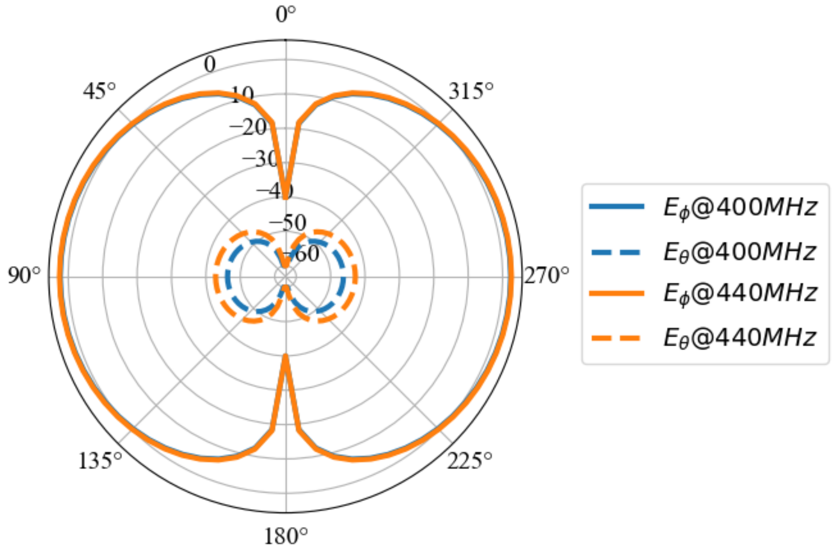

Figure 4.2.5: Realized Gain radiation pattern ϕ and θ components in the $\phi = 0$ cut.

4.3 Switched Frequency Omnidirectional Antenna

An alternative of the circular AL for switched frequency reconfiguration is discussed in this section. The proposed antenna is based on the study discussed in Section 4.2.1. The structure is differentially fed from the center, and the circular AL parts are printed on both sides of a 1.6 mm thick PTFE PCB with a 174 mm diameter.

While in the previous example of continuously frequency agile AL, the load was considered as a lumped element in simulations, applying the parallel Varicap and inductance virtually between two points, in this section a focus is made on practical implementation of the switchable circuit, based on PIN-diodes, designed to best represent real implementation.

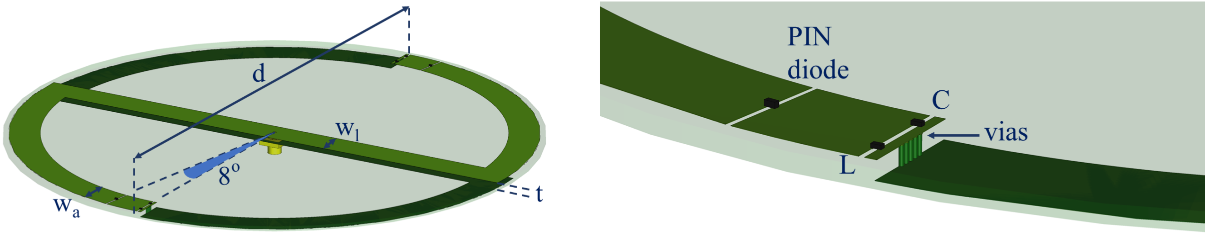

(a) (b)

Figure 4.3.1: Alford loop antenna structure

4.3.1 Base antenna structure

As in the previous section, the design process starts from the design of the circular AL to operate at 400 MHz. Then a slot is carved on the upper-layer arms to reach a 440 MHz resonance, and finally the integration of the PIN-diode is performed. An additional optimization based on the presence of a parallel LC circuit is also included to tune the switched frequencies and allow the DC bias over the differential feed.

In Figure 4.3.1, the circular AL structure designed for switchable frequency reconfiguration is shown, and in Figure 4.3.1 (b) a zoom in the loading area is depicted with the presence of a PIN-diode, an LC parallel, and vias between the two PCB layers.

The presence of the slot which hosts the PIN-diode moves the resonant frequency to higher values, as it reduces the electrical length of the AL arms. When the diode is forwardly biased, the slot gap is shorted, and the antenna operates as the base structure.

The position of the slot is crucial to ensure the right frequency spacing between the two resonances. In Figure 4.3.2, steps of 5° to the center of the loop have been considered, and two remarks can be made compared to the curve without slots. The introduction of the slot shifts the resonant frequency to a 450 MHz, a 50 MHz hop, while the frequency shift due to each successive 5° increasing angle is around 12 MHz. Furthermore, a mismatch due to a reduction of the resistive part of the input impedance reduces the magnitude of the reflection coefficient.

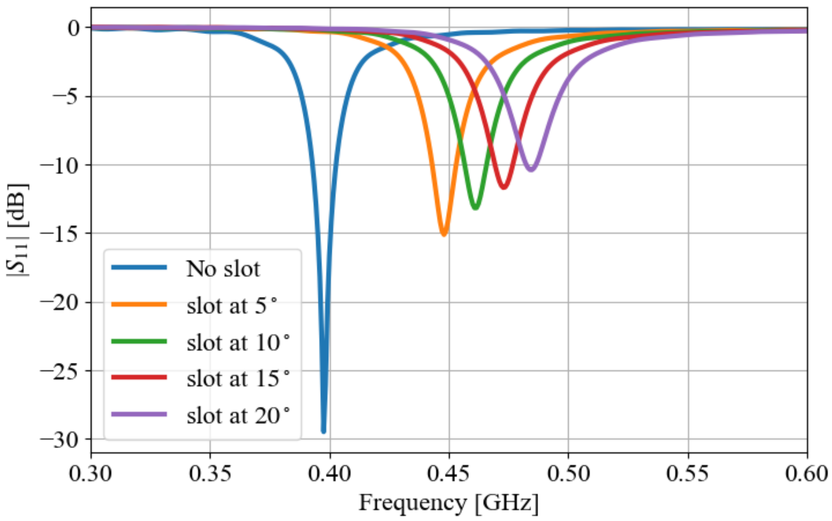

Figure 4.3.2: Resonant frequency responce to slot on the upper arm. Comparison with different angles.

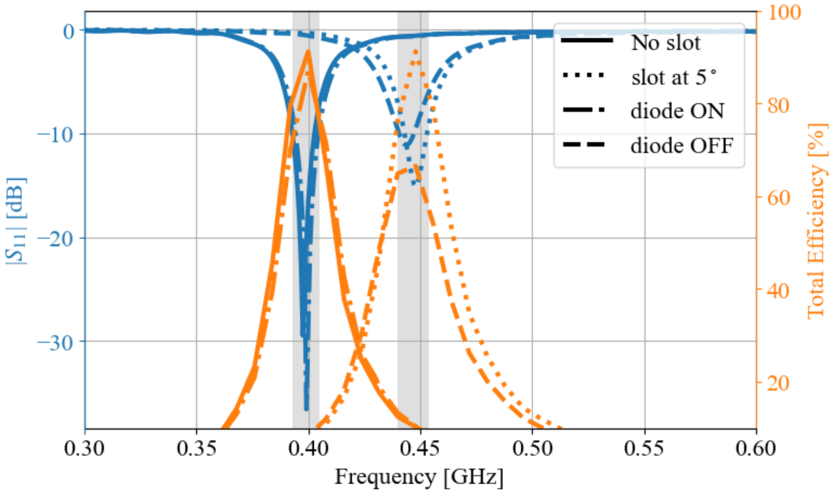

Figure 4.3.3: Effects of PIN diode introduction on the slot.

4.3.2 Reconfiguration Mechanism Design and Integration

The placement of a Skyworks® SMP1345 Very low capacitance silicon PIN diode have been considered in simulation using the measured S-parameter provided by the manufacturer as a Touchstone file. Results comparing the active diode with the original AL structure and the diode turned off with the slotted AL at 5° are presented in Figure 4.3.3. The only difference lies in the effect of the diode turned off. The equivalent circuit of the diode when inversely biased is a very low capacitance of 0.15 pF. The reduction of total efficiency depends mostly by the mismatch induced with the capacitive load of the diode, thus radiating efficiency decreases.

The far-field pattern in terms of ϕ and θ components of the simulated realized gain is displayed in Figure 4.3.4 where the typical magnetic dipole's E_ϕ-dominant radiation is clear, also proving the horizontal polarization of the AL structure with more than 40 dB difference between E_θ and E_ϕ. In both cases, Diode ON at 400 MHz, and Diode OFF at 440 MHz the E_ϕ corresponds entirely.

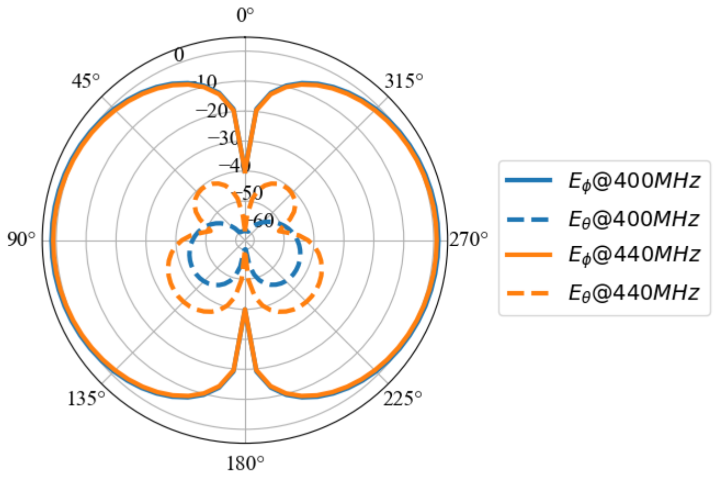

Figure 4.3.4: Realized Gain radiation pattern ϕ and θ components in the $\phi = 0$ for Diode ON and Diode OFF cases.

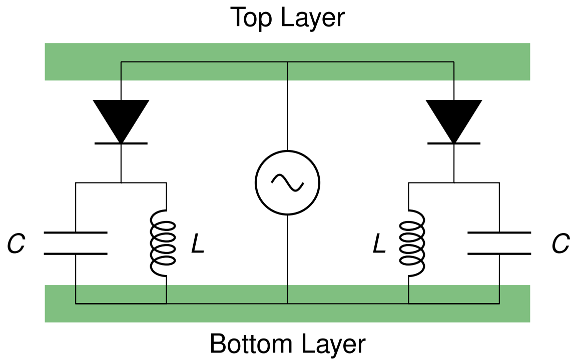

Figure 4.3.5: Equivalent circuit of the antenna structure with the two arms of the loop connected each other through the series PIN-diode and matching LC circuit.

The reconfiguration mechanism represents an additional design constraint in the case it has to be controlled from the RF feeding port. To achieve this, the two layers of the AL must provide DC continuity. Vias have been considered to join the end of upper layer AL arms with their corresponding ones on the lower layer [Figure 4.3.1]. As small vias act as inductances, the structure behaves as if it was loaded with a positive reactive load, resulting in a resonant frequency shift to higher frequencies.

A matching LC parallel circuit is designed to overcome this mismatch as shown in Figure 4.3.5, considering that proper choice of loads leads to a well-matched RF circuit with DC continuity between layers. The TDK 100 nH super High-Q inductance have been chosen for its stability at the design frequency. Consequently, the capacitive load have been chosen regarding the relation $C = {}^{1}\!/_{\omega^2 L} = 1.58$ pF.

After tuning the capacitor value, slightly reduced to increase the resonance frequency to approach the required bands, the frequency reconfiguration range still differs from the expected theoretical simulations of the previous section. A further optimization on the slot angle position have been performed, considering the realistic values of the loads to be included in the prototype at the design frequency of 400 MHz: a 1.2 pF capacitor discrete component, and a 100 nH inductance discrete component. The angle position of the slot in the final version is 8°.

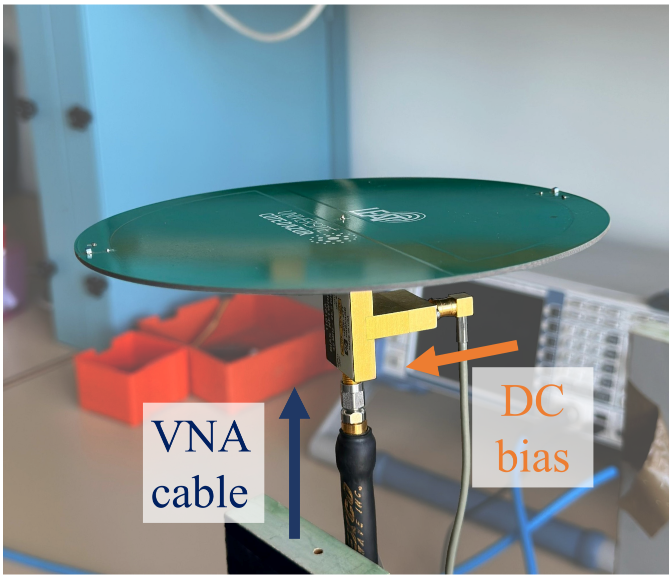

Figure 4.3.6: Photo during reflecting coefficient measurements with VNA showing the setup including the HP 11612A Bias Network which takes DC bias between the VNA cable and the Device Under Test (DUT).

4.3.3 Measured results and discussion

A prototype of the proposed antenna have been manufactured and characterized. The antenna prototype have been characterized using a Keysight VNA, interposing an HP 11612A Bias Network between the VNA cable and the antenna's SMA connector to allow the DC bias over SMA input, as depicted in Figure 4.3.6. The frequency reconfiguration was made possible by connecting the DC input of the bias network to a 2.1 V feeding power supply, to comply with the SMP1345 Touchstone file considered in simulations.

The measured $|S_{11}|$, presented in Figure 4.3.7, shows that the prototype successfully reconfigure its resonance frequency in the desired frequency bands. However, lower levels of the reflection coefficient are detected, with the version with activated diode at 400 MHz not reaching the -5 dB.

Discrete components, especially inductances, even high-Q ones, may behave differently from their typical value at high frequencies. There is usually a direct proportionality between inductance value and frequency. For this reason, the subsequent lower inductance value of 91 nH, available as a discrete component, have been used instead of the 100 nH to validate this point, and it is also plotted in Figure 4.3.7 in green. The resonances become clearer, with lower values of $|S_{11}|$ in the desired bands, although the diode-activated model does not reach the -10 dB.

Measurements of far-field directivity, gain, and thus efficiency, are not reported due to the challenges related to measurement for very wide wavelength. The simplicity of the loop antenna structure, as a magnetic dipole, makes it plausible that if the response of the system in terms of resonance is similar to the expected simulated one, it should radiate omnidirectionally as a magnetic dipole. However,no further considerations regarding losses and efficiency can be made.

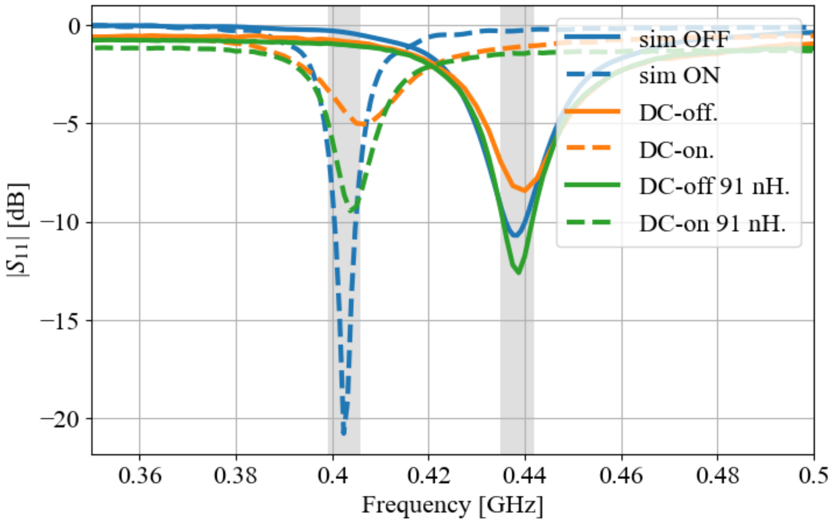

Figure 4.3.7: Reflection coefficient comparison between three models versions: Simulations (blue), Measurements (orange), and Measurements with modified L load (green). All versions for both states of the switched diode: OFF (plain), and ON (dashed).

4.4 Conclusion

This chapter has presented an overview of frequency reconfigurable antennas and frequency reconfigurability techniques available in literature.

A design based on the miniature circular AL have been carried out, comparing effects of substrate material on antenna size and efficiency. Two versions of the antenna frequency reconfiguration have been proposed: a frequency agility in Section 4.2 for continuous reconfiguration through the use of a Varicap, and a switched reconfiguration through the use of a PIN-diode. Simulated results show the attainment of the requirement through optimizations for double resonance in 400 MHz and 440 MHz.

Finally, a prototype was created to prove the concept, and consideration of the RF behavior of discrete SMT components is provided as a critical point to connect simulations and measurements.

In perspective, a far-field characterization in a controlled environment such as an anechoic chamber is expected. Moreover, the sensitivity to the specific discrete component behavior can be mitigated through a proper characterization of the device, or by incorporating these components in the RF design itself. This could involve printing them along with the antenna structure as RF capacitors and inductors.

Furthermore, the integration of a transceiver into the structure to transform it into an autonomous ground station for satellite IoT communications is envisioned, with test on real-life deployment.

Also, a detailed characterization of the reflection effects over the ground is expected. This may allow to fine tune the design to significantly enhance the efficiency of the antenna design for IoT applications.

References

[1] M.-C. Tang, Z. Wen, H. Wang, M. Li, and R. W. Ziolkowski, “Compact, frequency-reconfigurable filtenna with sharply defined wideband and continuously tunable narrowband states,” *IEEE Transactions on Antennas and Propagation*, vol. 65, no. 10, pp. 5026–5034, 2017.

[2] G. Polaiah, K. Kandasamy, and M. Kulkarni, “An autonomous frequency reconfigurable antenna using slotline open-loop resonators,” *IEEE Access*, vol. 9, pp. 82221–82232, 2021.

[3] V. Sathi, N. Ehteshami, and J. Nourinia, “Optically tuned frequency-reconfigurable microstrip antenna,” *IEEE Antennas and Wireless Propagation Letters*, vol. 11, pp. 1018–1020, 2012.

[4] L. Song, W. Gao, C. O. Chui, and Y. Rahmat-Samii, “Wideband frequency reconfigurable patch antenna with switchable slots based on liquid metal and 3-d printed microfluidics,” *IEEE Transactions on Antennas and Propagation*, vol. 67, no. 5, pp. 2886–2895, 2019.

[5] L. Li, X. Yan, H. C. Zhang, and Q. Wang, “Polarization- and frequency-reconfigurable patch antenna using gravity-controlled liquid metal,” *IEEE Transactions on Circuits and Systems II: Express Briefs*, vol. 69, no. 3, pp. 1029–1033, 2022.

[6] Z. Chen, H.-Z. Li, H. Wong, W. He, J. Ren, and T. Yuan, “A frequency-reconfigurable dielectric resonator antenna with a water layer,” *IEEE Antennas and Wireless Propagation Letters*, vol. 22, no. 6, pp. 1456–1460, 2023.

[7] S. Lee, S. I. H. Shah, H. L. Lee, and S. Lim, “Frequency-reconfigurable antenna inspired by origami flasher,” *IEEE Antennas and Wireless Propagation Letters*, vol. 18, no. 8, pp. 1691–1695, 2019.

[8] M.-C. Tang, R. W. Ziolkowski, S. Xiao, M. Li, and J. Zhang, “Frequency-agile, efficient, near-field resonant parasitic monopole antenna,” *IEEE Transactions on Antennas and Propagation*, vol. 62, no. 3, pp. 1479–1483, 2014.

[9] X. Zhao and S. Riaz, “A dual-band frequency reconfigurable mimo patch-slot antenna based on reconfigurable microstrip feedline,” *IEEE Access*, vol. 6, pp. 41450–41457, 2018.

[10] A. Vamseekrishna, B. T. P. Madhav, T. Anilkumar, and L. S. S. Reddy, “An iot controlled octahedron frequency reconfigurable multiband antenna for microwave sensing applications,” *IEEE Sensors Letters*, vol. 3, no. 10, pp. 1–4, 2019.

[11] J. Hu and Z.-C. Hao, “Design of a frequency and polarization reconfigurable patch antenna with a stable gain,” *IEEE Access*, vol. 6, pp. 68169–68175, 2018.

[12] M. W. Young, S. Yong, and J. T. Bernhard, “A miniaturized frequency reconfigurable antenna with single bias, dual varactor tuning,” *IEEE Transactions on Antennas and Propagation*, vol. 63, no. 3, pp. 946–951, 2015.

[13] P.-L. Chi, R. Waterhouse, and T. Itoh, “Compact and tunable slot-loop antenna,” *IEEE Transactions on Antennas and Propagation*, vol. 59, no. 4, pp. 1394–1397, 2011.

[14] R. Jawale, J. Padhi, and G. S. Reddy, “Frequency reconfigurable rectangular loop antenna,” in *2021 IEEE Indian Conference on Antennas and Propagation (InCAP)*, pp. 96–98, 2021.

[15] H.-J. Huang, C.-H. Tsai, C.-P. Lai, and S.-Y. Chen, “Frequency-tunable miniaturized strip loop antenna fed by a coplanar strip,” *IEEE Antennas and Wireless Propagation Letters*, vol. 15, pp. 1000–1003, 2016.

[16] Microsemi, “Kv1900 gc1300 series datasheet.” https://www.microsemi.com/document-portal/doc_download/8786-kv1900-gc1300-series-datasheet.

5 Conclusions and Perspectives

This thesis delved into the design principles and implementation strategies of modern IoT antennas. The unifying theme across all studies was the focus on miniaturization for highly portable and versatile IoT applications, as well as the investigation of practical manifacturing and measuring conditions. Designing antennas for IoT, particularly reconfigurable ones, poses uniques challenges. They necessitate complex structures where integrations of RF and DC circuit over the same structure is needed, which cannot be dealt with using traditional methods. Theoretical explanations of common structures seen in this text (such as WP in Section 2 and 3, or loop in Section 2 and 4) form the groundwork of a work that, due to the added complexity of coexisting components, must primarly and inevitably rely mostly on simulations. This state-of-the-art design strategy, despite being increasingly adopted, still requires refinement before it can become a standard practice.

Intrinsic characteristics of antennas for IoT also pose a challenge on their characterization. For instance, miniature antennas that are differentially fed or have a small ground plane requires a balun for proper characterization (Section 2 and 3), even though in real-case deployment, the antenna is directly connected to the RF source. Alternatively, antennas for long-range IoT applications may operate at such low frequencies that common anechoic chamber would not suffice (Section 4).

- In Chapter 1 a comprehensive review of current standards and technologies for next generation cellular network and IoT is conducted. The potentials and constraints of different standard in the IoT domain are analyzed in detail, with a focus on the trade-offs between power consumption, range, and data rate. This study lays the groundworkfor understanding the key challenges and specific design requirements and limitations of antennas for IoT.

  The effects of miniaturization and ESA on portability are discussed, noting the limitations they impose on radiated efficiency and bandwidth, which are crucial for low-power long range applications. The implementation of CP antennas for more robust communications is also explored. Lastly, the potential of reconfigurable antennas, the core of this thesis, is discussed. These antennas can dynamically adapt to application-specific functions or surrounding environment, albeit at a higher design complexity cost.

- Chapter 2 delves into the design and development of compact, OCP antennas for use in IoT applications. The chapter begins by outlining the benefits of employing OCP antennas in modern wireless systems, including their capacity to mitigate signal orientation issues and multipath fading. It then addresses the challenges associated with designing compact OCP antennas, reviewing existing solutions and their respective limitations. The main body of the chapter examines two OCP antenna designs: a miniature antenna and its reconfigurable version. The design process is detailed through numerical simulations and experimental results, and comparisons with other OCP antennas documented in literature are proposed as well.

  - A compact single-fed OCP antenna design and implementation is presented in Section 2.2. CP is obtained by combining an AL and a WP radiating structures, which are used to generate two orthogonal E-field components. The antenna exhibits a clear RHCP with a dipole-like omnidirectional radiation pattern. A prototype has been realized using two FR-4 PCBs and experimentally tested. The measured -10 dB impedance matching bandwidth is 120 MHz wide (4.9%) from 2.40 to 2.52 GHz. The measured RCHP maximum realized gain and total efficiency are 1.91 dBic and 87%, respectively. Its compact size ($0.25\lambda \times 0.25\lambda \times 0.08\lambda$), and its low-cost, robust, and easy-to-realize structure make this antenna an ideal candidate for IoT applications.
  - Based on this structure, a RHCP to LHCP reconfigurable OCP antenna has been studied in Section 2.3. The reconfiguration, based on 8 PIN-diodes, relatively low-power demanding, enhances the previous design with polarization diversity. Measurements on a prototype of this antenna highlights the importance of addressing challenges related to the integration of discrete SMT components during the antenna design and optimization process, and emphasizes the critical role of the forward DC biasing current in the PIN-diodes for their AC applications.

  The work presented in this chapter underscores the necessity of incorporating simpler DC biasing network in antenna designs, which takes into account the complexity of implementation and the RF behavior of discrete SMT components. Future direction may include the use of alternative devices to PIN-diodes, with low insertion-loss, like RF-MEMS on the proposed antenna.

- Chapter 3 centers on the design and implementation of pattern reconfigurable antennas, which can dynamically adjust the direction or shape of their transmitted and received signals. This capability is particularly beneficial for IoT applications, where devices may be in motion or need to communicate over long distances. The chapter emphasizes the importance of optimisation techniques to achieve optimal antenna performance and overcome the challenges involved in incorporating complex switching mechanisms into the antenna design. ESPAR antenna designs are also provided for drone-based long-range LoRa communications. Additionally, the chapter explores the reconfigurability of flexible, conformal arrays for wearable and deployable systems.

  - The design of an ESPAR of co-planar omnidirectional sources is discussed in Section 3.2. The design process included use of a PSO algorithm to maximize the realized gain in the desired direction for two similar structures, scaled to work at 5.075 GHz and 2.4 GHz. All considerations are validated by measurements on a prototype of the 5.075 GHz version, which aligns with simulated results. The section demonstrates that a crucial aspect of designing complex reconfigurable structures lies in including the reconfiguratin control system in the design optimization. Although this step is more demanding in terms of computation, it allows for a more accurate description of the antenna system behavior and may reduce the design conception steps.
  - a five elements ESPAR is proposed in Section 3.3 to meet the requirements for low-profile, long-range, easy-to-assemble antennas for UAVs in long-range 868 MHz LoRa communications.

    The proposed design, based on PIN diodes, is validated by a prototype which has been characterized both in a controlled environment and in a real-world scenario, on board of an hexacopter drone. On-field communication tests were performed to evaluate the advantages of the directive beam for coverage improvement. Measures of RSSI on LoRaPHI packet communications proved that directive beams can improve the channel reliability, potentially allowing for longer distance coverage. The section provides the description of a versatile infrastructure tool for the analysis and real-time measurement of antennas for long-range IoT applications.

  - In Section 3.4, a four element array of five-series-fed patch elements is presented for arbitrarily conformal phased arrays for wearable, deployable, and morphing RF applications. An assessment of multiple bending and folding shapes, concave, convex and accordion-like, is presented and compared to a planar conventional phased-array. The strategic tuning of amplitude and phase feeding of the phased-array, as well as selective activation, can greatly improve performance of conformal shape-changed phased-arrys in terms of beamwidth and SLL mitigation. Along with phased-array beam-steering, the additional pattern reconfigurability given by shape-change opens to diverse opportunities for advancements in communications and sensing applications.

  The production of an optimized complete seven element ESPAR structure prototype and its characterization is expected to further validate the foundation laid by this work. A future direction may be to benchmark the electronically switched beam capabilities in terms of switching time, radiation performance, and control speed to compare the switchable ESPAR technology to other technologies like radars or phased arrays. The PSO can be further improved to optimize other aspects such as specific polarization or radiation frequency, or else, minimize losses due to mismatch in complex arrays impedance networks. An extension to other type of pattern reconfigurable antennas, working at different bands, is enabled with the drone-based open-air measuring infrastructure. Future directions may consider the use of more diverse antennas and protocols in this framework, with a focus also on higher level advantages of pattern reconfigurable antennas on wireless communications. The potential of combining multiple pattern reconfiguration techniques is significant, but design and tuning complexity increase in parallel. Advanced optimization techniques for tuning amplitude and phase of the foldable phased-array is needed. Neural networks and AI can be applied to this end for real-time phased array feeding tuning.

- Chapter 4 focuses on the design and development of miniature frequency-reconfigurable antennas for ground-station IoT satellite communication applications. A circular AL has been made frequency agile using a Varicap (Section 4.2) for continuous tuning and a PIN-diode (Sec 4.3) for discrete switched-frequency. In both cases, the required bands of 400 MHz and 440 MHz are covered, and the antenna radiaties in horizontal polarization. The chapter delves into the design process, including considerations for miniaturization, efficiency, and practical implementations with RF behavior of discrete SMT components.

  Looking ahead, it is anticipated that a far-field characterization will be conducted in an anechoic chamber. Additionally, the impact of specific discrete component behavior can be mitigated through comprehensive device characterization or by integrating these components directly into the RF design as micro-strip. This could involve fabricating them concurrently with the antenna structure as RF capacitors and inductors. Furthermore, the incorporation of a transceiver within the structure is contemplated, with the aim of transforming it into a self-sufficient ground station for satellite IoT communications. This would involve testing in real-world deployment scenarios. In this framework, a thorough analysis of the reflection effects on the ground could potentially enable the fine-tuning of the design to significantly augment the efficiency of the antenna design for IoT applications.

List of Figures

List of Tables

List of Acronyms

3GPP	Third Generation Partnership Project	3
AC	Alternating Current	8
AI	Artificial Intelligence	1
AL	Alford Loop	14
AR	Axial Ratio	14
balun	Balance-to-Unbalance	32
BFIC	Beam Former Integrated Circuit	60
BLE	Bluetooth Low Energy	4
BPSK	Binary Phase Shift Keying	41
CLL	Capacitively Loaded Loop	40
CNC	Computer Numerical Control	25
CP	Circular Polarization	7
CSMA	Carrier Sense Multiple Access	2
CSMA/CA	Carrier Sense Multiple Access with Collision Avoidance	5
CSS	Chirp Spread Spectrum	5
D2G	Drone to Ground	41
DC	Direct Current	8
DGS	Defected Ground Structure	72
DoA	Direction of Arrival	41
DRA	Dielectric Resonator Antenna	14
DSSS	Direct Sequence Spread Spectrum	5
DUT	Device Under Test	82
EC-GSM	Extended Coverage - Global System for Mobile communication	4
eMBB	enhanced Mobile Broadband	1
eMTC	enhanced Machine Type Communication	4
ESA	Electrically Small Antennas	6
ESPAR	Electronically Steerable Parasitic Array Radiator	VII
ETSI	European Telecommunications Standard Institute	3
FB	Fractional Bandwidth	75
FBR	Front-to-Back Ratio	45
FDMA	Frequency Division Multiple Access	4
GA	Genetic Algorithm	40
GSM	Global System for Mobile communication	4

GWO	Gray Wolf Optimizer	41
HPBW	Half-Power Beam Width	45
IC	Integrated Circuit	60
IEEE	Institute of Electrical and Electronics Engineers	3
IETF	Internet Engineering Task Force	3
IIoT	Industrial Internet of Things	2
IoIT	Internet of Intelligent Things	6
IoT	Internet of Things	VII
IP	Internet Protocol	5
ISM	Industrial, Scientific and Medical	2
LAN	Local Area Network	40
LECIM	Low Energy Critical Infrastructure Monitoring Networks	5
LHCP	Left Handed Circular Polarization	13
LoS	Line-of-Sight	55
LP	Linear Polarization	15
LPWAN	Low Power Wide Area Network	3
LR-WPAN	Low Rate - Wireless Personal Area Network	5
LTE	Long Term Evolution	4
LTE-M	Long Term Evolution for Machine-Type communications	4
M2M	Machine to Machine	6
MAC	Medium Access Control	5
MIMO	Multi Input Multi Output	72
ML	Machine Learning	6
mMTC	massive Machine Type Communications	1
MNO	Mobile Network Operator	4
MTC	Machine Type Communications	2
NB-IoT	Narrow-Band Internet of Things	4
NFRP	Near Field Resonant Parasitic	40
OC	Open Circuit	30
OCP	Omnidirectional Circular Polarization	VII
OFDMA	Orthogonal Frequency Division Multiple Access	4
PCA	Priority Channel Access	5
PCB	Printed Circuit Board	7
PIN	Positive Intrinsic Negative	8
PIFA	Planar Inverted F Antenna	14
PRACH	Phisical Random Access Channel	4
PRB	Physical Resource Block	4
PSO	Particle Swarm Optimization	9
QoS	Quality of Service	2
R-FDMA	Random Frequency Division Multiple Access	5
RF	Radio Frequency	6
RF-MEMS	Radio Frequency - Microelectromechanical Systems	8
RFID	Radio Frequency IDentification	1

RHCP	Right Handed Circular Polarization	13
RSSI	Received Signal Strength Indicator	41
RX	Reception	60
SC	Short Circuit	31
SDO	Standards Development Organisations	3
SI	Swarm Intelligence	40
SIG	Special Interest Group	3
SLL	Side Lobe Level	46
SMA	SubMiniature version A	18
SMT	Surface Mounted Technology	35
SNR	Signal to Noise Ratio	3
SP4T	Single Pole Four Through	43
SPDT	Single Pole Double Through	41
SPI	Serial Peripheral Interface	65
SPnT	Single Pole Multiple Through	40
TX	Transmission	60
UAV	Unmanned Aerial Vehicle	39
UE	User Equipment	4
UHF	Ultra High Frequency	73
UNB	Ultra Narrow Band	4
URLLC	Ultra-Reliable and Low Latency Communications	1
UV	Ultra Violet	65
Varicap	Variable Capacity	8
VNA	Vector Network Analyzer	25
VSWR	Voltage Standing Wave Ratio	54
WAN	Wide Area Network	2
WLAN	Wireless Local Area Network	3
WOA	Whale Optimization Algorithm	41
WP	Wire-Patch	18
WPAN	Wireless Personal Area Network	2
WRAN	Wireless Regional Area Network	3
WSN	Wireless Sensors Networks	5
ZOR	Zeroth-Order Resonance	15

A PSO for optimal ESPAR loads

Problem formulation

Let us consider the ESPAR as an array network. Its electric far-field can be described as the weighted combination of each element's far-field:

$$\boldsymbol{E_{TOT}} = \sum_{i=1}^{N} \boldsymbol{E_i} \cdot \boldsymbol{a_i} \tag{A.0.1}$$

where N is the number of radiators and a_i the weight coefficients.

These are the variables that the PSO will use to perform. These coefficients are processed as the unique solution of the linear system:

$$\boldsymbol{A} * \boldsymbol{a} = \boldsymbol{b} \tag{A.0.2}$$

where, A (A.0.3) is the $N \times N$ diagonal matrix of the S-parameters, normalized on the reflection coefficient of the i^{th} particle Γ_i (A.0.4):

$$\boldsymbol{A} = S_{i,j} \cdot \Gamma_i - \boldsymbol{I_N} \tag{A.0.3}$$

$$\Gamma_i = \frac{Z_i - 50}{Z_i + 50} \tag{A.0.4}$$

where i, j are the index of the N radiators and I_N the identity matrix of size N. And $b = \{-1, 0, 0, ...0\}$ considering the first radiator the only driven one.

Summarizing, knowing only the impedance network S-parameters $S_{i,j}$ and electric far-fields of each radiating element E_i, is possible to compute the ESPAR far-field, thus directivity or gain, eventually considering radiation efficiency e_r.

Particle Swarm Optimizer formulation

The PSO algorithm is based on the original work from Kennedy et al.[1] and expressed here for the specific problem.

---

[1] J. Kennedy and R. Eberhart, "Particle swarm optimization," Proceedings of ICNN'95 - International Conference on Neural Networks, Perth, WA, Australia, 1995, pp. 1942-1948 vol.4, doi: 10.1109/ICNN.1995.488968.

The optimizer uses multiple simultaneous potential solutions: the particles, randomly generated at each round. Convergence is achieved after an amount R of rounds, where particles are updated based on parameters like velocity v and direction d, which in turn depend on the particle which gave the best cost function result.

Concerning the problem previously stated, noted that $\boldsymbol{S_{ij}}$ and $\boldsymbol{E_i}$ can be available from a single full-wave simulation over a specific ESPAR geometry, the optimizing algorithm will start from Z_p^0, set of ESPAR radiating elements' impedances for the particle p at the iteration 0. Then calculate with (A.0.1) at each recursive round for each particle $E_{TOT_p}^k$. At the end of each round k the best particle is selected that generates the maximum far-field.